Suez University
Faculty of Petroleum and Mining Eng.
Engineering Sciences Department

A Numerical and Experimental Study of Tubular Solar Still

A Thesis
Submitted in Partial Fulfillment of
M.Sc. in
Energy Engineering

By
Eng. Abdelhady Maher Zaghloul
B.Sc. Mechanical Engineering
(2006)

Supervision Committee

Dr. Sayed Al-Huleiby
Ass. Prof. of Mech. Eng –Eng. Sciences Dept.
Faculty of Pet.&Min. Eng.
Suez university

Dr. Ahmed Mohamed Soliman
Lecturer of Mech. Eng -Eng Sciences Dept
Faculty of Pet.&Min. Eng.
Suez University

Dr. Mohamed Abdel-WahabSharaf El-Din
Lecturer of Mechanical Eng. –Eng. Sciences Dept.
Faculty of Pet.&Min. Eng.
Suez University

SUEZ
2015

Suez University
Faculty of Petroleum and Mining Eng.
Engineering Sciences Department

Approval

A Numerical and Experimental Study of Tubular Solar Still

A Thesis
Submitted in Partial Fulfillment of
M.Sc. in
Energy Engineering

By

Eng. Abdelhady Maher Zaghloul
B.Sc. Mechanical Engineering
(2006)

Approval Committee

Prof. El-Desouki EbrahimEid
Prof. of Mechanical Power Eng.
Dean of Faculty of Industrial Education Eng.
Suez University

Dr. Ahmed Safwat Mohamed
Ass. Prof of Mech. Eng.–Eng. Sciences Dept.
Faculty of Pet.&Min. Eng.
Suez University

Dr. Sayed Al-Huleiby
Assoc. Prof. of Mechanical Engineering
Faculty of Pet.&Min. Eng.
Suez university

Approval

Data 27/6/2015

Dean of Faculty.

SUEZ
2015

`

Author	**Abdelhady Maher Zaghloul**
Title	**A Numerical and Experimental Study of Tubular Solar Still**
Faculty	**Faculty of Petroleum and Mining Engineering**
Department	**Energy Engineering Department**
Location	**Suez-Egypt**
Degree	**Master Degree in Materials Science and Engineering**
Date	**27/6/2015**
Language	**English**
Supervisors	**1- Prof. Sayed Al-Huleiby** **2- Dr. Ahmed Mohamed Soliman** **3- Dr. Mohamed Abdel-Wahab Sharaf El-Din**

Abstract

Desalination has been increasingly adopted over the last decades as an option, and sometimes as a necessity to overcome water shortages in many areas around the world Direct sunlight has been utilized long back for desalination of water. Solar distillation plants are used for supplying desalinated water to small communities nearby coastal remote areas. Solar stills are easy to construct, can be done by local people from locally available materials, simple in operation by unskilled personnel, no hard maintenance requirements and almost no operation cost. Hence for increasing the performance of solar still it is necessary to model and investigate the effect of different parameters as condensing cover. Present work aimed at modeling of tubular solar still using ANSYS CFX 15.0 to investigate the effect of different radii on the yield. A 3-D two phase model is developed for evaporation and condensation process to simulate the temperature distribution of water and gas phase and also the amount of fresh water productivity. Three different radii studied to analyze the effect on rate of evaporation. Simulation is carried out from 40-60 °C with 5 °C interval. For 100, 150 and 200 mm radii. The test took place in Suez Governorate (latitude of 29° 966' and longitude of 32° 549')

Preface

This thesis is submitted for the Master degree in science at Suez Canal University – Faculty of Petroleum and Mining Engineering. The work reported herein was carried out under the supervision of Prof Ass. Sayed Al-Huleiby, Dr. Ahmed Mohamed Soliman and Dr. Mohamed Abdel-Wahab Sharaf El-Din, Engineering Science department, Faculty of Petroleum & Mining Engineering in the period of July 2012 to May 2015. To the best of my knowledge, this work is original, except where suitable references are made to previous work. Neither this, nor any substantially similar thesis has been submitted for any degree, diploma or qualification at any other university or institution in Egypt. This thesis does not exceed 20,000 words in length.

Abdelhady M. Zaghloul

May 2015

Acknowledgments

First, I thank ALLAH the most Beneficent, the most Merciful for helping me to complete this work. I would like to express my sincere thanks and gratitude to my supervisors Prof Ass. Sayed Al-Huleiby, Dr. Ahmed Mohamed Soliman and Dr. Mohamed Abdel-Wahab Sharaf El-Din, Engineering Science department, Faculty of Petroleum & Mining Engineering, for their support, guidance and enthusiasm. I also want to acknowledge, all the staff members of the Engineering Science department, Faculty of Petroleum & Mining Engineering, (especially Prof. Ahmed Safwat – Head of department, Dr. Ahmed Soliman) for their support, guidance and enthusiasm. Also my deep sincerity to Dr. Adel Tawfik and Dr. Hany Al-Gohary for their efforts during the pre-semester. Finally I wish to record my deep sense of appreciation for my parents, brother and sister for relentlessly supporting me during entire the period.

Abstract

Desalination has been increasingly adopted over the last decades as an option, and sometimes as a necessity to overcome water shortages in many areas around the world Direct sunlight has been utilized long back for desalination of water. Solar distillation plants are used for supplying desalinated water to small communities nearby coastal remote areas. Solar stills are easy to construct, can be done by local people from locally available materials, simple in operation by unskilled personnel, no hard maintenance requirements and almost no operation cost. Hence for increasing the performance of solar still it is necessary to model and investigate the effect of different parameters as condensing cover. Present work aimed at modeling of tubular solar still using ANSYS CFX 15.0 to investigate the effect of different radii on the yield. A 3-D two phase model is developed for evaporation and condensation process to simulate the temperature distribution of water and gas phase and also the amount of fresh water productivity. Three different radii studied to analyze the effect on rate of evaporation. Simulation is carried out from 40-60 °C with 5 °C interval. For 100, 150 and 200 mm radii. The test took place in Suez Governorate (latitude of 29° 966' and longitude of 32° 549')

Contents

ACKNOWLEDGEMENTS **I**
ABSTRACT **Iii**
LIST OF SYMBOLS **V**
CONTENTS **Ix**
LIST OF FIGURES **Xiii**
LIST OF TABLES **Xvi**

CHAPTER 1 INTRODUCTION **1**

1.1 WATER SHORTAGE 1
1.2 SOLAR DESALINATION SYSTEMS AS A CHOICE 3
1.3 DESALINATION TECHNIQUES 5
1.3.1 Membrane Desalination (RO) 6
1.3.2 Evaporation Processes 8
1.4 EVAPORATION BEHAVIOUR 9
1.4.1 Evaporation Theory 9
1.5 CONDENSATION BEHAVIOUR 11
1.6 HISTORICAL BACKGROUND 11
1.7 WHAT IS SOLAR STILL 13
1.8 TYPES OF SOLAR STILL 14
1.8.1 Active and passive solar still 15
1.8.2 Solar still design 15
1.8.2.1 Single basin type solar still 16
1.8.2.2 Solar still concave surface 16

1.8.2.3 Double-basin solar still 17
1.8.2.4 Hemispherical solar still 18
1.9 SOLAR COLLECTORS 18
1.10 CFD MODELING 19
1.11 OBJECTIVE 21

CHAPTER 2 LITERATURE REVIEW 24

2.1 HISTORICAL BACKGROUND OF DESALINATION 24
2.2 PARAMETRIC STUDY 37
2.2.1 Climatic Parameters 38
2.2.2 Design Parameters 38
2.2.3 Operational Parameters 39

CHAPTER 3 METHODOLOGY 41

3.1 INTRODUCTION 41
3.2 CFD-PROCESS 42
3.2.1 Pre-processing 42
3.2.2 Solving 42
3.2.3 Post-processing 43
3.3 NUMERICAL SIMULATIONS 43
3.3.1 Theory 43

3.3.2	Conduction	44
3.3.3	Convection	45
3.3.4	Radiation	47
3.3.5	Condensation	49
3.4	GOVERNING EQUATIONS	50
3.4.1	Energy equation	50
3.4.2	Continuity equation	50
3.4.3	Momentum equation	51
3.5	PHYSICAL MODEL	53
3.5.1	Experimental Set Up	53
3.5.2	Measurement Instruments	57
3.5.2.1	Temperature sensors specifications (Thermocouples)	57
3.5.2.2	Temperature Recorder (measures ambient temperature)	58
3.5.2.3	Solar Intensity Recorder	59
3.5.2.4	Anemometer (measures wind speed)	60
3.5.3	Weather Conditions and Measurements	61
3.5.4	Methodology	64
3.5.4.1	Geometry Details	64

3.5.4.2 Meshing Details 65

3.5.4.3 Pre-processing Details 68

3.5.4.4 Solving 68

3.5.4.5 CFX-Post 69

CHAPTER 4 RESULTS AND DISCUSSION 71

4 RESULTS AND DISCUSSIONS 71

4.1 Temperature Distribution 71

4.1.1 Simulation for 200 mm radius 72

4.1.2 Simulation for 150 mm radius 82

4.1.3 Simulation for 100 mm radius 92

4.2 EXPERIMENTAL VALIDATION 102

4.2.1 Water production rate by CFD and Experimental data 102

4.2.2 Water production rate by full-TSS and half-TSS models 108

4.2.2.1 Full-TSS models with constant tray dimensions 108

4.2.2.2 Half-TSS models with constant tray dimensions 110

4.2.2.3 Half-TSS models with variable tray dimensions 112

4.2.3 Water temperature by CFD and Experimental data 113

CHAPTER 5 CONCLUSION AND FUTURE SCOPE 117

5.1 FLOW OF WORK DONE 117

5.2 FUTURE SCOPE 120

REFERENCES **122**

List of Figures

Fig. 1.1	World solar radiation	4
Fig. 1.2	Flow chart of renewable energies powered desalination processes	`5
Fig. 1.3	Reverse Osmosis	8
Fig. 1.4	Conventional solar still	14
Fig. 1.5	Single-basin type solar still	15
Fig. 1.6	Concave wick solar	17
Fig. 1.7	Double-basin solar still	17
Fig. 1.8	Cross sectional view of a hemispherical solar still	18
Fig. 1.9	Solar Water Heater	19
Fig. 2.1	Della Porta solar distillation apparatus	25
Fig. 3.1	General CFD-Process	42
Fig. 3.2	Mass and heat transfer inside and outside of a TSS	44
Fig. 3.3	Suez location coordinates	54
Fig. 3.4	Experimental set-up of the full-TSS model with constant tray dimensions	55
Fig. 3.5	Experimental set-up of the half-TSS model with constant tray dimensions and thermocouples positions	55
Fig. 3.6	Experimental set-up of the half-TSS model with variable tray dimensions	56
Fig. 3.7	Constant and variable dimensions trays	56
Fig. 3.8	Thermocouple and Digital indicator	58
Fig. 3.9	Ambient temperature recorder	59

Fig. 3.10	HAENNI solar radiation	59
Fig. 3.11	Sensors of solar radiation	60
Fig. 3.12	Anemometer	60
Fig. 3.13	Comparison between the ambient temperature vs. the solar intensity	61
Fig. 3.14	Wind Speed	62
Fig. 3.15	Temperature variation for 100mm radius model	63
Fig. 3.16	Temperature variation for 150mm radius model	63
Fig. 3.17	Temperature variation for 200mm radius model	64
Fig. 3.18	3-D model of 100mm condensing cover radius	64
Fig. 3.19	3-D model of 150mm condensing cover radius	65
Fig. 3.20	3-D model of 200mm condensing cover radius	65
Fig. 3.21	3- D unstructured mesh of 100mm condensing cover radius	66
Fig. 3.22	3- D unstructured mesh of 150mm condensing cover radius	67
Fig. 3.23	3- D unstructured mesh of 200mm condensing cover radius	67
Fig. 3.24	Convergence graph of the fluid flow simulation	69
Fig. 4.1	Gas mixture temperature contour at a bottom temperature of 40°C for a 200mm radius	72
Fig. 4.2	Gas mixture temperature plot at a bottom temperature of 40°C for a 200mm radius	72
Fig. 4.3	Water temperature a contour at bottom temperature of 40°C for a 200mm radius	73
Fig. 4.4	Water temperature plot at a bottom temperature of 40°C for a 200mm radius	73
Fig. 4.5	Gas mixture temperature a contour at bottom temperature of 45°C for a 200mm radius	74

Fig. 4.6	Gas mixture temperature plot at a bottom temperature of 45°C for a 200mm radius	74
Fig. 4.7	Water temperature contour at a bottom temperature of 45°C for a 200mm radius	75
Fig. 4.8	Water temperature plot at a bottom temperature of 45°C for a 200mm radius	75
Fig. 4.9	Gas mixture temperature contour at a bottom temperature of 50°C for a 200mm radius	76
Fig. 4.10	Gas mixture temperature plot at a bottom temperature of 50°C for a 200mm radius	76
Fig. 4.11	Water temperature contour at a bottom temperature of 50°C for a 200mm radius	77
Fig. 4.12	Water temperature plot at a bottom temperature of 50°C for a 200mm radius	77
Fig. 4.13	Gas mixture temperature contour at a bottom temperature of 55°C for a 200mm radius	78
Fig. 4.14	Gas mixture temperature plot at a bottom temperature of 55°C for a 200mm radius	78
Fig. 4.15	Water temperature contour at a bottom temperature of 55°C for a 200mm radius	79
Fig. 4.16	Water temperature plot at a bottom temperature of 55°C for a 200mm radius	79
Fig. 4.17	Gas mixture temperature contour at a bottom temperature of 60°C for a 200mm radius	80
Fig. 4.18	Gas mixture temperature plot at a bottom temperature of 60°C for a 200mm radius	80
Fig. 4.19	Water temperature contour at a bottom temperature of 60°C for a 150mm radius	81
Fig. 4.20	Water temperature plot at a bottom temperature of 60°C for a 200mm radius	81
Fig. 4.21	Gas mixture temperature contour at a bottom temperature of 40°C for a 150mm radius	82
Fig. 4.22	Gas mixture temperature plot at a bottom temperature of 40°C for a 150mm radius	82
Fig. 4.23	Water temperature contour at a bottom temperature of 40°C for a 150mm radius	83

Fig. 4.24	Water temperature plot at a bottom temperature of 40°C for a 150mm radius	83
Fig. 4.25	Gas mixture temperature contour at a bottom temperature of 45°C for a 150mm radius	84
Fig. 4.26	Gas mixture temperature plot at a bottom temperature of 45°C for a 150mm radius	84
Fig. 4.27	Water temperature contour at a bottom temperature of 45°C for a 150mm radius	85
Fig. 4.28	Water temperature plot at a bottom temperature of 45°C for a 150mm radius	85
Fig. 4.29	Gas mixture temperature contour at a bottom temperature of 50°C for a 150mm radius	86
Fig. 4.30	Gas mixture temperature plot at a bottom temperature of 50°C for a 150mm radius	86
Fig. 4.31	Water temperature contour at a bottom temperature of 50°C for 150mm radius	87
Fig. 4.32	Water temperature plot at a bottom temperature of 50°C for a 150mm radius	87
Fig. 4.33	Gas mixture temperature contour at a bottom temperature of 55°C for a 150mm radius	88
Fig. 4.34	Gas mixture temperature plot at a bottom temperature of 55°C for a 150mm radius	88
Fig. 4.35	Water temperature contour at a bottom temperature of 55°C for a 150mm radius	89
Fig. 4.36	Water temperature plot at a bottom temperature of 55°C for a 150mm radius	89
Fig. 4.37	Gas mixture temperature contour at a bottom temperature of 60°C for a 150mm radius	90
Fig. 4.38	Gas mixture temperature plot at a bottom temperature of 60°C for a 150mm radius	90
Fig. 4.39	Water temperature contour at a bottom temperature of 60°C for a 150mm radius	91
Fig. 4.40	Water temperature plot at a bottom temperature of 60°C for a 150mm radius	91
Fig. 4.41	Gas mixture temperature contour at a bottom temperature of 40°C for a 100mm radius	92

Fig. 4.42	Gas mixture temperature plot at a bottom temperature of 40°C for a 100mm radius	92
Fig. 4.43	Water temperature contour at a bottom temperature of 40°C for a 100mm radius	93
Fig. 4.44	Water temperature plot at a bottom temperature of 40°C for a 100mm radius	93
Fig. 4.45	Gas mixture temperature contour at a bottom temperature of 45°C for a 100mm radius	94
Fig. 4.46	Gas mixture temperature plot at a bottom temperature of 45°C for a 100mm radius	94
Fig. 4.47	Water temperature contour at a bottom temperature of 45°C for a 100mm radius	95
Fig. 4.48	Water temperature plot at a bottom temperature of 45°C for a 100mm radius	95
Fig. 4.49	Gas mixture temperature contour at a bottom temperature of 50°C for a 100mm radius	96
Fig. 4.50	Gas mixture temperature plot at a bottom temperature of 50°C for a 100mm radius	96
Fig. 4.51	Water temperature contour at a bottom temperature of 50°C for a 100mm radius	97
Fig. 4.52	Water temperature plot at a bottom temperature of 50°C for a 100mm radius	97
Fig. 4.53	Gas mixture temperature contour at a bottom temperature of 55°C for a 100mm radius	98
Fig. 4.54	Gas mixture temperature plot at a bottom temperature of 55°C for a 100mm radius	98
Fig. 4.55	Water temperature contour at a bottom temperature of 55°C for a 100mm radius	99
Fig. 4.56	Water temperature plot at a bottom temperature of 55°C for a 100mm radius	99
Fig. 4.57	Gas mixture temperature contour at a bottom temperature of 60°C for a 100mm radius	100
Fig. 4.58	Gas mixture temperature plot at a bottom temperature of 60°C for a 100mm radius	100

Fig. 4.59	Water temperature contour at a bottom temperature of 60°C for a 100mm radius	101
Fig. 4.60	Water temperature plot at a bottom temperature of 60°C for a 100mm radius	101
Fig. 4.61	Water mass flow predicted by CFD simulation for 100mm radius model	102
Fig. 4.62	Water mass flow predicted by CFD simulation for 150mm radius model	103
Fig. 4.63	Water mass flow predicted by CFD simulation for 200mm radius model	103
Fig. 4.64	Rate of fresh water production from experimental data and simulation result for 200mm radius	105
Fig. 4.65	Rate of fresh water production from experimental data and simulation result for 150mm radius	105
Fig. 4.66	Rate of fresh water production from experimental data and simulation result for 100mm radius	106
Fig. 4.67	Gas mixture velocity on a plane inside the solar still for 100mm radius	107
Fig. 4.68	Gas mixture velocity on a plane inside the solar still for 150mm radius	107
Fig. 4.69	Gas mixture velocity on a plane inside the solar still for 200mm radius	108
Fig. 4.70	Accumulative productivity of full-TSS models with constant tray dimensions	109
Fig. 4.71	Accumulative productivity of full-TSS models with constant tray dimensions with respect to volume of humid air	110
Fig. 4.72	Accumulative productivity of half-TSS models with constant tray dimensions	111
Fig. 4.73	Accumulative productivity of half-TSS models with constant tray dimensions with respect to volume of humid air	111
Fig. 4.74	Accumulative productivity of half-TSS models with variable tray dimensions	112
Fig. 4.75	Accumulative productivity of half-TSS models with variable tray dimensions with respect to volume of humid air	113
Fig. 4.76	Water temperature predicted by the CFD simulation and experimental data for 100mm radius	114

Fig. 4.77	Water temperature predicted by the CFD simulation and experimental data for 150mm radius	114
Fig. 4.78	Water temperature predicted by the CFD simulation and experimental data for 200mm radius	115
Fig. 5.1	Comparison between three TSS models for the three experiments with the same 200mm radius Vs the volume of humid air	119

List of Tables

Table 1.1	Some of indirect solar desalination pilot plants implemented at different locations	6
Table 3.1	Dimensions of three TSS models	`57
Table 3.2	Mesh Statistics	66

List of Symbols

C	Unknown constant in the Nusselt number expression
Gr	Grashof number
L	Latent heat of vaporization of water, J/Kg
L_V	Characteristic dimension of condensing cover, m or it is the average spacing between water surface and glass cover, m
K_V	Thermal conductivity of humid air (W/m K)
H_{ew}	Evaporative heat Transfer coefficient(W/m^2 K)
H_{CW}	Convective heat Transfer coefficient from water to condensing cover (W/m^2 K)
Pr	Prandtl number
P_w	Partial saturated vapor pressure at water temperature, N/m^2
P_g	Partial saturated vapor pressure at condensing cover temperature N/m^2
Nu	Nusselt number
$\dot{m}_{ew}$	Distillate output kg/m^2 sec
N	Unknown constant in the Nusselt number expression
q_{ew}	Rate of evaporative heat transfer W/m2
R	Volume fraction, dimensionless
K	Thermal conductivity
F_{LG}	Rate of interphase mass transfer, kg/m3s
A_W	Evaporative surface area
V	Velocity vector, m/s
t	Time interval in sec
T_W	Water temperature, $^{\circ}C$
T_g	Inner temperature of condensing cover, $^{\circ}C$
RO	Reverse osmosis
CFD	Computational fluid dynamics
TDS	Total Dissolved Solids

Greek Symbols

α	Thermal Diffusivity ($m^2\ s^{-1}$)
Δ	Change in
∇^2	Laplacian (a scalar differential operator)
λ	Wavelength (m)
B	Coefficient of Thermal Expansivity (K^{-1})
M	Dynamic Viscosity ($kg\ m^{-1}\ s^{-1}$)

`

CHAPTER 1
INTRODUCTION

1.1 WATER SHORTAGE

Water scarcity already affects every continent. Around 1.2 billion people or almost one-fifth of the world's population, live in areas of physical scarcity, and 500 million people are approaching this situation. Another 1.6 billion people, or almost one quarter of the world's population, face economic water shortage (where countries lack the necessary infrastructure to take water from rivers and aquifers). Water scarcity is among the main problems to be faced by many societies. Water use has been growing at more than twice the rate of population increase in the last century, and although there is no global water scarcity as such, an increasing number of regions are chronically short of water. Water shortage is both a natural and a human-made phenomenon. There is enough freshwater on the planet for seven billion people but it is distributed unevenly and too much of it is wasted, polluted and unsustainably managed. Water scarcity is defined as the point at which the aggregate impact of all users impinges on the supply or quality of water under prevailing institutional arrangements to the extent that the demand by all sectors, including the environment, cannot be satisfied fully. Water scarcity is a relative concept and can occur at any level of

supply or demand. Scarcity may be a social construct (a product of affluence, expectations and customary behavior) or the consequence of altered supply patterns-stemming from climate change [1]. One of the major problems for the whole world and, and particular in the third world, is the availability of pure, clean and healthy water, especially in remote areas. Desalination systems using traditional fuels have been utilized in many countries in the Middle and Near East to produce fresh water. It is interesting to note that many of these countries where desalination has been used extensively are characterized by a high intensity of incident solar energy [2]. Water is considered one of the prime elements responsible for life on earth. It covers three-fourths of the surface of the earth. However, most of earth's water is found in oceans as salt water, which contains too much salt and consequently cannot be used for human consumption, farming or most industrial uses. The remaining earth's water supply is fresh water. Globally, 200 million hours are spent each day, mostly by females, to collect water from distant, often polluted sources. About 3.575 million people die each year from water related diseases [3]. The performance of solar distillation systems depends on climatic parameters such as ambient temperature, solar radiation intensity, weather condition etc. Design parameters, like inclination angle, and operational parameters, such as orientation of solar still and brine water depth [4]. It has been found that with the increment in solar radiation intensity [5] and ambient temperature, the productivity of the

solar still increases [5], [6]. For Middle Eastern countries, sun has a good presence, especially in the huge area of the desert. Sun is considered one of the most important natural, renewable and clean sources of thermal energy and considered very important for life. The idea of using solar energy systems with desalinating plants is considerably helpful and good for the environment.

1.2 SOLAR DESALINATION SYSTEMS AS A CHOICE

Desalination of sea water is considered the most important method to free water from salt and impurities, and makes water ready to be used for human needs. However, the desalination process consumes a huge amount of thermal energy based on the amount of productivity produced. The use of solar energy in thermal desalination processes is one of the most promising applications for renewable energies. Countries in the southern Mediterranean basin (Egypt), usually have abundant seawater resources and a good level of solar radiation, which could be used to produce drinking water from seawater. Figure (1.1) shows the good presence of the solar radiation in Egypt. It is pinpointed on the figure that an amount of 66.9kWh/m^2 per day of global radiation is measured in the Middle East countries [7]. Solar desalination can either be direct, using solar energy to produce distillate directly in the solar collector, or indirect combining conventional desalination techniques, such as multistage flash desalination (MSF), vapor compression (VC),

reverse osmosis (RO), membrane distillation (MD) and electro-dialysis (ED), with solar collectors for heat generation. Solar thermal energy coupled to a power cycle by using direct mechanical power can also be employed [8]. Figure (1.2) shows a flow chart of renewable energies powered by different types of desalination processes [9]. It is clear from the figure that solar energy can be powered by thermal and electrical desalination systems. Solar desalination is particularly important for locations with a scarcity of fresh water and a high solar intensity [10]. In this section; a review of using solar energy with desalination techniques is investigated. Table 1.1 illustrates several desalination processes combined with solar energy.

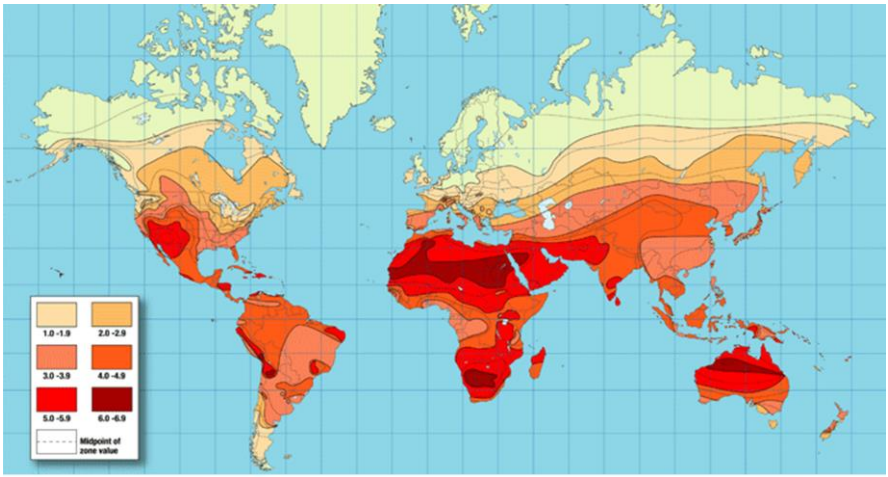

Fig 1.1: World solar radiation [7]

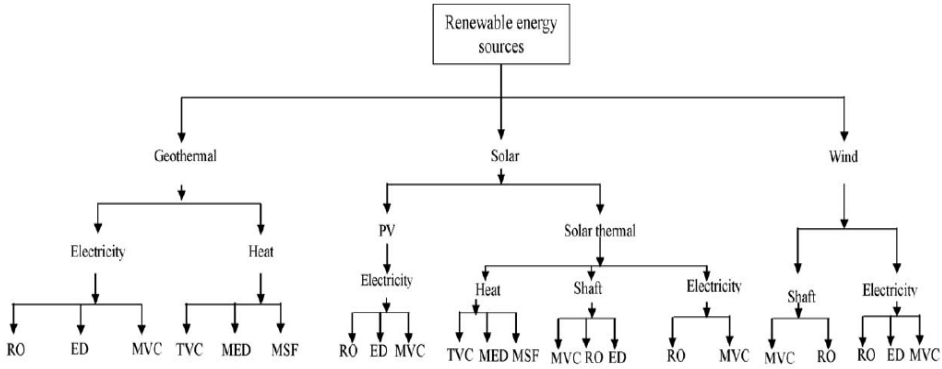

PV= Photovoltaic, RO= Reverse osmosis, ED= Electrodialysis, MVC= Mechanical vapor compression, MED= Multi effect distillation, MSF= Multi stage flash distillation, TVC= Thermal vapor compression

Fig. 1.2 Flowchart of desalination processes powered by renewable energies [11]

1.3 DESALINATION TECHNIQUES

Desalination is one of several processes for removing dissolved salts and impurities from brackish water or seawater to produce fresh water for irrigation or human consumption. There are too many ways that can be used to remove dissolved minerals from hard water, the most commonly used techniques for desalination are:

a) Membrane Desalination (RO).
b) The Evaporative Technique.

Table 1.1: Some of the indirect solar desalination pilot plants at different locations

Desalination process type	Location	Capacity	Type of power	Reference
MSF+MED	Al-Ain, UAE	500m^3/day	Parabolic trough collectors	[12]
PV+RO	Al-Ain, UAE	1m^3/day	PV	[13]
MSF	Kuwait	100m^3/day	Parabolic trough collectors	[14]
MSF	La Paz, Mexico	10m^3/day	Flat plate and Parabolic-trough collectors	[15]
MSF	Lampedusa Island, Italy	0.3m^3/day	Low concentration solar collectors	[16]
MSF	Gran Canaria, Spain, France	10m^3/day	Low concentration solar collectors	[17]
MSF	Al Azhar University in Gaza	0.2m^3/day	Thermal collectors and PV cells	[18]
MSF	Germany	10m^3/day	——	[19]
MSF	Safat, Kuwait	10m^3/day	Solar collectors	[20]

1.3.1 Membrane Desalination (RO)

Membrane Desalination (RO) is a modern process technology to purify water for a wide range of applications including semiconductors, food processing, biotechnology, pharmaceuticals, power generation,

seawater desalting, and municipal drinking water. With demand for pure water ever increasing, the growth of the reverse osmosis industry is poised to continue growing well into the next century. The driving force of the reverse osmosis process is applied pressure. The amount of energy required for osmotic separation is directly related to the salinity of the solution. Thus, more energy is required to produce the same amount of water from solutions with higher concentrations of salt. In the last few years RO seawater desalination technology has gone through a remarkable transformation. The number and capacity of large RO plants have increased significantly. Systems with permeate capacity up to 300,000 m^3/d are currently being built. The cost of desalted water, which is supplied to the costumer, has dropped down from \$2.0/m^3 in 1998 to current price (2004) of about \$0.5/m^3. This decrease of water cost is even more remarkable if one considers that, on the average, the permeate water quality requirements are more stringent now than they were 5 years ago. The drivers behind these economical improvements are competition and improvement of process and membrane technology [21]. Figure (1.3) outlines the process of Reverse Osmosis. When pressure is applied to the concentrated solution, the water molecules are forced through the semi-permeable membrane, while the contaminants cannot pass [22].

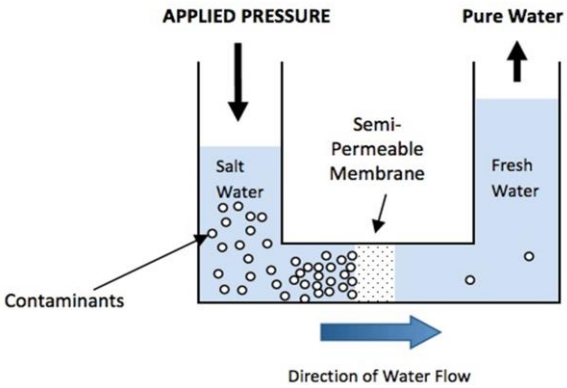

Fig. 1.3 Reverse Osmosis [21]

1.3.2 Evaporation Processes.

Evaporation is the process of liquid becoming vapor, a change in water from liquid form to gas or vapor. The primary pathway that water moves from the liquid state back into the water cycle as atmospheric water vapor. When the brackish water is evaporated, water gets converted into a vapor which is condensed to obtain potable water in liquid state. The evaporative process can be promoted by different techniques of solar desalination commercial systems, such as multi-stage flash distillation. In a multi-stage flash distillation, the feed water is heated up and pressurized to the plant's maximum allowable temperature, and is then discharged to a chamber which is maintained at a pressure slightly below the saturation vapor pressure of water. This will then cause some of the water to 'flash' into steam and get condensed to obtain fresh water. The average energy requirement for a multistage flash distillation is significantly higher than the reverse osmosis process. Moreover, multiple-effect distillation is

another energy-efficient method for water desalination as it uses the heat energy from the water vapor when it condenses to preheat the subsequent water. The high latent heat of water which is transferred to preheat the next stage of water does significantly reduce the overall system's energy requirement for water evaporation. Currently, the average energy requirements for a multistage flash distillation are about 47.5-52kWh/kL [23]. Which is dramatically higher than the reverse osmosis process.

1.4 EVAPORATION BEHAVIOUR

Research was undertaken to understand the behavior of evaporation process for water desalination to find out what rules and factors that control it. Also the previous studies of the mathematical models which will be used to study these desalination behaviors.

1.4.1 Evaporation Theory

In the evaporation process water gets converted into water vapor, when the molecules on the surface of the liquid gain sufficient kinetic energy to overcome the liquid phase of the intermolecular forces. The rate of evaporation increases with high overall kinetic energy of the molecule. Evaporation can also be determined through observing the equilibrium vapor pressure. Evaporation occurs when the equilibrium vapor pressure, which is proportional to temperature, is equivalent or

higher than the atmospheric pressure. Evaporation highly depends upon the kinetic energy of the molecules [24].

The factors influencing the evaporation are as below:

i. Liquid temperature

Increasing the liquid temperature gives the molecules more energy. The more energy a particle has, the faster it moves. Particles in a liquid that acquire increased energy have the ability to break free of the surface of the liquid and convert to a gaseous state.

ii. Pressure

Controlling the liquid pressure is a feature that is used to control the evaporating point of a liquid. A lower atmospheric pressure will cause the liquid to evaporate faster than high atmospheric pressures.

iii. Surface area

There is a positive relationship between the evaporation and surface area. As the evaporation process increases with the increasing of the surface area.

iv. Velocity of air

Water is more likely to evaporate when the air velocity increases. As it decreases the humidity of the air surrounding, where there is more space for evaporating process with less humidity in the surrounding air.

1.5 CONDENSATION BEHAVIOUR

As the solar desalination system was intended to reduce electrical energy requirements, passive cooling methods for condensation were researched too. The suggested condensation method was hot vapor condensing on a cool surface to collect liquid water. This phenomenon was modeled as film condensation. A film condensation analysis is applicable to saturated vapor condensing on a cool surface in which the liquid formed is drained off the surface by the action of gravity [25].

1.6 HISTORICAL BACKGROUND

Methods of solar distillation have been employed by humankind for thousands of years. From early Greek mariners to Persian alchemists, this basic technology has been utilized to produce both freshwater and medicinal distillates. Solar stills were in fact the first method used on a large scale to process contaminated water and convert it to a potable form [26]. In 1870 the first US patent was granted for a solar distillation device to Norman Wheeler and Walton Evans [28]. Two years later in Las Salinas, Chile, the Swedish engineer Charles Wilson, began building a direct method solar powered distillation plant to supply freshwater to workers at a saltpeter and silver mine. It operated continuously for 40 years and produced an average of 22.7 m^3 of distilled water a day using the effluent from mining operations as its feed water [29]. Solar desalination of seawater and brackish groundwater in the modern United

States extends back to the early 1950s when Congress passed the Conversion of Saline Water Act, which led to the establishment of the Office of Saline Water (OSW) in 1955. The OSW's main function was to administer funds for research and development of desalination projects [30]. One of the five demonstration plants constructed was located in Daytona Beach, Florida and devoted to exploring methods of solar distillation. Many of the projects were aimed at solving water scarcity issues in remote desert and coastal communities [29]. In the 1960s and 70's several modern solar distillations plants were constructed on the Greek isles with capacities ranging from 2000 to 8500 m^3/day [26]. In 1984 a MED plant was constructed in Abu-Dhabi with a capacity of 120 m^3/day and is still in operation [29]. Of the estimated 22 million m^3 of freshwater being produced a day through desalination processes worldwide, less than 1% is made using solar energy [26]. The prevailing methods of desalination, MSF and RO, are energy intensive and rely heavily on fossil fuels [27]. Because of inexpensive methods of freshwater delivery and abundant low cost energy resources, solar distillation has, up to this point, been viewed as cost prohibitive and impractical [26]. It is estimated that desalination plants powered by conventional fuels consume the equivalent of 203 million tons of fuel a year [26]. With the approach (or passage) of peak oil production, fossil fuel prices will continue to increase as those resources decline. As a

result solar energy will become a more attractive alternative for achieving the world's desalination needs [31].

1.7 WHAT IS SOLAR STILL

A wide, shallow pan painted black is used as an ideal vessel for the water distillation. It is made wide and shallow to increase the surface area so that it can trap maximum solar energy. The painted surface is baked in the sun to free volatile toxicants which might otherwise evaporate and condense along with the drinking water. The pan is painted black or with some other dark color, to maximize the amount of solar energy absorbed and to increase water temperature so the rate of evaporation can be accelerated. To capture and condense the evaporated water, some kind of surface close to the heated salt water, which are several degrees cooler than the water. The evaporating pan is usually covered by a sheet of clear glass or translucent plastic or glass (to allow sunlight to reach the water) which is tilted to a slight angle to let the fresh water that condenses on its underside trickle down to a collecting trough [32]. The glass creates a cavity and also holds the heat inside. Figure 1.4 shows components of a solar still design.

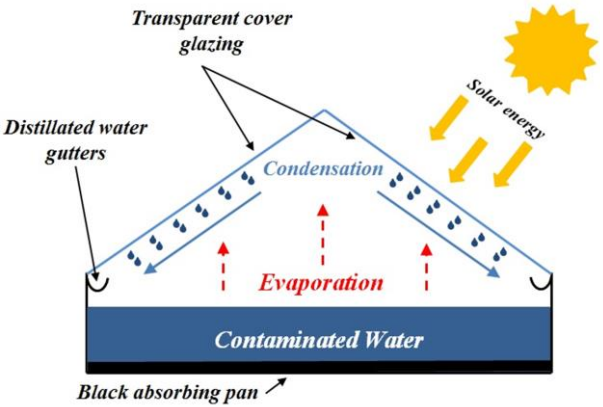

Fig. 1.4 Conventional solar still [15]

1.8 TYPES OF SOLAR STILL:

Classification of solar desalination systems:

1) In terms of energy supply
    a. Active solar still
    b. Passive solar still
2) In terms of structure of the conventional solar still
    a. Single basin solar still
    b. Single-slope double-basin solar still
    c. Single-slope triple-basin solar still
    d. Pyramid-shaped solar still
    e. Conventional solar still with sponge cubes in basin
    f. Double-slope single-basin solar still.

1.8.1 Active and passive solar still

In terms of energy supply, solar desalination systems are classified into two groups: active and passive solar stills. Passive solar still are conventional systems that use the solar energy as the only source of solar energy. However, in the active solar still, extra energy supply is given to the passive solar still for improving the evaporation process and make it faster. This extra thermal energy is added by several ways such as thermal energy from any available industrial plant waste, like industry or even a solar collector.

1.8.2 Solar still design

Solar still designs range from the simple to high-tech. Practical design for a solar still is the single-basin type.

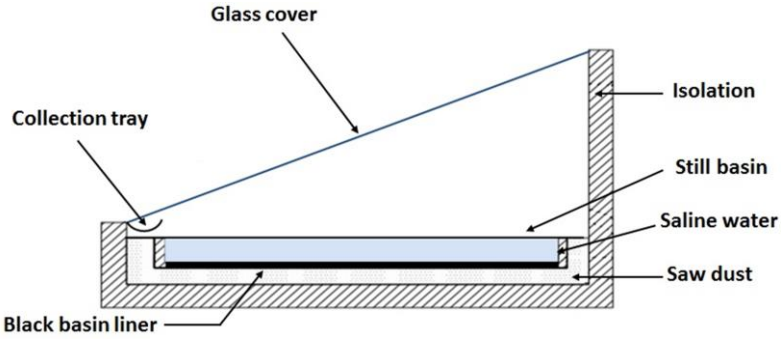

Fig. 1.5 Single-basin type solar still [38]

1.8.2.1 Single basin type solar still

The solar still consists of a galvanized iron steel sheet basin which contains the saline water. The basin top is covered by transparent material e.g. glass. Normally the interior side of the basin is painted with dark color to maximize the absorption process of solar energy. When the solar radiation passes through the transparent cover of the still, it is absorbed by the darkened bottom of the basin. The saline water starts to heat up and evaporate. The air between the glass cover and the water surface is trapped and saturated with moisture. The base also radiates energy in the infra-red region, which is reflected back into the still by the glass cover. The evaporated water is condensed on the interior surface of the glass cover to trickle down on the inclined glass into the collecting tray.

1.8.2.2 Solar still concave surface

A concave-shaped wick surface increases an evaporation rate because the water surface level is lower than the upper limit of the wick surface (Figure 1.6). Results show that average distillate productivity in day time was 4.1 L/m^2 and the maximum instantaneous system efficiency was found to be 45% and the daily efficiency of the still was 30%. The maximum hourly yield was 0.5 L/h per m^2 after solar noon [33].

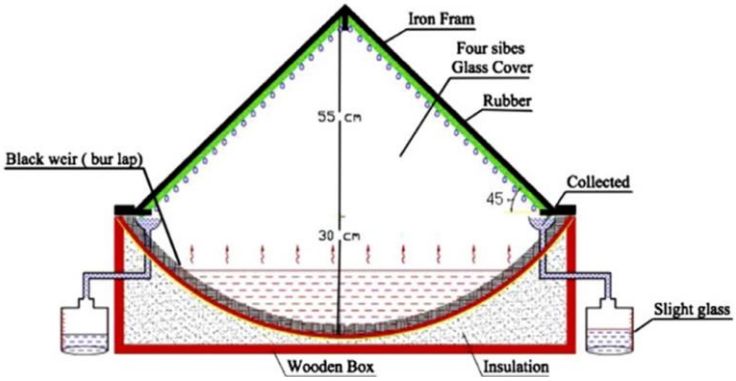

Fig. 1.6 Concave wick solar [33]

1.8.2.3 Double-basin solar still

The first basin glass cover is used as the base for the second basin with the advantage that the heat of condensation from the first basin cover is used to heat the water on the bottom of the second basin (Figure. 1.7) [34].

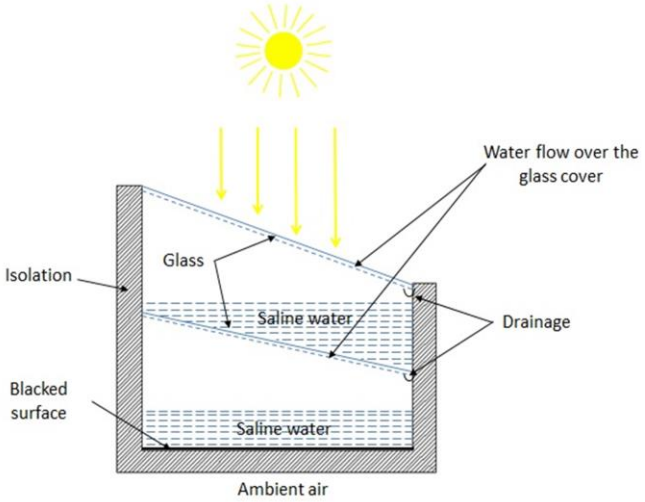

Fig. 1.7 Double-basin solar still [34]

1.8.2.4 Hemispherical solar still

A hemispherical solar still is filled with saline water. The top hemispherical cover is made of transparent acrylic sheet with high solar transmittance. The outer box of the still is made of wood. The bottom of the basin was filled with sawdust. The sides of the basin are isolated by glass wool to reduce the conduction heat loss through the sides of the still, variation in the insulation value can have a 10% effect on overall of productivity. [35]

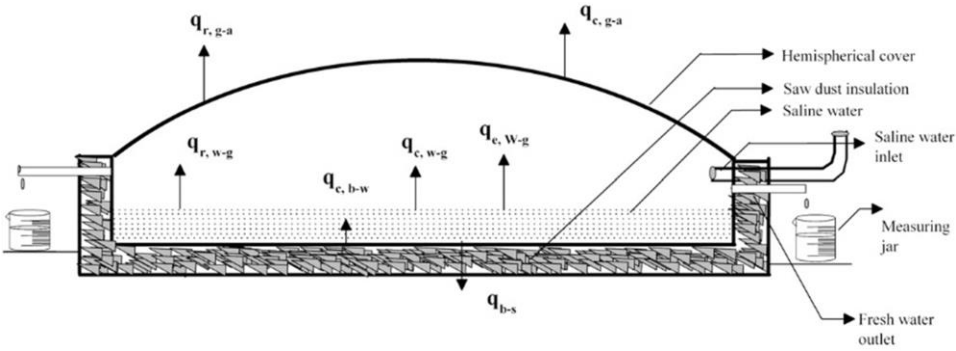

Fig. 1.8 Cross sectional view of a hemispherical solar still [35]

1.9 SOLAR COLLECTORS

The solar thermal collector is a device which captures sunlight radiation and converts it into a usable form for solar plants. A solar collector is a relatively low cost heat exchanger that absorbs the sunlight radiation and transforms it into heat, then transfers this heat to the desired medium, e.g. (water, air, ... etc.) to be heated up. One of the main ways a

solar collector can be made more efficient is by using a transport medium that is different than the material that heated up. While water itself makes a perfectly usable medium, many people prefer to use something different, depending on the environmental situation.

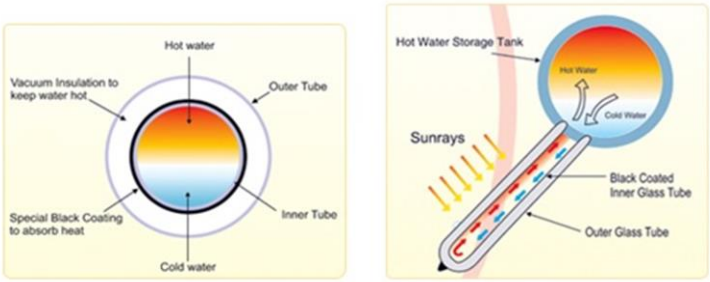

Fig. 1.9 Solar Water Heater [36]

1.10 CFD MODELING

CFD is the abbreviation for Computational Fluid Dynamics. It is one of the fluid dynamic branches that uses numerical methods to analyze and solve problems of the fluid flow. CFD simulation provides tools for fast, accurate and flexible flow and thermal analysis, so it can predict product performance before the production, optimize designs and evaluate the product behavior. There is less need for costly physical prototypes, and the launch of innovative products is accelerated. Automation tools and the novel environment for design studies, facilitate the examination and comparison of design alternatives and show the

effects of structural changes on comprehensive. CFD simulation provides even in the early stages of product development to make informed design decisions. High speed computers are used for calculations and to perform the iteration simulations of the fluid with surfaces defined by the boundary conditions (BC). The term Computational Fluid Dynamics (CFD) denotes the numerical simulation of flows. An important form of the basis of conservation laws the physics of mass, pulse and energy (Navier-Stokes equations). Additionally, will but also empirical approaches (turbulence, heat transfer to top, pollutant dispersion, porous media, etc.) uses. The conservation equations lead to a system of partial differential equations, which, in discretized form, in CFD programs with using appropriate algorithms Iterative be solved. We speak of field models because the solution area is typically divided in thousands of control volumes or computational cells. The modeling can be there spatial 2 or 3-dimensional as well as stationary in time state or transient. The Navier-Stokes equations of Claude Louis Marie Henri Navier and George Gabriel Stokes were already developed before 200 years and provide the exact description of flowing fluids. In the direct numerical simulation shall every turbulent fluctuating motion directed by the calculation grid be displayed. This results achieved into that, even at very low turbulence cell numbers of the grid of several billion. Since on normal computers that currently not more than about 5 to 10 million cells expected, the clustering more computers their confines has DNS is

currently limited on few exceptions. The current practice at the most spread strategy is the RANS turbulence modeling (Reynolds Averaged Navier Stokes), the one whole group of equation approaches includes the best known k-model. The two equations of the kinetic energy and the isotropic dissipation rate at many practical issues sufficient and accurate results. Because CFD packages are not only the numerical flow simulation, but also thermal, physical relations and chemical reactions of various phases (e.g. air, water, sand particles) in interaction describe each other. In almost all spheres of activity which involve heat transfer and fluid flow. A number of different softwares based on CFD codes have been developed such as: Fluent, OpenFOAM, Flovent, Icem-CFD, Phoenics, GAMBIT, and CFX. Each software is usually supported by supplementary software for different applications, such as domain model preparation, mesh generation etc. Presently CFD techniques are increasingly used to model flow through solar collectors and solar distillation units.

1.11 OBJECTIVE

The primary concern of this research is to investigate the performance of Tubular Solar Still (TSS). The present study is designed to examine:

1. The temperature distribution of the water and gas mixture by using CFD in different radii of the tubular solar stills (100mm, 150mm, 200mm).

2. A comparison of the performance of three tubular stills with different radii (100mm, 150mm, 200mm).

3. A prediction of the maximum distillate water production rate of the three different radii models with constant try dimensions and variable tray dimensions.

CHAPTER 2

LITERATURE REVIEW

2.1 HISTORICAL BACKGROUND OF DESALINATION

A historical review may help to understand the main concept of desalination procuresses through last centuries. **Delyannis [37]** studied the history of desalination processes. In his research he tried to overview historical paths by focusing on the most important ideas and features developed from antiquity until today on desalination of non-potable with special reference to the use of solar energy for desalination. He found that the sun was especially glorified by the Egyptians, Greeks, and Incas. Looking at the history of mankind, can find that energy and water are correlative items that govern that govern the rise and fall of civilizations.

The desalination concept from pre-historic times to middle ages

Aristotle (384-322), a well- known philosopher and scietist of antiquity already described the origins and properties of natural, brackish and seawater in a surprisingly correct way. He writes for the water cycle in nature: "The sun moving, as it does, sets up processes of becoming and decay, and sweetest water is every day carried out and is dissolved into vapor and rises to the upper regions, where it is condensed again by the cold and so returns to the earth".

Even today no better explanation is given for the water cycle in nature. Really, the water cycle is a huge solar energy open distillation plant. Mouchot (1869, 1879) the well-known French scientist who experimented with solar energy, mentions in one of his numerous books that during medieval time, Arab alchemists carried out experiments with polished Damascus concave mirrors to focus solar radiation onto glass vessels containing salt water in order to produce fresh water.

The development of solar desalination during the Renaissance period

Later on during the Renaissance, Giovani Batista Della Porta (1535–1615), one of the most important scientists of his time wrote many books in the volume on distillation. He mentions seven methods of desalination, but the most important reference is in the 19th volume,

DE DISTILLATIONIBVS. 185

hæc in latus fidelias aquæ plenas immittut, vt citiùs vapores in aquam crassescant. Optimè omnia iam parata, obuerte ad intentissimũ solarium radiorum æstum: nam extemplo in vapores soluuntur, & gutatim in subiecta vasa stillabunt. Vesperi post Solis occasum remoue, ac nouis herbis reple. Herba pe ligonus, siue *lingua passerina* vulgò vocata, concisa, extillatuq;, maximè oculorum inflammationibus præstat, aliisq; morbis. Ex hiperico elicitur aqua omne spasmum profligatura, ũ dolens membra ea abluerit: & alia, quæ longum esset recensere. Modus distillandi pictura prostat.

Fig. 2.1 Della Porta solar distillation apparatus [37]

he describes a solar distillation apparatus that converted brackish water into fresh water (Della Porta). Figure (2.1) shows the Della Porta solar distillation unit. He also describes, in the second chapter of volume 20, a method to obtain fresh water from the air (nowadays called the humidification– dehumidification method).

In 1870 the first American patent on solar distillation was granted to Wheeler and Evans. the inventors who described the greenhouse effect, analyzed in detail the cover condensation and re-evaporation, discussed the dark surface absorption and the possibility of corrosion problems. High operating temperatures were claimed also as means of rotating the still in order to follow the solar incident radiation. Two years later, in 1872, an engineer from Sweden, Carlos Wilson, designed and built the first large solar distillation plant in Las Salinas, Chile (Harding, 1883).

Abdul Jabbar N. Khalifa et al. [38] conducted an experiment to investigate the effect of the isolation thickness of the solar still productivity. Heat losses from all sides of the basin should be reduced to maximize the efficiency of the still. A comparison was made between a study of solar stills with insulation thickness of 30, 60 and 100mm and with solar stills without insolation. It was found that there is a dramatic difference in productivity. The insulation thickness could influence the productivity of the still by over 80%. A number of research works were carried out and nearly all studies reported improvement in the

productivity of stills due to the use of isolation. The maximum thickness of insulation that was examined in these studies is 100 mm, which indicates a general agreement between the investigators about the maximum practical thickness. However, they disagree about the limit of the optimum thickness. This limit is ranging from 40 to 100 mm of insulation thickness. A performance correlation for the effect of insulation on productivity is also developed in this experiment. Batch feeding of water with salinity ranging from 1100 to 1400 ppm was used in these tests, a cover tilt angle of 35° and a brine depth of 40 mm were kept unchanged in all tests. It was found that perfect insulation of solar stills increases the maximum brine temperature by 67%. One of the reasons behind the increase in the daily productivity was the increase in the nocturnal production due to the continuous production during off sunshine hours. The nocturnal production output was increased from 0.2 l for uninsulated still to 0.45, 0.55, and 0.6 L for stills with insulation thickness of 30, 60 and 100 mm, respectively. The experimental results show that insulation could influence the productivity of the still by over 80%; the productivity is increased from 1.81 L/m^2 per day for a still with no insulation to 3.28 L/m^2 per day for a still with an insulation thickness of 60 mm and 100 mm of the insulated stills.

The experimental data shows the productivity as a function of the insulation thickness.

$$y = 1023(t)^3 - 408.8(t)^2 + 45.34(t) + 1.81, \qquad R^2 = 1 \qquad (2.1)$$

where (y) is the productivity (l/m^2 day) and (t) is the insulation thickness (m), (Root Mean square value R^2)

A. Safwat Nafey et al. [39] investigated the productivity enhancement of solar still on either side theoretically and experimentally by adding floating perforated black plate to the brackish water in different brine depths (3, 4, 5, 6mm) under the same conditions. The floating perforated black aluminum plate is appointed to maintain film evaporation in the solar still. In this work, a comparison between the theoretical and the experimental results was achieved. The results of the developed mathematical model was in good harmony with the experimental results. Two units of a single sloped solar still are designed and constructed to maintain the comparison under the same weather conditions. The inner sides of the boxes were coated white to reflect solar radiation to the water surface while the base of the units were coated with black coating to absorb solar radiation. Only the base of each unit is insulated with foam (thermal conductivity = 0.04 W/m K) of 4 cm thickness. The condensation surface used was 3mm glass with fixed inclination of 15° for both stills. The used perforated aluminum sheet had to meet certain requirements, such as high degree of blackness and ability to float on the

water surface. These requirements are satisfied by using a liner of aluminum sheet of 0.5 mm thickness. This sheet was painted black. Holes with a 0.5mm diameter are made. To facilitate floating on the brine surface, five floating balls are stacked on the underside surface of the plate. The two units were oriented with its face to the south. Results showed that the productivity of the solar still depends on the brine depths. As the brine depth increases, the total productivity decreases, and this might be due to the higher thermal capacity of the water. The result also showed that, the slope of the curves of the experimental and theoretical results of the floating plate still unit is less than that of the plain water still. This may be because using floating perforated black plate which decreases the temperature of the bottom layer. Hence, the thermal energy stored at any brine depth is decreased. So, it can be said that the productivity in the case of the floating plate decreases with increasing brine depth. This is partly owing to the increase in heat loss through the glass and partly due to the increase in thermal capacity of the bottom water. The obtained theoretical and experimental results show that at a brine depth of 3cm, the increase in productivity amounted to 15% and to 40% at 6cm of brine depth. The higher percentage in productivity is obtained in the higher brine depth because the floating plate has the advantage of maintaining the thermal energy in the water below it in a small quantity with respect to that in the plain water still. It can be said

that using a floating perforated black plate in a solar still at a brine depth of 6 cm enhances the productivity by nearly 40% approximately.

Hiroshi Tanaka [40] presented a theoretical analysis in this study for a basin type solar still with internal and external reflectors. The external reflector is a flat plate that extends from the back wall of the still and can be manually inclined forwards or backwards according to the sun. A report of a theoretical prediction of the daily amount of distillate produced by the still throughout the year was combined with this study according to previous studies, which varies according to the inclination angle of both the glass cover and the external reflector, at 30°N latitude. An optimum inclination angle of 10-50° was found for each month for the external reflector of the still. The increase in the average daily amount of distillate throughout the year of a still with inclined external reflector with optimum inclination in addition to an internal reflector, compared to a conventional basin type still was predicted to be 29%, 43% or 67% when the glass cover inclination is 10°, 30° or 50° and the length of external reflector is half the still's length.

Akash et al [40] studied the effect of absorbing materials on the performance of a double slope single basin solar still in an assay to enhance the productivity of distillate water and observed that the productivity was enhanced by 38% by adding an absorbing black rubber mat to the basin. Using black ink increased it by 45% and by using Black

dye (being the best absorbing material) the water productivity was enhanced by 60%.

Shankar and Kumar [41] studied the parameters affecting the productivity of the single passive solar still such as operation parameters, design parameters and the climate parameters. It was found that the exegetic efficiency and the energetic efficiency boosted from 0.4% to 10.7% with boost in the value of $\frac{T_{WO}-T_a}{I_s\ (t)}$ from 0.014 to 0.115, reduced by 21.8% and 36.7% respectively with reduction in basin liner absorptivity from 0.9 to 0.6, reduced by 0.47% to 0.75% respectively with per degree increase in glass cover tilt and increased marginally up to a wind velocity of 2 m/s^2 and after that these remained constant.

Mario and Giovanni [42] designed a simple solar still using transparent thin-walled plastic tubes of ~0.10–0.25m inner diameter to distillate sea water. The designed model was divided into evaporation and condensation sections. The evaporation section contains horizontal transparent tubes. The tubes are half filled with sea water which absorbs solar radiation. The condensation section is separated from the evaporation section in a shaded space below it and includes the horizontal glass tubes of ~0.01m inner diameter. The wall thickness of the condensing plastic tubes is ~50 μm. The enhanced fresh water productivity was reported with respect to previous studies of conventional solar stills in which sea water evaporation and water vapor

condensation occur in one confined space. The study analyzed the technological features of their proposed tubular solar still in details with a specific view to clarify relevant aspects concerning transparent and impermeable construction materials, assembly procedures and roll of various operating parameters.

Arjunan et. al. [43] carried out an experimental study on a try to store the excess solar radiation energy by putting blue stones in the hearth of the still. It was observed that the productivity of the still is influenced by the internal and external heat transfer with keeping the glass cover at 10° tilt angle, paralleled with a conventional still and there is 5 % increase in the productivity of the modified solar still when using blue metal stones as a storage medium. They observed that the maximum amount of heat loss that takes place in the solar still is a mixed effect of convective and radiation heat transfer from glass to ambient.

Tiwari and Ashok Kumar [44] conducted an experimental study on the tubular solar still design suggested by Tleimat and Howe. The still consists of a rectangular black metallic tray (0.1m x 1.1m x 0.0127m) placed at the diametric plane of a cylindrical glass tube. The length and diameter of the glass tube are slightly greater than the length and width of the tray. During operation, the ends of the glass tube are sealed with wooden plates. The tray and glass tube are fixed slightly tilted from the horizontal plane but in opposite direction. Brine fed from one end is

partly evaporated. The evaporated water condensed on the inside walls of the glass cover flows down and it is collected from one end at the bottom of the glass tube. It was observed that, (i) the daily yield of distillate in the tubular solar still is higher than that of the conventional solar still for the same set of still and climatic parameters. (ii) The average brine temperature is independent of still length for higher flow rate while the output temperature of brine strongly depends on still length. (iii) The purity of the product in the tubular solar still is greater than in a conventional one. (iv) The internal heat transfer coefficient remains constant for constant inlet brine temperature in contrast with the conventional solar still for higher flow rates.

A.K. Tiwari and G.N. Tiwari [45] conducted an experimental study for five days for five different water depths from 0.04m to 0.18m. They observed the effect of water depth on evaporative mass transfer coefficient. The hourly average values of h_{cw} , h_{ew} , h_{cw_dunk} , h_{ew_dunk} calculated by using experimental data. Fluctuation in water temperature were higher at low water depth, with increase in water depth the alternation in water temperature decreased due to storage effect. The higher the water depth, the more time water will take to exceed the glass temperature and ultimately the glass temperature will be higher due to solar radiation, with negative value of ΔT. On the other hand, the higher depth of water once ΔT became positive it remained positive till next sunrise. For lower water depth ΔT became positive very soon at 12 noon.

Whereas for higher water depth ΔT became positive at 3 pm, 3 hours later. The higher the water depth, the more energy was stored within the water in the form of sensible heat and lesser rise in temperature of water surface. They finally concluded that heat transfer coefficient depends significantly on water depth.

Mahmoud. I.M. Shatat, K. Mahkamov [46] investigated the performance of a multi-stage water desalination still connected to a heat pipe evacuated tube solar collector with an aperture area of $1.7m^2$. The multi-stage solar still water desalination system was designed to recover latent heat from evaporation and condensation processes in four stages. The variation in the solar radiation during a typical mid-summer day in the Middle East region was simulated on the test rig using an array of 110 halogen floodlights covering the area of the collector. The results of tests demonstrated that the system produces about 9kg of fresh water per day and has a solar collector efficiency of about 68%. However, the overall efficiency of the laboratory test rig at this stage of the investigations was found to be at the level of 33% due to excessive heat losses in the system. The analysis of the distilled water showed that its quality was within the World Health Organization guidelines. The still's operation was numerically simulated by employing a mathematical model based on a system of ordinary energy and mass conservation differential equations written for each stage of the still. A computer program was developed for transient simulations of the evaporation and condensation processes

inside the multi-stage still. Experimental results obtained and theoretical predictions were found to be in good agreement.

Sodha et al. [47] presented the results of experimental study of waste hot water for desalination. The study was on two modes: (i) Feeding hot waste water obtained from thermal power plants once a day, (ii) flowing hot waste water from thermal power plants at constant rate through the solar still. It was clear that the depth of water in the basin, solar radiation, length of the still and inlet water temperature are the parameters which affects the performance of the still and the still fed with hot water at constant rates gives higher yield in comparison to a still with hot water filled only once a day.

Ganeshan and Nirmalakhandan [48] designed a solar still which maintained a vacuum in the evaporating chamber, exploiting the natural gravity law and the barometric pressure head and developed a model. They demonstrated that the correlation between the predictions made by the theoretical model and the measured performance data and produced a yield of 7.5L/m^2 day of evaporation area using direct solar energy alone. With the addition of (PV/T) panel of 6m^2 area their system produced 12L/m^2 day of fresh water at an efficiency range of 65% to 90%. The average specific energy feed was calculated as 2930 kJ/Kg of fresh water.

Al-Kharabsheh, Yogi Goswami [49] studied utilizing vacuum conditions for evaporation and condensation. Vacuum is created using

natural forces of gravity and atmospheric pressure. The proposed desalination system consisted of a solar heating system, and an evaporation chamber and a condenser. The condenser is placed 10m above the ground level and connected to saline water via connected pipes. By balancing the atmospheric and the hydrostatic pressures in the supply and discharge pipes, the distillation of water at a lower temperature level requires less thermal energy. This heat can be provided from solar collectors, which will operate at a higher efficiency because of lower collector operating temperatures. Simple flat plate collectors may be used to heat the saline water in the evaporator. As a result of evaporating the saline water, the salinity increases which causes a decreasing in evaporation rate, which is why it is necessary to withdraw the brine at a certain flow rate. As saline water in the evaporator starts evaporating, its salinity increases which tends to decrease evaporation rate, so it becomes necessary to withdraw the concentrated brine at a certain flow rate and inject saline water at a rate equivalent to the withdrawal plus evaporation rates. The withdrawn water will be at a temperature equal to that of the evaporator, so it becomes necessary to recover the energy from it. A tube-in-tube heat exchanger is used for this purpose, where injected water flows inside the inner tube and withdrawn water will flow in the annulus in a countercurrent direction. Water can be injected by the atmospheric pressure under the influence of vacuum conditions. This makes the proposed system a continuous process type. It was found that the effects

of withdrawal rate and the depth of water in the evaporator were small, while the effect of heat source temperature was significant. Based on theoretical simulations the present system would perform much better than a simple flat basin solar still.

Tiwari et al. [50] developed the thermal models for all types of solar collector integrated active solar stills based on energy balance equations in terms of inner and outer glass temperature. They studied the total daily yield of passive solar still, FPC, concentrating collector, ETC and ETC with heat pipe. The authors have drawn the following points: (i) The overall average thermal and exergy efficiency of FPC integrated active solar stills are in the range of 5.6–19.1 and 0.25–0.85%, respectively. (ii) The overall thermal efficiency of active solar stills integrated with FPC, concentrating collector, ETC and ETC with heat pipe is 13.14%, 17.57%, 17.22% and 18.26%, respectively. (iii) the maximum values of total heat transfer coefficient (h_{tw}) for active solar stills integrated with flat plate collector, concentrating collector, evacuated tube collector and ETC with heat pipe are 43, 86, 67 and 76 W m^{-2} C^{-1}, respectively. If the exergy out of FPC is considered, then average exergy efficiency of active solar stills varies in the range 0.59–1.82%.

2.2 PARAMETRIC STUDY

There are a number of parameters which affect the performance of a solar still. These are broadly classified as [21]:

(i) Climatic parameters.

(ii) Design parameters.

(iii) Operating parameters.

2.2.1 Climatic Parameters

- Solar Radiation
- Wind Speed
- Sky Conditions
- Ambient Temperature
- Outside Humidity

2.2.2 Design Parameters

- Single slope or double slope
- Type of solar still
- Orientation of still
- Inclination of glazing
- Water depth in basin
- Bottom insulation
- Glazing material
- Spacing between water and glazing

2.2.3 Operational Parameters

- Water depth
- Coloring of water
- Rate of algae growth
- Salinity of water
- Preheating of water
- Input water supply arrangement

`

CHAPTER 3

METHODOLOGY

3.1 INTRODUCTION

Extensive computational fluid dynamics (CFD) codes have been developed in the past few decades to estimate velocity field, temperature and heat transfer in both external and internal flows. However, those CFD codes consume a great deal of computational resources and time to obtain reasonable accurate solutions. In this chapter, a simulation of two phase three dimensional model is developed on TSS. The simulation carried out to explain the assumptions of each step. Size of geometry, meshing, boundary condition applied on the simulation model and simulation procedure has been discussed here with an enhanced contrast. By knowing the thermal properties of the materials used in the solar still, the corresponding thermal impedances, thermal capacitances and heat sources of each component can be calculated and applied into the equivalent thermal CFD model, and to predict the air and vapor temperature rises in the real still. Additionally, those thermal impedances are derived from entirely dimensional information of the still. Hence, the same thermal equivalent thermal model can be easily adapted to a range of machine sizes, boundary conditions and configurations.

3.2 CFD-PROCESS

The CFD-process consists of three vital steps as described in figure (3.1).

Fig. 3.1 General CFD-Process

3.2.1 Pre-processing

The geometry of the TSS is imported from ANSYS v150 File (.agdb). The geometry is then cleaned up depending on the details wanted and the areas of interest. A mesh of triangles are put on to the surface of the geometry, the size for these triangles can be varied. Afterwards, The domain is volume meshed generating a fluid domain in the geometry. Prismatic layers are then built up in order to take into account solids or to resolve boundary layers. This process was performed in ANSYS CFX 15.0.

3.2.2 Solving

The mesh is then exported to the solver were all the physics are set-up and solved by applying appropriate boundary conditions for inlets/outlets and walls in the domain along with its specific physical model. The solver solves the mass, momentum and energy equations throughout the domain together with the specified physical model. The

equations are discretized along the cells of the domain and solved until convergence is reached. ANSYS CFX was used as a solver and for the calculations.

3.2.3 Post-processing

Thereafter the results from the solving are post-processed. This is where you visualize the results by plotting interesting parameters in different ways. Post-processing was performed in ANSYS CFX.

3.3 NUMERICAL SIMULATIONS

This chapter will show how the numerical method was developed. First by giving an introduction to heat transfer and fluid dynamics by giving some general theories for the TSS model by explaining the governing equations and the physical models used in CFX.

3.3.1 Theory

Figure (3.2) below gives an overview of the heat transfer mechanisms that are present in the TSS and its environment. The flow of air inside the TSS depends mainly on natural convection which is forced by the heat from the water vapor. The water vapor will heat the surrounding air and force the hot air to rise and a new colder air enters from below. Radiation from the sun will be absorbed by the bottom of the trough and reflected by the water. Energy will be absorbed by the nearby surfaces and cause the adjacent air to be heated. The heat absorbed by the

surfaces will be transported through the materials by heat conduction. Each mechanism will be described further in the subchapters below.

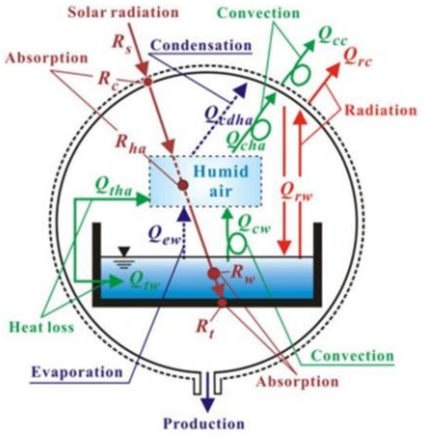

Fig. 3.2 Mass and heat transfer inside and outside of a TSS [52].

3.3.2 Conduction

Heat energy transfers through chain vibration of molecules. In other words, when two regions have a temperature difference, energy is transferred between the two by conduction. Conduction usually takes place in or between interaction surfaces and solids. The heat transport occurs spontaneously from the higher temperature medium to the lower temperature medium due to the temperature gradient between the two. The two regions strive for equilibrium, thus conductive heat transfer will stop when the temperature difference between the two mediums is zero. Heat that is being transferred through a medium by conduction can be expressed by Fourier's law.

$$\dot{q}_x = -k \cdot \frac{\Delta T}{\Delta x} \quad (3.1)$$

where k = thermal conductivity coefficient [W/m K], Δx = wall thickness [m], ΔT = temperature difference between the mediums [K]. Thermal conductivity is a material specific property that defines how much heat that can be transported through the material. Thermal conductivity varies with material temperature. A high thermal k-value indicates good thermal conductivity, meaning that the material conducts more heat.

3.3.3 Convection

Convection is the mechanism where heat is transferred between a solid material and the fluid around it as the fluid flows against the surface of the solid. Heat energy is transferred through the movement of the medium. Convection is a mixture of conduction and the motion of a fluid and as the fluid motion increases, so does the convective heat transfer. When the fluid is in motion, heat is transferred by convection, and when the fluid motion is infinite, heat is transferred by conduction.

$$\frac{dQ_{conv}}{dt} = h \cdot A\,(T_{conv} - T_t) \quad (3.2)$$

Where h = Heat transfer coefficient [W/m^2 K], A = surface area [m^2], T_{conv} = surface temperature [K] and T_t = free stream temperature of the fluid [K]. HTC depends on the surface geometry, the flow field around the surface as well as the fluid properties and velocity.

Natural convection is usually recognized as movement of air induced by temperature changes, and is also known as buoyancy driven flow. As the temperature of the fluid rises, the density will decrease, thus the warmed air will start to move upward, being replaced by colder air moving in from below. Buoyancy driven flows are characterized by constants like the Grashof number which is used to describe the ratio between the viscous forces and the buoyancy forces. The intensity of natural convection can be measured by the magnitude of the Rayleigh number. The Rayleigh number indicates the difference between viscous and buoyancy forces in the fluid and a large value implies strong natural convection effects. The Prandtl number describes the ratio between the fluids kinematic viscosity and thermal diffusivity.

$$G_r = \frac{\beta \cdot g \cdot L^3 \cdot \rho^2 \cdot \Delta T}{\mu^2} \tag{3.3}$$

$$R_a = G_r \cdot P_r = \frac{\beta \cdot g \cdot L^3 \cdot \rho^2 \cdot \Delta T}{\nu \cdot \alpha} \tag{3.4}$$

Where β is the thermal expansion coefficient, g is the gravitational constant, L is the characteristic length, ρ is the density of the fluid, ν is the kinematic viscosity [m^2/s] , α is the thermal diffusivity [m^2/s], ΔT is the temperature difference between the surface and the fluid and μ is the dynamic viscosity. The critical Rayleigh number where transition to turbulence occurs is between 10^8 and 10^9, values above this indicate turbulent flow.

3.3.4 Radiation

Radiation is the heat energy exchange through electromagnetic waves. These waves do not need any medium to be transferred and radiation is therefore fastest in vacuum where nothing restricts the electromagnetic waves. Electromagnetic waves are spread over a wide spectrum of wavelengths where each part of the spectrum has vast differences in their properties compared to other parts of the spectrum. Thermal radiation is emitted by all bodies with a temperature above absolute zero, i.e. above zero degrees Kelvin. The amount of radiation emitted from a body can be expressed by the Stefan-Boltzmann law below.

$$\dot{Q}_{radiation} = \varepsilon \cdot \sigma \cdot A \cdot (T_1^4 - T_2^4) \qquad (3.5)$$

Where ε = Emissivity [-], T_1= surface temperature [K], T_2 = surrounding temperature [K], A = surface area [m^2] and σ = 5.67×10^{-8}[W/m^2 K^4]. Emissivity is a material property and the emissivity of a surface is equal to one for a black body and close to zero for a highly reflective material. The shiny surface of a reflector has an emissivity value between 0,05 to 0,1, while dark colored surfaces have values up to 0,98. Emissivity depends on wavelength, surface temperature and the incoming radiation angle. A surface can emit, transmit or absorb radiation. The absorption which is the amount of radiation is being absorbed by a surface. A body that absorbs all incoming light has an absorption coefficient of one. Absorbing radiation will cause the body temperature to increase. Both the emissivity and absorption depends on the surface temperature and the wavelength of the incoming radiation. On the other hand, these values can be estimated as an average if the surrounding radiation is of the same order of magnitude as the surface temperature, which often is the case. The values are often estimated as constant values for all temperatures and wavelengths, and is called gray body radiation. Transmissivity means that a large amount of the incoming radiation is being transmitted through the material, if the material transmits radiation in the visible range, it is optically transparent. If no transmission of radiation in the visible range occurs, the material is opaque. Light that is being transmitted through a material can also be scattered, scattering mainly depends on impurities or structural disorder and could be seen as a measure of particles and

irregularities in the structure of the material, prohibiting some of the light to be transmitted [53].

3.3.5 Condensation

The air mainly consists of five substances: nitrogen, oxygen, argon, carbon dioxide and water vapor. The amount of water vapor that can be obtained by air can be expressed as the relative humidity (RH) and is limited by the temperature and pressure of the air, thus the maximum relative humidity varies with two parameters. If the pressure drops or the temperature rises when RH=100%, water will deposit from the air and form dew. If air with a relative humidity of 100% gets in contact with a cold object with a surface temperature below the current dew point, water will deposit from the air onto the surface of the object. Condensation is formed as small water droplets and can be seen as fog (as often seen in valleys or at sea after sunrise) or as small droplets on the surface of cold objects such as glass windows or cold soda cans. The condensations phenomena inside TSS can simply be explained by the inner surface of the transparent glass having a temperature equal to or above the current dew point of the air adjacent to the water surface. Most analysis on the subject simplifies the condensation on the inside of the glass as film condensation and this will also be the case regarding this thesis work.

3.4 GOVERNING EQUATIONS

CFD solves the energy , continuity, momentum and mass transfer conservation principles at a steady state condition as are given below.

3.4.1 Energy equation

Liquid phase:

$$\nabla \cdot (\mathrm{r_L}\rho_\mathrm{L}\mathrm{V_L}\mathrm{h_L}) = -\nabla \cdot \mathrm{q} - (\mathrm{Q_{LG}} + S_{LG}h_{LG}) \qquad (3.6)$$

Vapor phase:

$$\nabla \cdot (r_G\rho_G V_G h_G) = -\nabla \cdot \mathrm{q} + (\mathrm{Q_{LG}} + S_{LG}h_{LG}) \qquad (3.7)$$

Where $\mathrm{Q_{LG}}$ is the rate of heat transfer from liquid phase to vapor phase. Also from vapor to liquid phase where $\mathrm{Q_{LG}} = -\mathrm{Q_{LG}}$.

3.4.2 Continuity equation

Liquid phase:

$$\nabla \cdot (r_L\rho_L V_L) - F_{LG} = 0 \qquad (3.8)$$

Vapor phase:

$$\nabla \cdot (r_L\rho_L V_L) + F_{LG} = 0 \qquad (3.9)$$

Where F_{LG} is the mass transfer rate from liquid phase to vapor phase. Also from vapor to liquid phase where $F_{LG} = -F_{LG}$.

3.4.3 Momentum equation

Liquid phase:

$$\nabla \cdot \left(r_L(\rho_L V_L V_L)\right) = -r_L \nabla P_L + \nabla \cdot \left(r_L \mu_{laminar,\ L} (\nabla V_L + (V_L)^T)\right) + r_L \rho_L g - M_{LG} \quad (3.10)$$

Vapor phase:

$$\nabla \cdot \left(r_G(\rho_G V_G V_G)\right) = -r_G \nabla P_G + \nabla \cdot \left(r_G \mu_{laminar,\ G} (\nabla V_G + (V_G)^T)\right) + r_G \rho_G g - M_{LG} \quad (3.11)$$

Where M_{LG} is the interfacial forces acting on each phase.

The evaporative and convective heat transfer coefficients proposed by Dunkle [51] are as follows:

$$h_{ew} = 16.372 \times 10^{-3}\ h_{cw}\ \frac{P_w - P_{gi}}{T_w - T_{gi}} \quad (3.12)$$

$$h_{cw} = 0.884 \left[T_w - T_{ig} + \frac{(P_w - P_{ig}) + T_w}{268.9 \times 10^{-3} - P_w}\right]^{1/3} \quad (3.13)$$

As the rate of water evaporation was assumed to be equal to the fresh water produced, the mass flux equation between two phases is presented:

$$\dot{m}_{ew} = \frac{q_{ew} \times A_W \times t}{L} \quad (3.14)$$

Hence

$$\dot{q}_{ew} = h_{ew}(T_w - T_g) \quad (3.15)$$

$$\dot{q}_{cw} = h_{cw}(T_w - T_g) \quad (3.16)$$

Where h_{ew} is the evaporative heat transfer coefficient and h_{cw} is the convective heat transfer coefficient that each depends on the operating range temperature, physical properties of the fluid within the system and the geometry of the evaporative surface and the geometry of the condensing cover respectively.

The convective heat transfer coefficient h_{cw} is given by the dimensionless Nusselt number, which is the ratio of convective to conductive heat transfer across a boundary.

$$Nu = \frac{h_{cw}}{k_v} \times L_v = C(G_r \cdot P_r)^n \quad (3.17)$$

Where

$$h_{cw} = \frac{k_v}{L_v} \times C(G_r \cdot P_r)^n \quad (3.18)$$

Where Gr and Pr are the Grashof and Prandtl numbers respectively and are given by the expressions:

$$G_r = \frac{\beta g L_v^3 \rho^2 \Delta T}{\mu^2} \tag{3.19}$$

$$P_r = \frac{\mu \cdot C_p}{k_v} \tag{3.20}$$

3.5 PHYSICAL MODEL

3.5.1 Experimental Set Up

With one full-TSS model and two half-TSS models, three experiments were conducted in the same location as presented in figure (3.3) in Suez, Egypt (29.966° N, 32.549° E) with the same weather conditions to study how to obtain the maximum productivity during the day. The first experiment took place in 2014, May 14th with the full tube model of TSS and different diameters 200mm, 300mm and 400mm. In 2015, June 2nd another experiment was conducted with half-TSS with the constant tray dimensions 1200mm, 150mm and 30mm. Figure (3.4) shows the experimental set up of the full TSS. Figure (3.5) displays the second experiment model which was designed as half-tubular still with different Radii 100mm, 150mm and 200mm and constant tray dimensions 1200, 150, 30mm. The last experiment model which was designed as the second model in radii but with variable tray dimensions in the tray widths

of 200, 300 and 400mm as shown in figure (3.6). All models consist of basin liner which absorbs incident solar radiations that are transmitted through the tubular glass cover. Basin liner is made of a galvanized steel sheet of 1mm thickness and coated with black paint for better solar absorption. It has an area of 1.2m × 0.15m.

Fig. 3.3 Suez location coordinates [54]

No heat losses occurred from the bottom and side walls of solar still as it is all enclosed into the tubular solar still. The condensing cover of solar still is made of highly transparent plastic of 3mm thickness and is placed on vertical walls of the distillate channel of the solar still. The condensed water gets collected in a distillate channel. A plastic pipe is connected to the distillate channel to drain distillate water to a scaled measuring jar and a drainage pipe is connected to remove wastes inside the solar still. Rubber gaskets are provided between glass cover and vertical walls to prevent heat loss. Thermocouples shown in the schematic figure (3.5) are fixed into the solar still to measure the basin liner, as well as glass and

water temperatures. The thermocouple fixed outside the basin measures the outside temperature of the basin. These thermocouples are connected to digital temperature indicators to indicate the hourly temperature readings. Figure (3.7) illustrates the fixed and the variable dimensions trays.

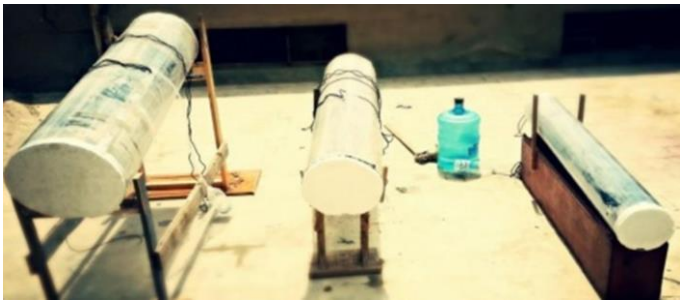

Fig. 3.4 Experimental set-up of the full-TSS model with constant tray dimensions

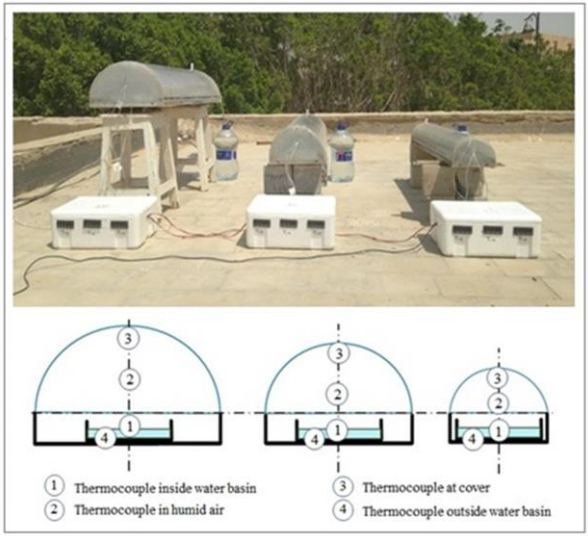

Fig. 3.5 Experimental set-up of the half-TSS model with constant tray dimensions and thermocouples positions

Fig. 3.6 Experimental set-up of the half-TSS model with variable tray dimensions

Fig. 3.7 Constant and variable dimensions trays

Table 3.1 Dimensions of three TSS models

Model N°	Fixed Tray Dimensions (mm)		Variable Tray Dimensions (mm)		Glass Dimensions (mm)	
	Length	1200	Length	1200	Length	1200
1	Height	30	Height	30		
	Width	200	Width	200	Radius	100
	Length	1200	Length	1200	Length	1200
2	Height	30	Height	30		
	Width	200	Width	300	Radius	150
	Length	1200	Length	1200	Length	1200
3	Height	30	Height	30		
	Width	200	Width	400	Radius	200

3.5.2 Measurement Instruments

3.5.2.1 Temperature sensor specifications (Thermocouples)

Manufactured by: LAE Controllers (Figure 3.8)

Model: thermocouple MTR-11

Well Length: 150cm

Temperature Range: -50~150 ℃

Accuracy: +/- 1°C

Operating Humidity: 50~85% RH

Fig. 3.8 Thermocouple and Digital indicator

3.5.2.2 Temperature Recorder (measures ambient temperature)

Measurement: Temperature (°C & °F)

Data Output 446580: Analog 10mvDC per °C/F or %RH

Measurement rate: 2.5 readings per second

Operating Temperature: 32 to 122 °F (0 to 50 °C)

Operating Humidity: < 80% RH

Storage Temperature: 14 to 140 °F (-10 to 60 °C)

Storage Humidity: < 70% RH

Accuracy: (±0.8 °C)

Fig. 3.9 Ambient temperature recorder

3.5.2.3 Solar Intensity Recorder

Manufactured by: HAENNI. Co. (Figures 3.10 and 3.11)

Model: solar 118

Wire Length: 400cm

Radiation Range: 0-1500 W/m^2

Fig. 3.10 HAENNI solar radiation

Fig. 3.11 Sensors of solar radiation

3.5.2.4 Anemometer (measures wind speed)

Figure 3.12 manifests a waterproof anemometer for measuring wind speed. Indication of wind chill temperature based on the combination of air temperature and wind speed. Indication of mean and maximum speeds. Wind curves on the Beaufort scale.

Wind speed: 0,2 … 30 m/s
Accuracy: ±5% of mean wind speed
Units: km/h, m/h, m/s or knots
Temperature: -30° to +59°C
Battery: 3.0 V (CR2032)
Dimensions: 137 × 50 × 18mm³

Fig. 3.12 Anemometer

3.5.3 Weather Conditions and Measurements

A daily measurements on the weather conditions for solar intensity, ambient temperature and wind speed were taken in May from 1-8, 2015 during the TSS experimental setup to study the best weather conditions and their impact on the daily productivity. Figure (3.13) shows a comparison between the hourly ambient temperature and solar intensity on the 2nd of May, 2015 from 6 am to 8 pm.

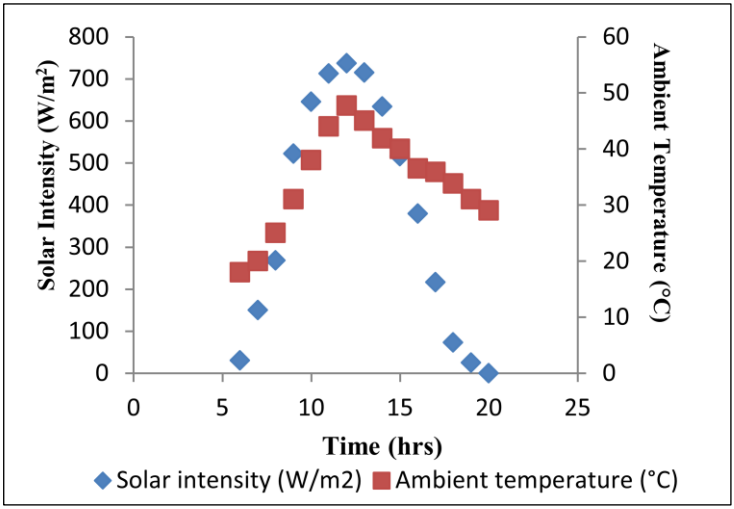

Fig. 3.13 Comparison between the ambient temperature vs. the solar intensity

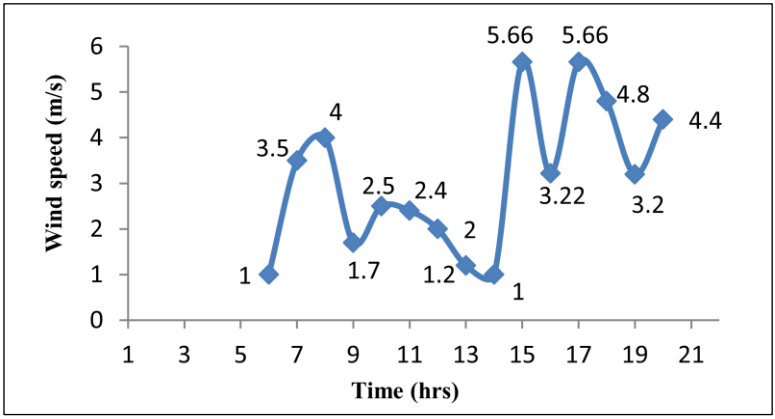

Fig. 3.14 Wind Speed

Figure (3.14) shows the wind speed during the same day. The line chart shows a fluctuation of a wind speed as a main trend starts with 1 m/s of wind speed at the beginning of the day and end with 4.4 m/s at 8 pm. The maximum wind speed of that day was at 3 pm and 5 pm with 5.66 m/s. Figures (3.15), (3.16), (3.17) reveal the hourly temperature readings from basin, vapor and glass for the three models 100mm, 150mm, 200mm respectively.

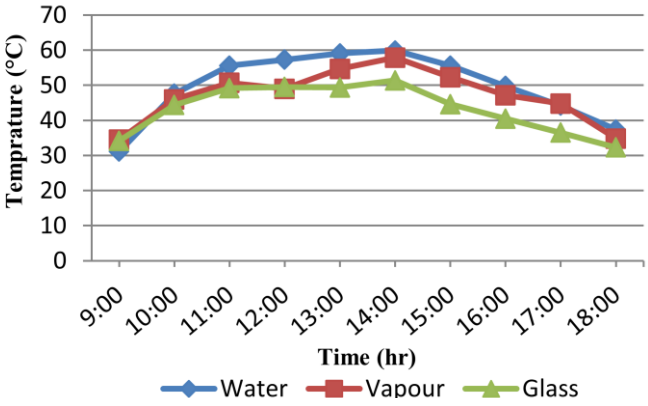

Fig 3.15 Temperature variation for 100mm radius model

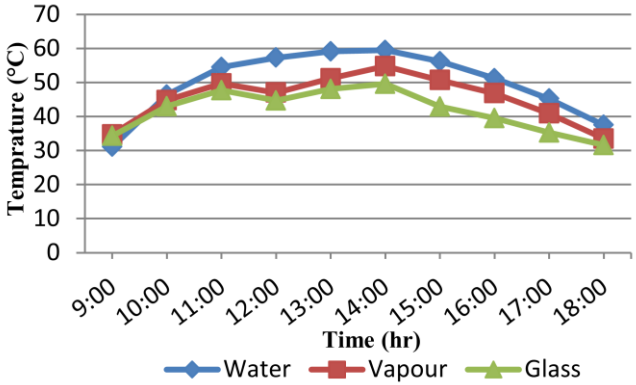

Fig 3.16 Temperature variation for 150mm radius model radius

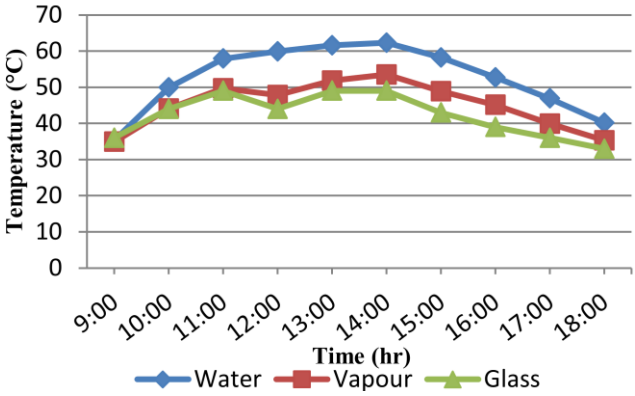

Fig 3.17 Temperature variation for 200mm radius model

3.5.4 Methodology

3.5.4.1 Geometry Details

After the geometry of the Tubular Solar Still (TSS) was created and imported to ANSYS meshing module, a mesh created and saved in ANSYS working directory (.msh). Geometry of three different radii models (100, 150 and 200mm) radii are shown respectively in the figures below:

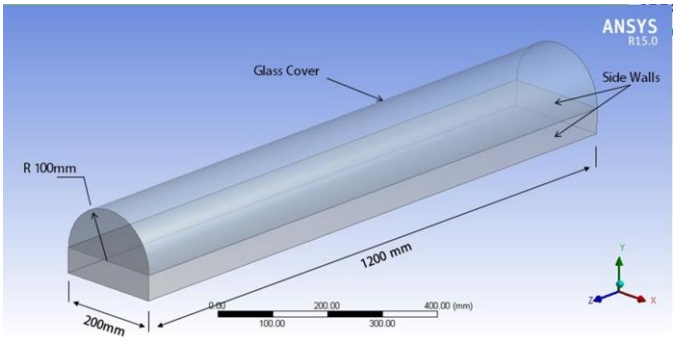

Fig. 3.18 3-D model of 100mm condensing cover radius

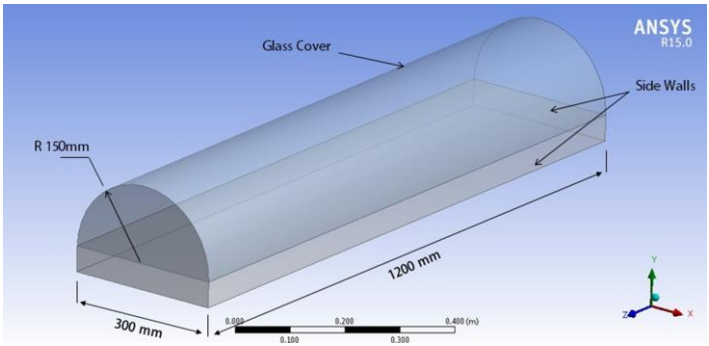

Fig. 3.19 3-D model of 150mm condensing cover radius

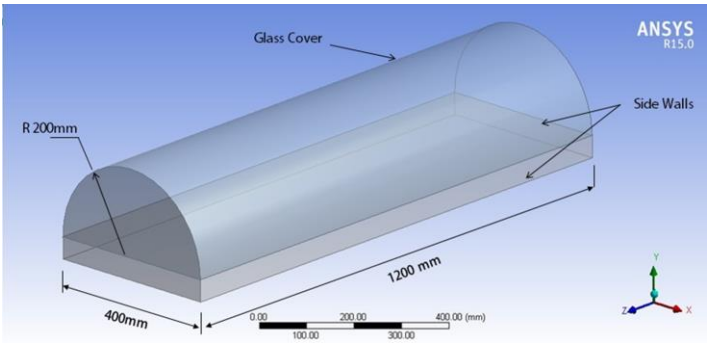

Fig. 3.20 3-D model of 200mm condensing cover radius

3.5.4.2 Meshing Details

The next step after creating the geometry is to import it into the mesh module. Fine sizing is created with an unstructured mesh of the tetrahedrons method. Figures (3.21), (3.22), (3.23) below reveal the meshing details of radii models 100, 150 and 200mm respectively.

Table 3.2 Mesh Statistics

Domain	Nodes	Elements
100 mm Radius	9275	40966
150 mm Radius	14378	66518
200 mm Radius	18951	89578

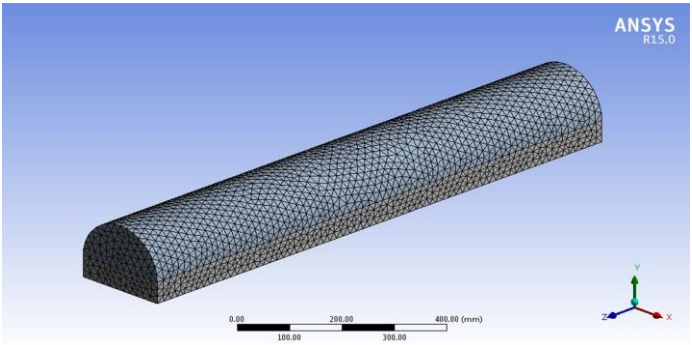

Fig. 3.21 3-D unstructured mesh of 100mm condensing cover radius

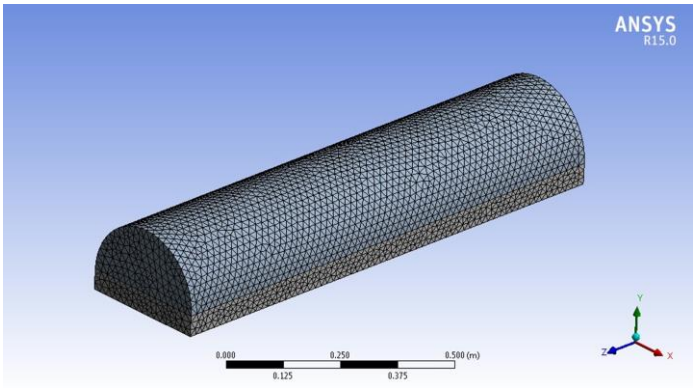

Fig. 3.22 3-D unstructured mesh of 150mm condensing cover radius

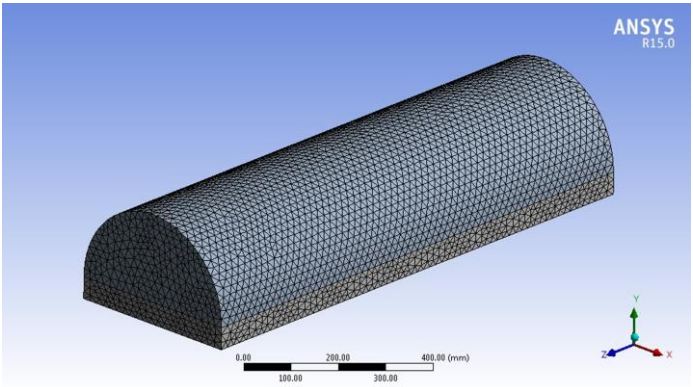

Fig. 3.23 3-D Unstructured mesh of 200mm condensing cover radius

3.5.4.3 Pre-processing Details

The next step after finishing the mesh module is the Pre-processing where the boundary conditions must be assigned for every detail of the mesh to solve energy, continuity and momentum equation. In the CFX Pre two domains are assigned for the water tray and for the glass cover, where two phase domains are created for each of them in the VOF framework for water and mixture of water vapor ideal air. Both phases are continuous with taking into account the buoyancy effect when accounting for thermal energy and heat transfer. Two resistance model are taken to transfer heat, heat transfer coefficient for water phase and zero resistance for gas phase. All sidewalls were assumed to be adiabatic so that no heat loss takes place. It was assumed that heat gets into the model from the bottom to heat up the water until it evaporates. Adhesion forces for the drop formation are taken into account. Free slip boundary condition is specified for Vapor phase and no slip boundary condition is specified for liquid phase.

3.5.4.4 Solving

The solver solves the mass, momentum and energy equations throughout the domain together with the specified physical model. The equations are discretized along the cells of the domain and solved until convergence is reached. ANSYS CFX was used as a solver and for the calculations. Figure 3.24 illustrates the convergence of the CFX-solver.

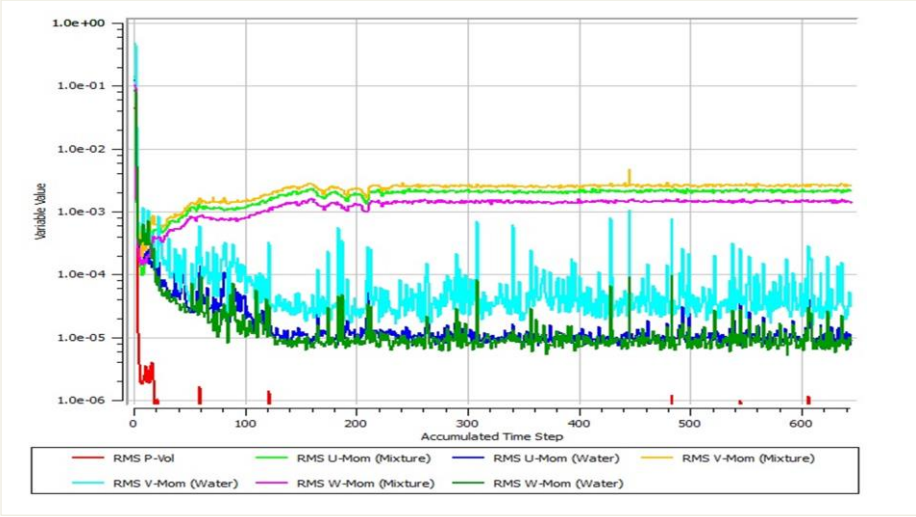

Fig. 3.24 Convergence graph of the fluid flow simulation

3.5.4.5 CFX Post

The result from the solving is then post-processed. This is where the results are visualized by plotting interesting parameters in different ways. Post-processing was performed in ANSYS CFX. Plots and result contours are shown in chapter 4.

`

CHAPTER 4

RESULT AND DISCUSSION

4. RESULT AND DISCUSSION

In order to evaluate the results, important parameters like the temperature distribution, velocity distribution and fluid volume fraction were plotted in different points. Comparisons have also been made by comparing the plots from numerical simulations to the rig-test results taken under normal environmental conditions. It is clear that, the behavior of the solar still depends on many factors such as water depth, water temperature, the glass cover thickness and fabrication materials. An adaption of computational fluid dynamics (CFD) is considered to compare between the performance of three different diameter models to analyze the rate of evaporation for each model. The CFD CFX 15.0 is used for the numerical analysis.

4.1 Temperature Distribution

Due to the heat supply from the basin bottom, the water starts to warm up to the vapor limit. Temperature difference between the water vapor and the glass cover leads to condensation of the water vapor on the inner surface of the tubular glass cover. A non-uniform temperature distribution is generated in the domain because the temperature source is applied to the tray bottom wall. A line is drawn in the middle of the

model in vertical direction from bottom to top, to show the temperature distribution in the domain from basin to tubular glass cover of the solar still. The following figures show the simulation results from 40-60°C with a gradual rise of 5°C.

4.1.1 Simulation for 200mm radius

4.1.1.1 Gas mixture at a bottom temperature of 40°C

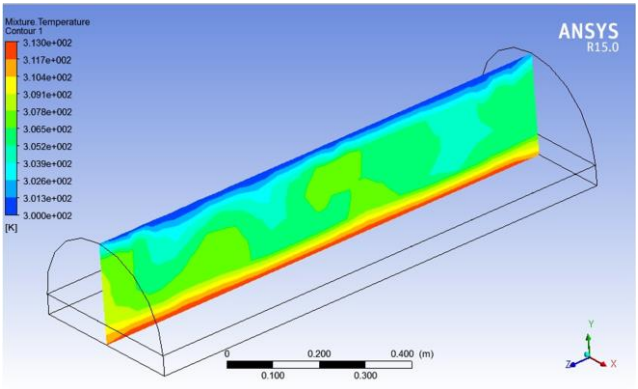

Fig 4.1 Gas mixture temperature contour at a bottom temperature of 40°C for a 200mm radius

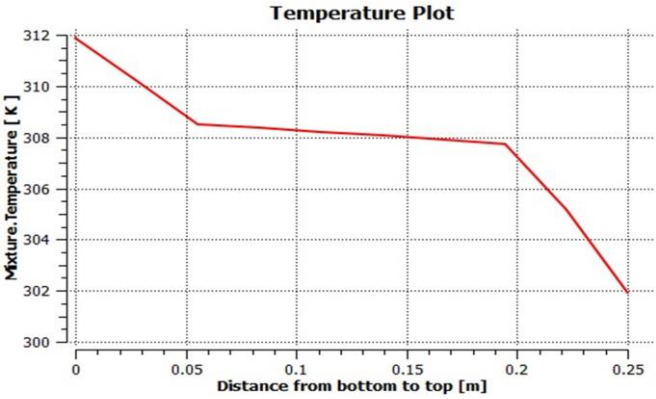

Fig 4.2 Gas mixture temperature plot at a bottom temperature of 40°C for a 200mm radius

4.1.1.2 Water at a bottom temperature of 40°C

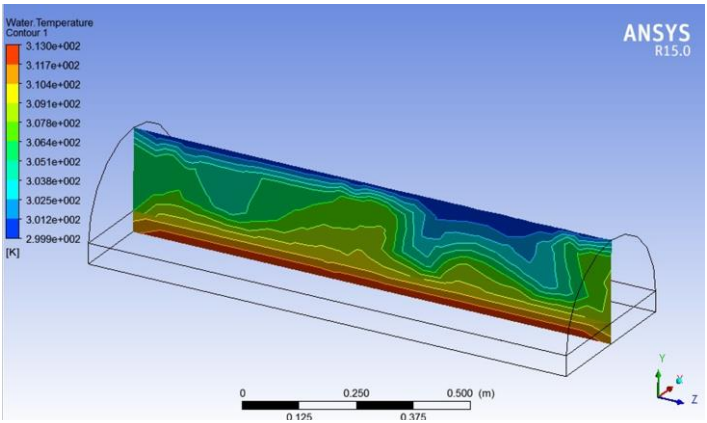

Fig 4.3 Water temperature contour at a bottom temperature of 40°C for a 200mm radius

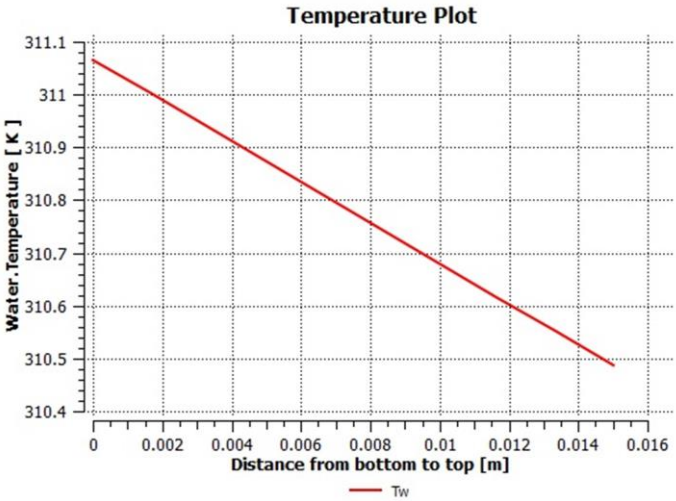

Fig 4.4 Water temperature plot at a bottom temperature of 40°C for a 200mm radius

4.1.1.3 Gas mixture at bottom temperature of 45℃

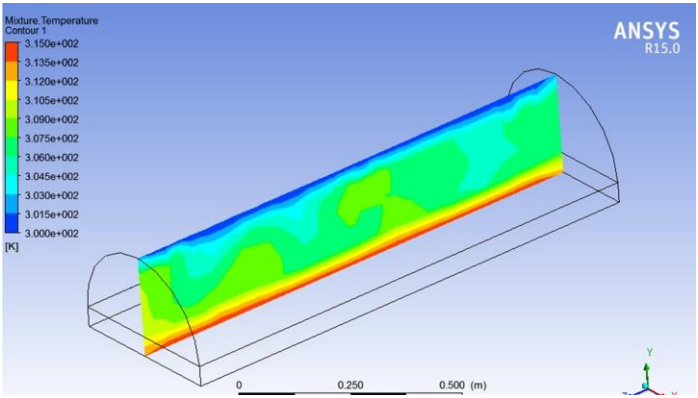

Fig 4.5 Gas mixture temperature contour at a bottom temperature of 45°C for a 200mm radius

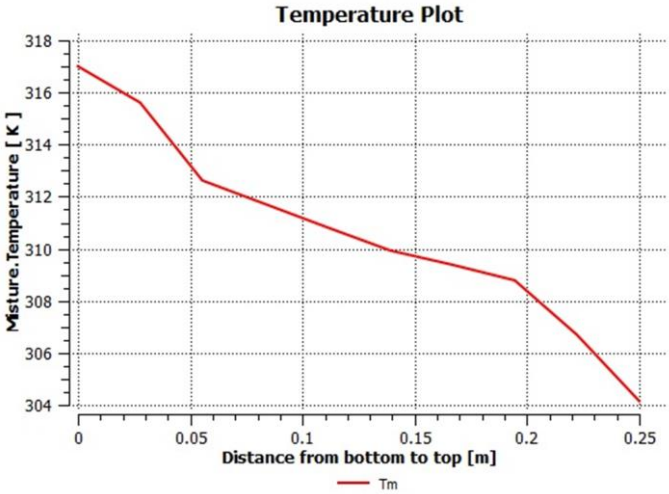

Fig 4.6 Gas mixture temperature plot at a bottom temperature of 45°C for a 200mm radius

4.1.1.4 Water at a bottom temperature of 45°C

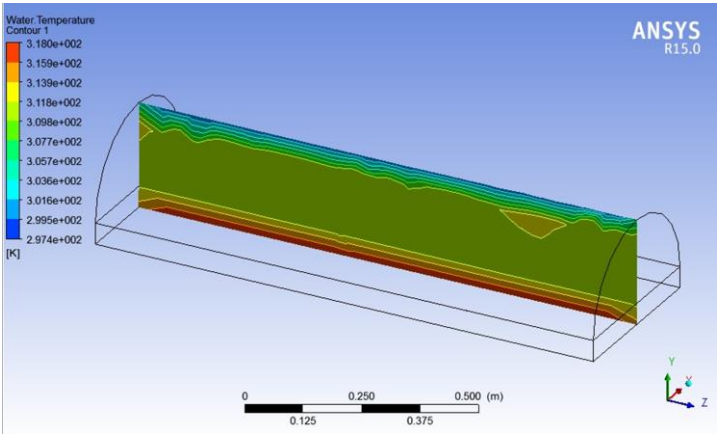

Fig 4.7 Water temperature contour at a bottom temperature of 45°C for a 200mm radius

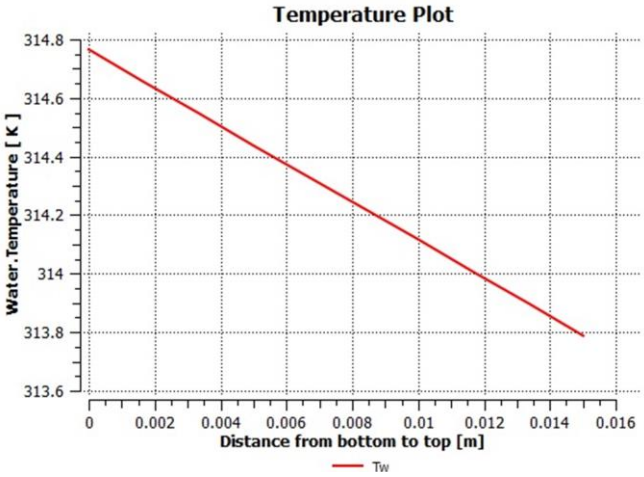

Fig 4.8 Water temperature plot at a bottom temperature of 45°C for a 200mm radius

4.1.1.5 Gas mixture at a bottom temperature of 50°C

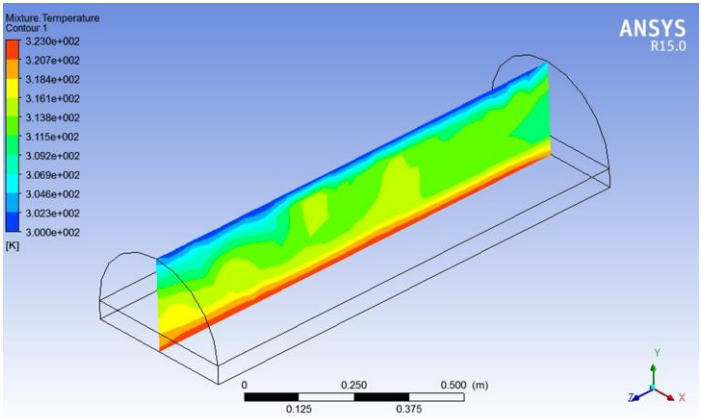

Fig 4.9 Gas mixture temperature contour at a bottom temperature of 50°C for a 200mm radius

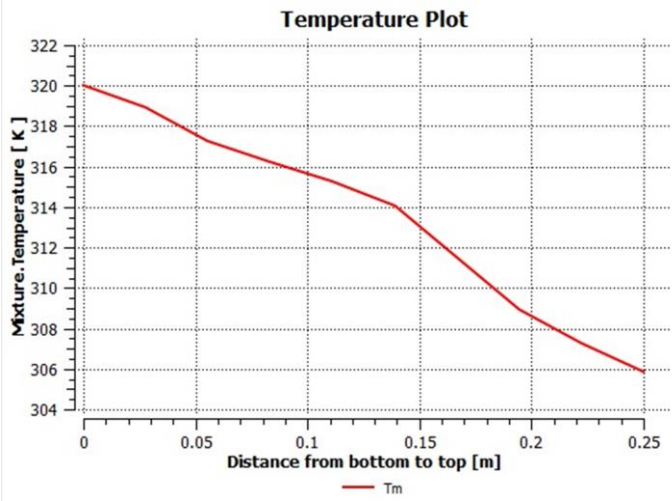

Fig 4.10 Gas mixture temperature plot at a bottom temperature of 50°C for a 200mm radius

4.1.1.6 Water at a bottom temperature of 50°C

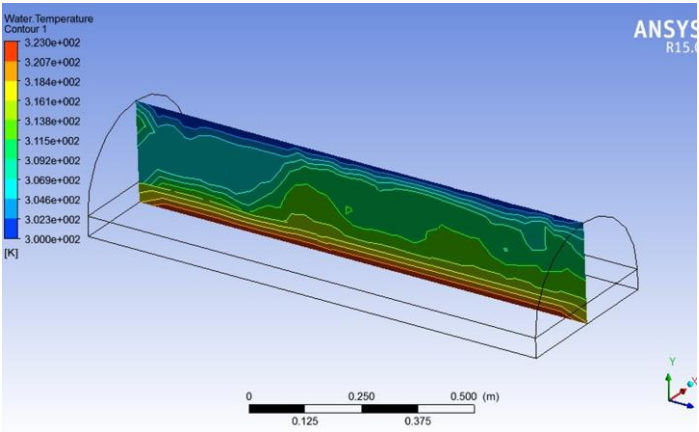

Fig 4.11 Water temperature contour at a bottom temperature of 50°C for a 200mm radius

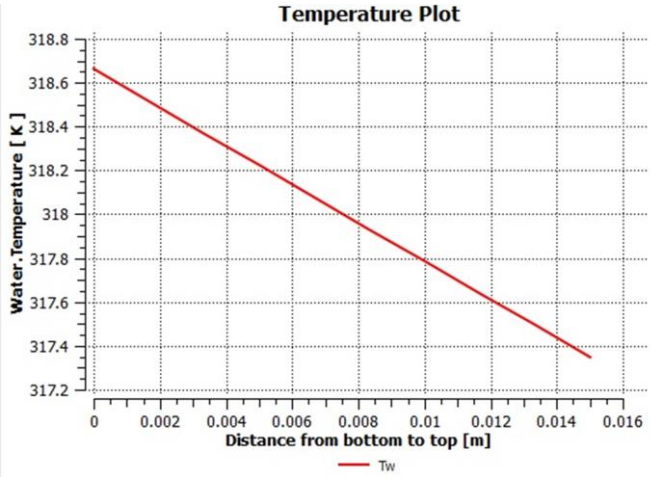

Fig 4.12 Water temperature plot at a bottom temperature of 50°C for a 200mm radius

4.1.1.7 Gas mixture at a bottom temperature of 55°C

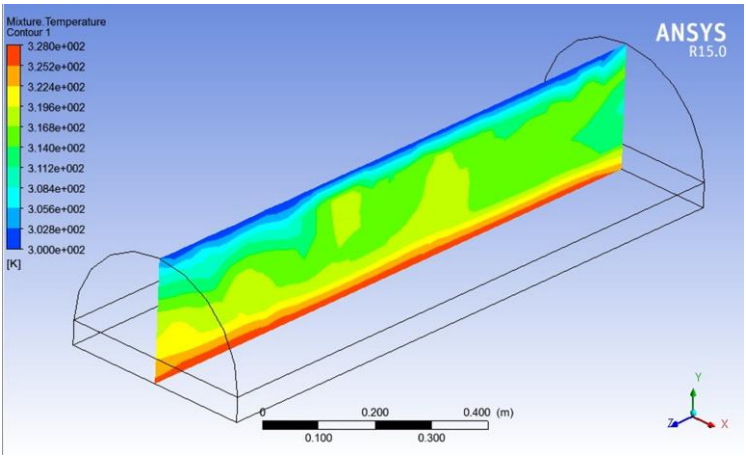

Fig 4.13 Gas mixture temperature contour at a bottom temperature of 55°C For a 200mm radius

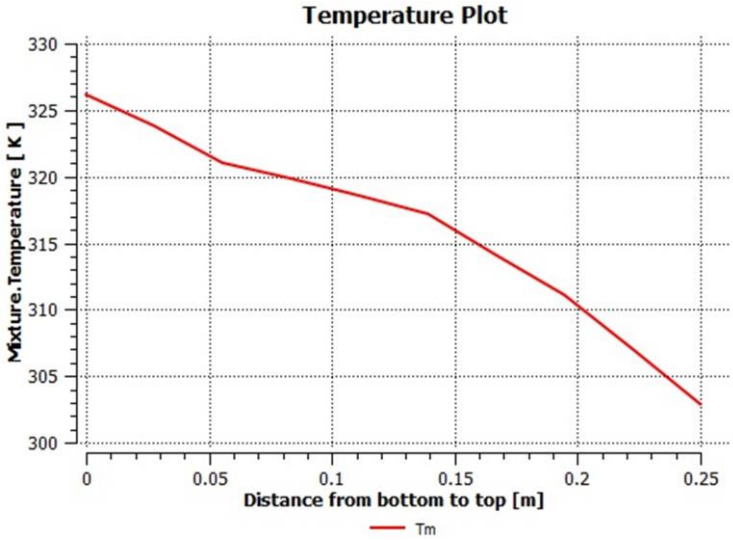

Fig 4.14 Gas mixture temperature plot at a bottom temperature of 55°C

4.1.1.8 Water at a bottom temperature of 55°C

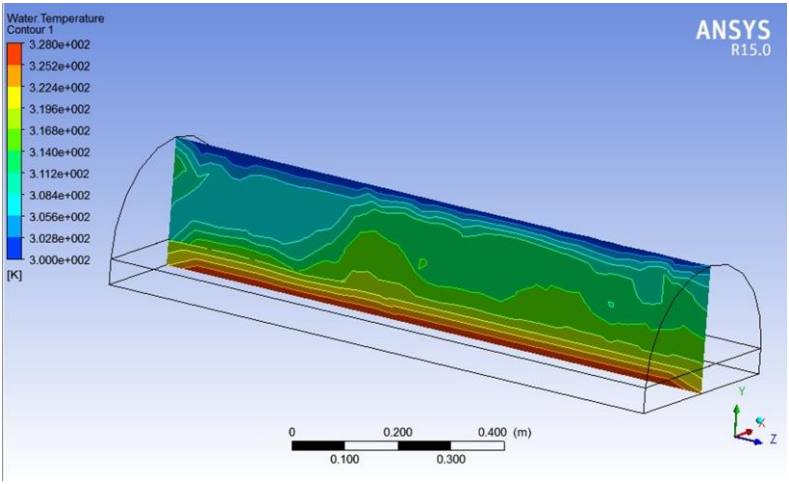

Fig 4.15 Water temperature contour at a bottom temperature of 55°C for a 200mm radius

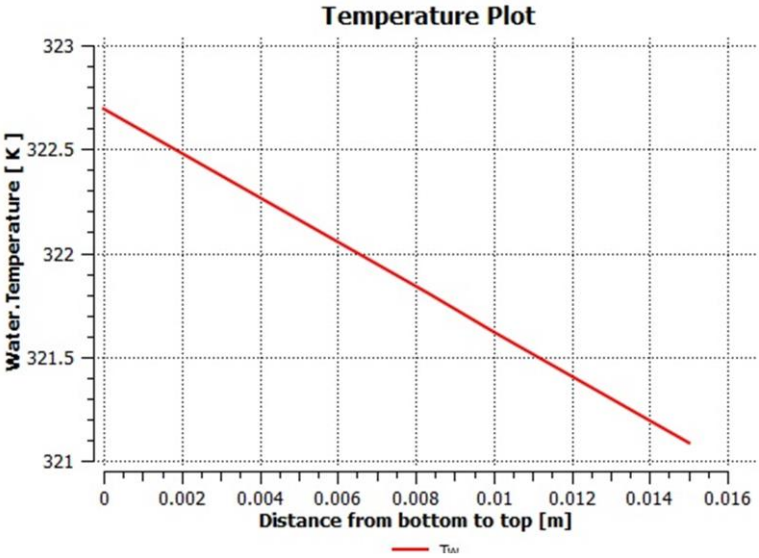

Fig 4.16 Water temperature plot at a bottom temperature of 55°C for a 200mm radius

4.1.1.9 Gas mixture at a bottom temperature of 60°C

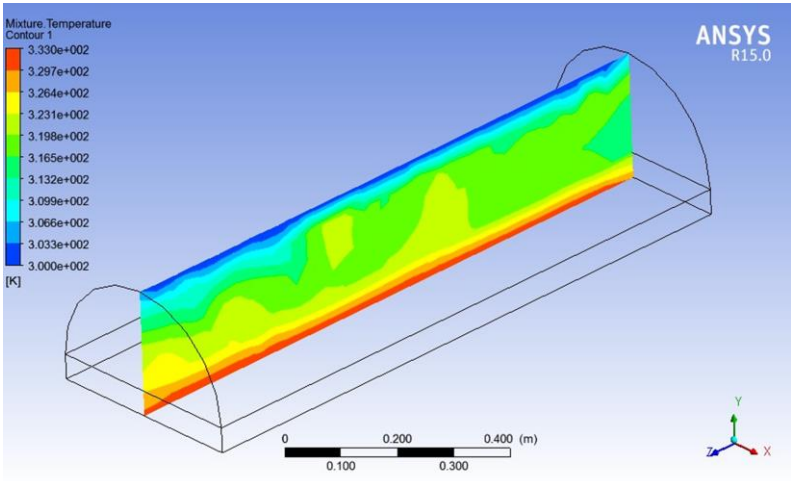

Fig 4.17 Gas mixture temperature contour at a bottom temperature of 60°C for a 200mm radius

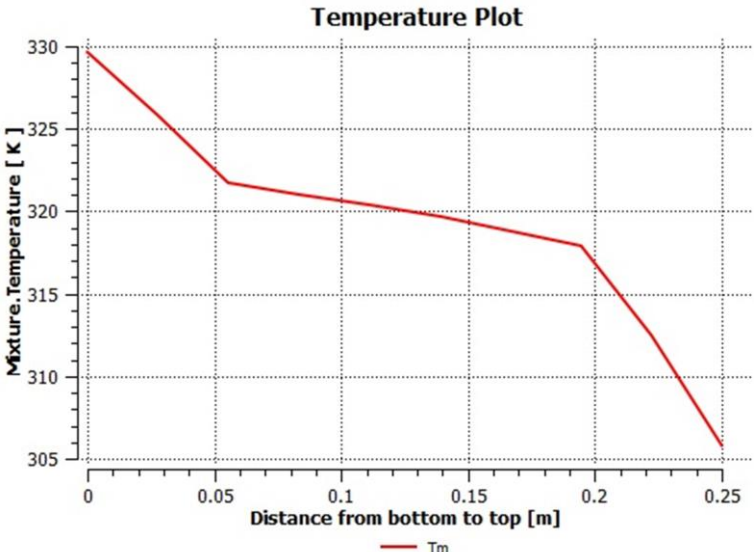

Fig 4.18 Gas mixture temperature plot at a bottom temperature of 60°C for a 200mm radius

4.1.1.10 Water at a bottom temperature of 60°C

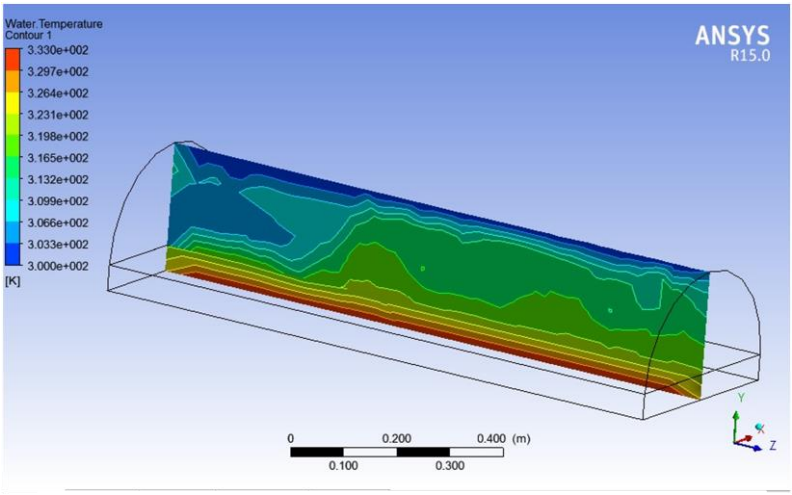

Fig 4.19 Water temperature contour at a bottom temperature of 60°Cfor a 200mm radius

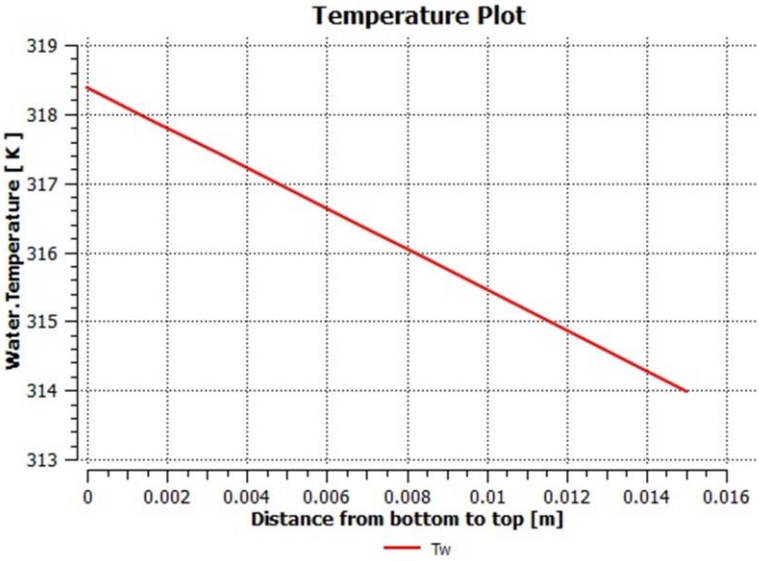

Fig 4.20 Water temperature plot at a bottom temperature of 60°C for a 200mm radius

4.1.2 Simulation for 150 mm radius

4.1.2.1 Gas mixture at a bottom temperature of 40°C

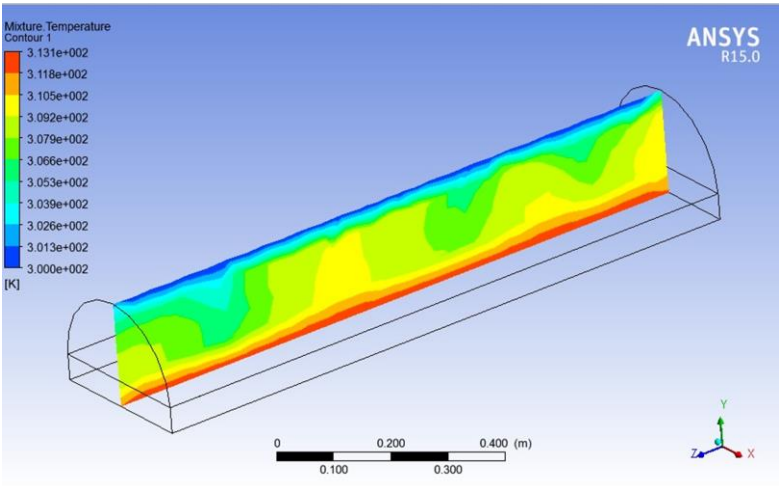

Fig 4.21 Gas mixture temperature contour at a bottom temperature of 40°C for a 150mm radius

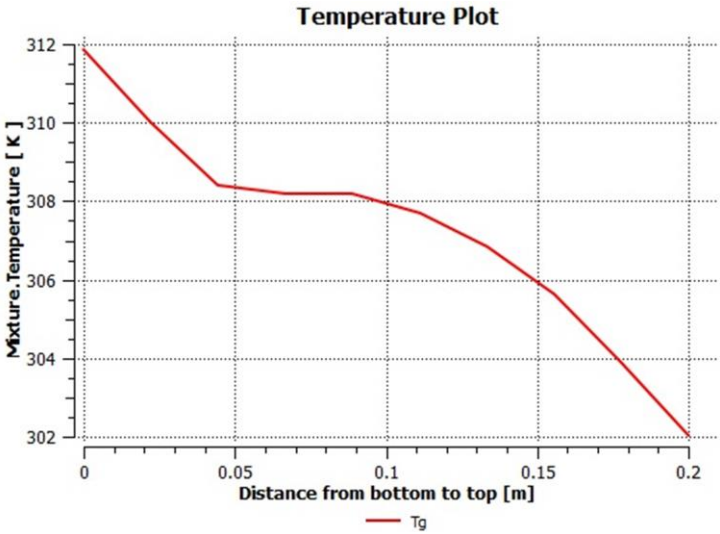

Fig 4.22 Gas mixture temperature plot at a bottom temperature of 40°C for a 150mm radius

4.1.2.2 Water at a bottom temperature of 40°C

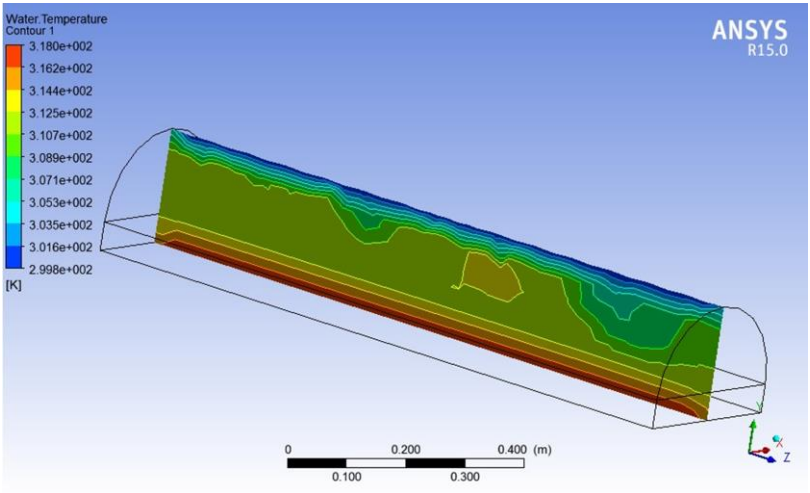

Fig 4.23 Water temperature contour at a bottom temperature of 40°C for a 150mm radius

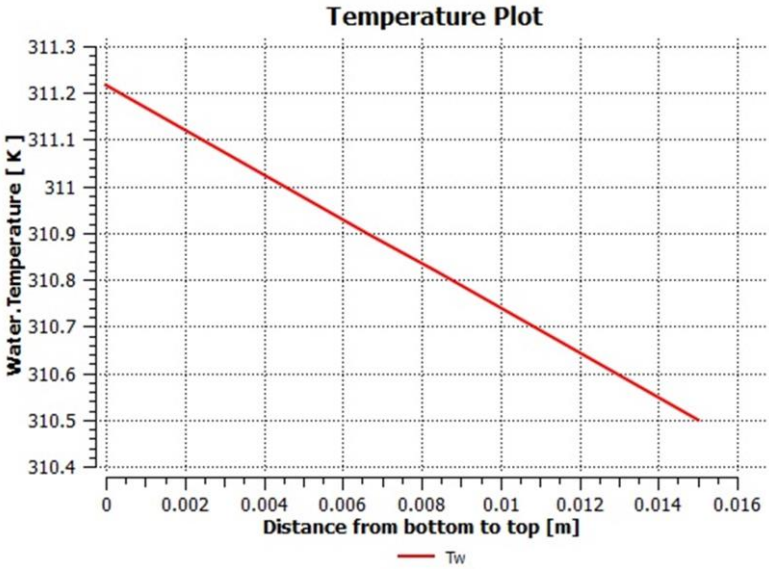

Fig 4.24 Water temperature plot at a bottom temperature of 40°C for a 150mm radius

4.1.2.3 Gas mixture at a bottom temperature of 45°C

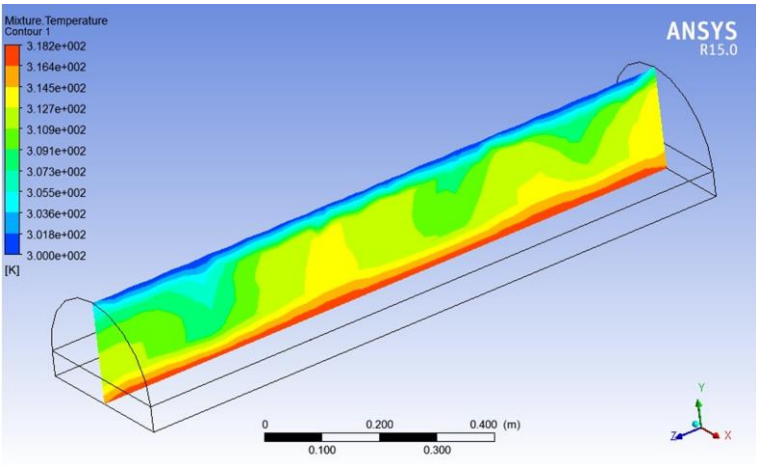

Fig 4.25 Gas mixture temperature contour at a bottom temperature of 45°C for a 150mm radius

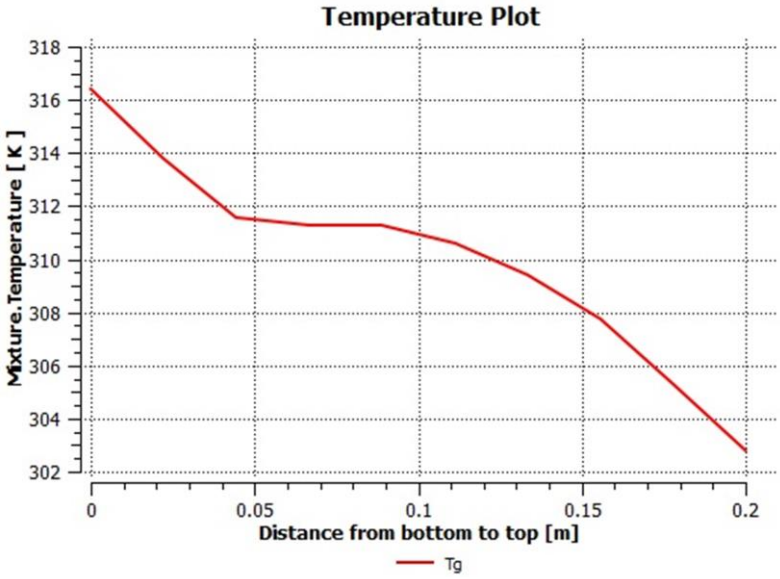

Fig 4.26 Gas mixture temperature plot at a bottom temperature of 45°C for a 150mm radius

4.1.2.4 Water at a bottom temperature for 45°C

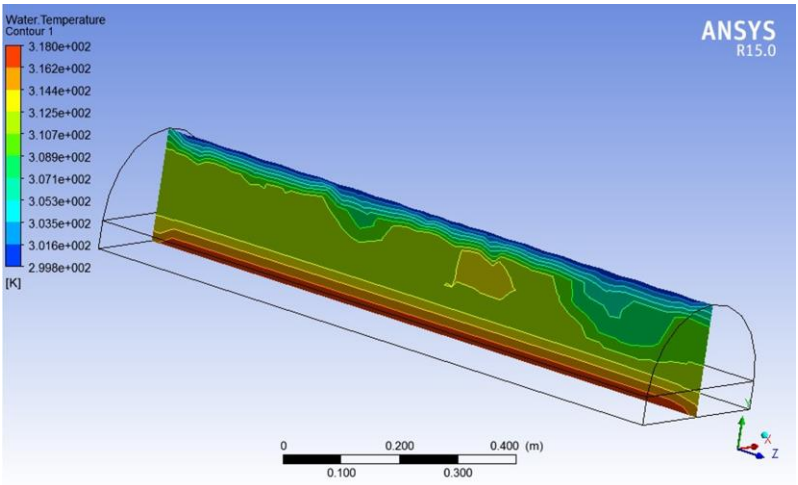

Fig 4.27 Water temperature contour at a bottom temperature of 45°C for a 150mm radius

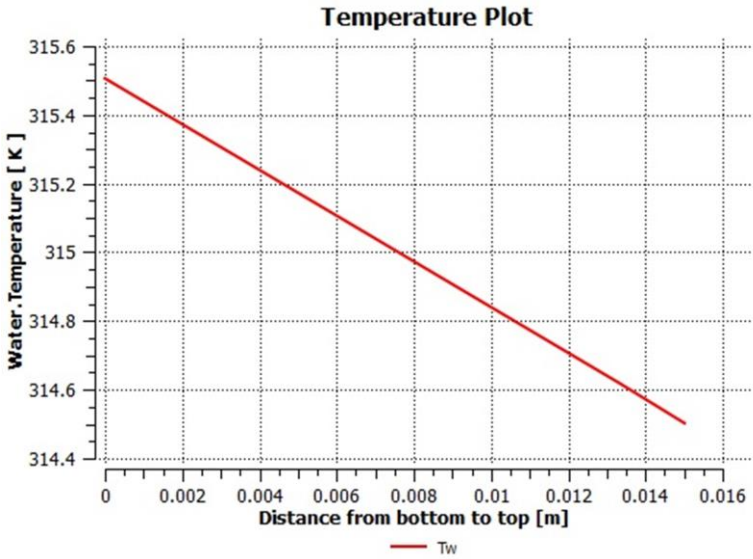

Fig 4.28 Water temperature plot at a bottom temperature of 45°C for a 150mm radius

4.1.2.5 Gas mixture at bottom temperature 50°C

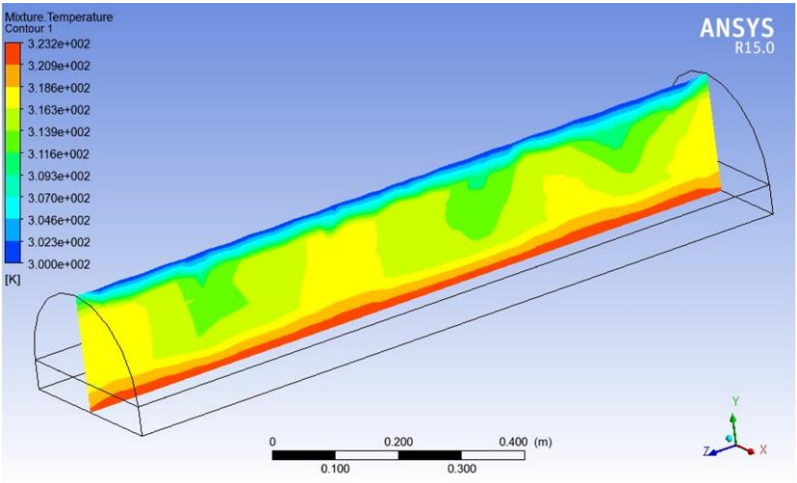

Fig 4.29 Gas mixture temperature contour at a bottom temperature of 50°C for a 150mm radius

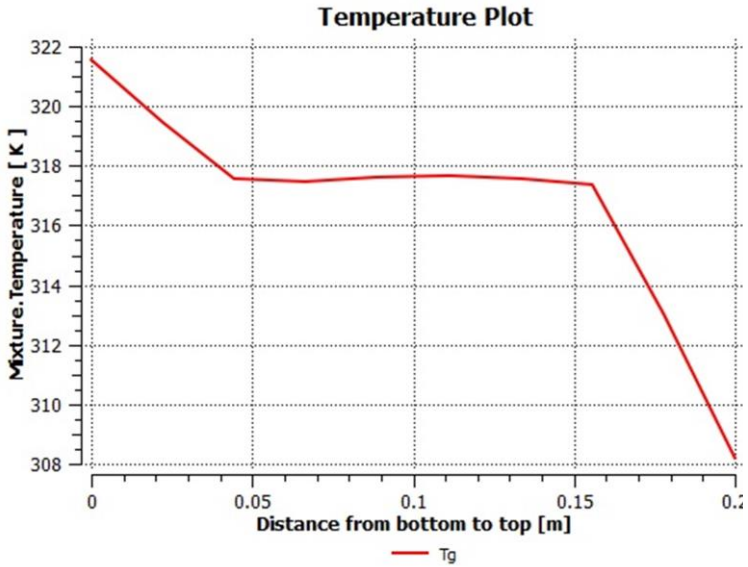

Fig 4.30 Gas mixture temperature plot at a bottom temperature of 50°C for a 150mm radius

4.1.2.6 Water at a bottom temperature of 50°C

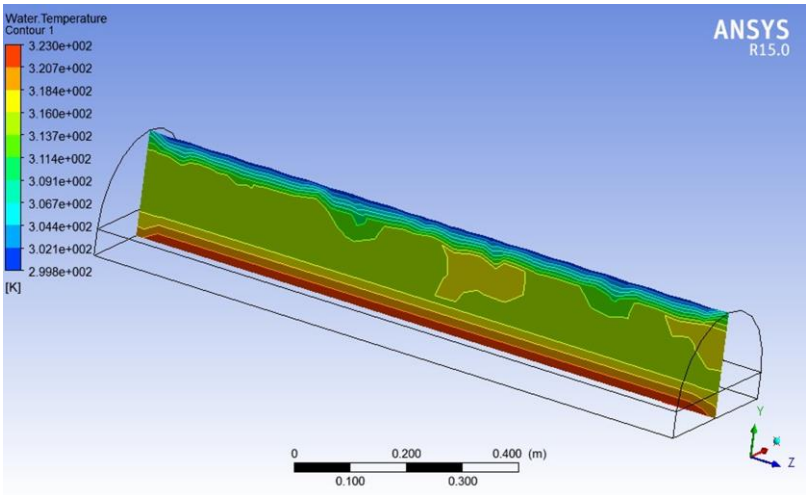

Fig 4.31 Water temperature contour at a bottom temperature of 50°C for a 150mm radius

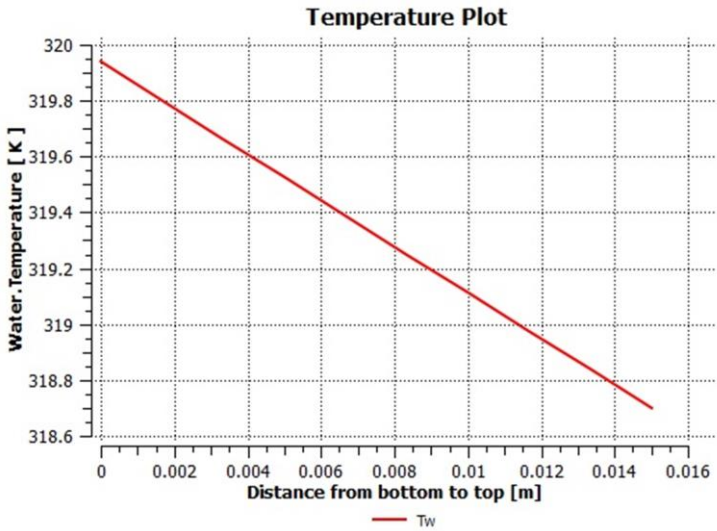

Fig 4.32 Water temperature plot at a bottom temperature of 50°C for a 150mm radius

4.1.2.7 Gas mixture at a bottom temperature of 55°C

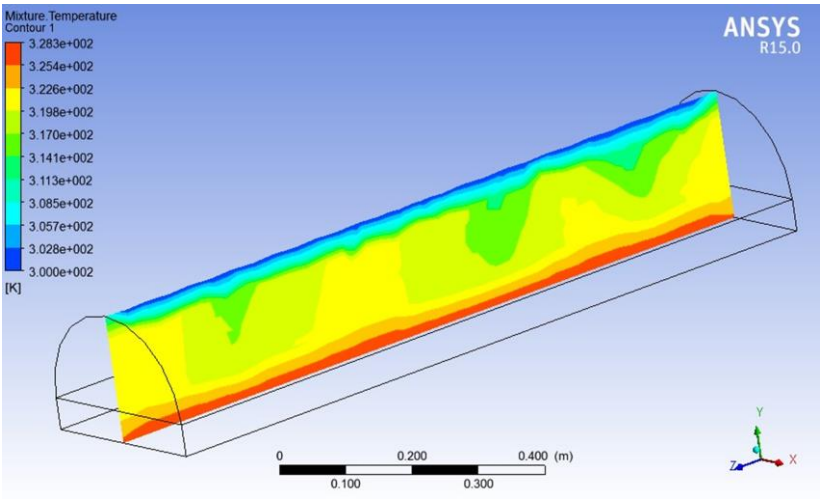

Fig 4.33 Gas mixture temperature contour at a bottom temperature of 55°C for a 150mm radius

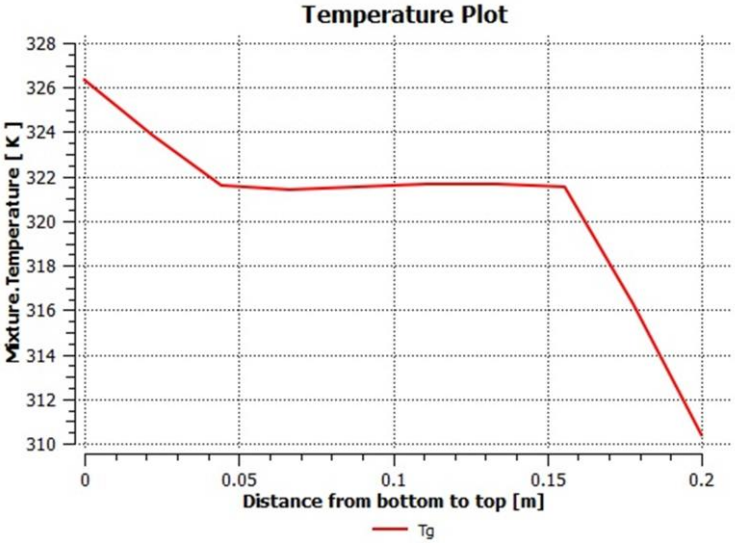

Fig 4.34 Gas mixture temperature plot at a bottom temperature of55°C for a 150mm radius

4.1.2.8 Water at a bottom temperature of 55°C

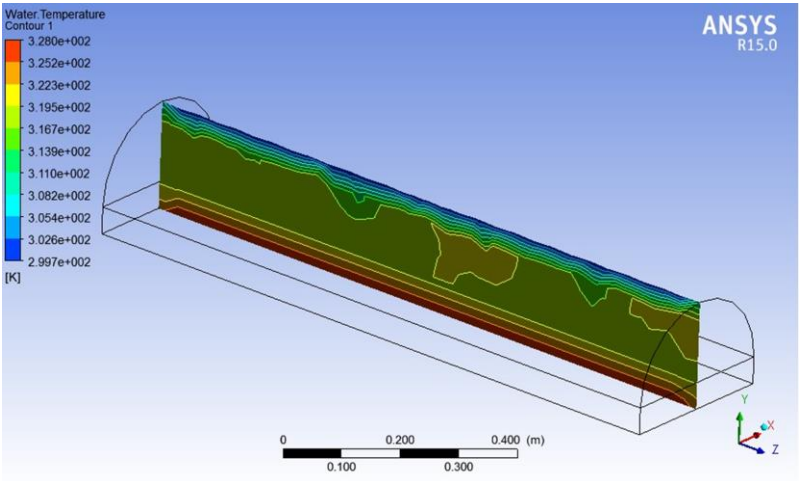

Fig 4.35 Water temperature contour at a bottom temperature of 55°C for a 150mm radius

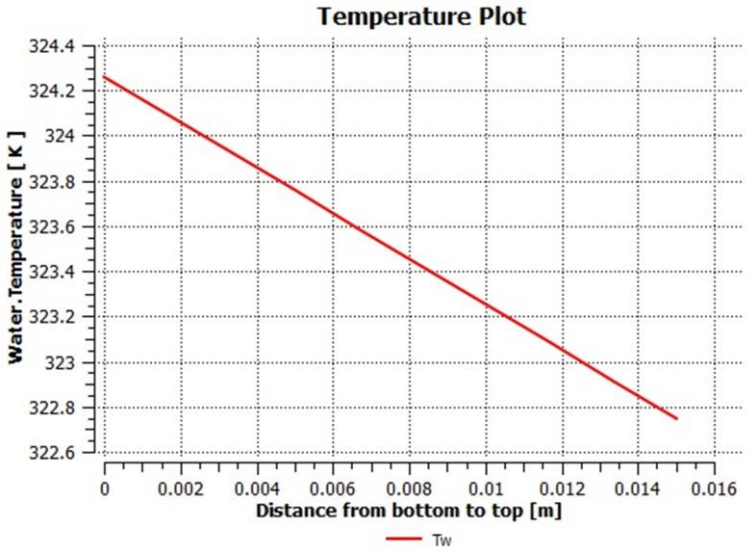

Fig 4.36 Water temperature plot at a bottom temperature of 55°C for a 150mm radius

4.1.2.8 Gas mixture at a bottom temperature of 60°C

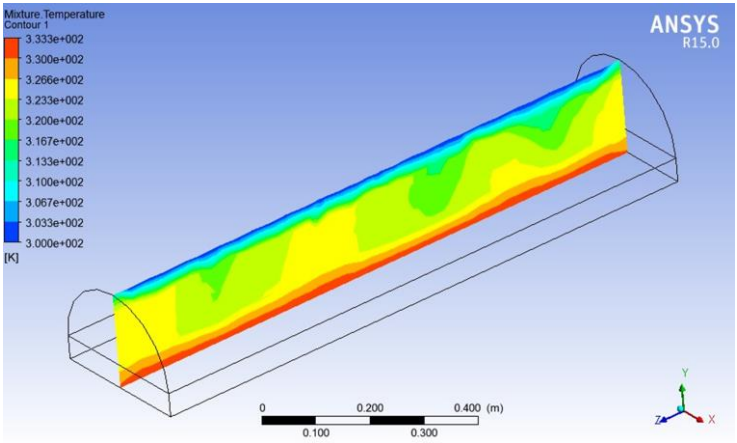

Fig 4.37 Gas mixture temperature contour at a bottom temperature of 60°C for a 150mm radius

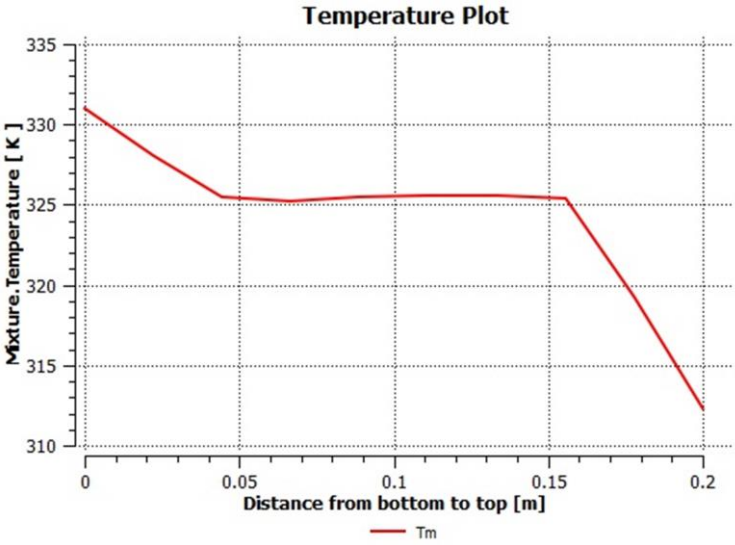

Fig 4.38 Gas mixture temperature plot at a bottom temperature of 60°C for a 150mm radius

4.1.2.9 Water at a bottom temperature of 60°C

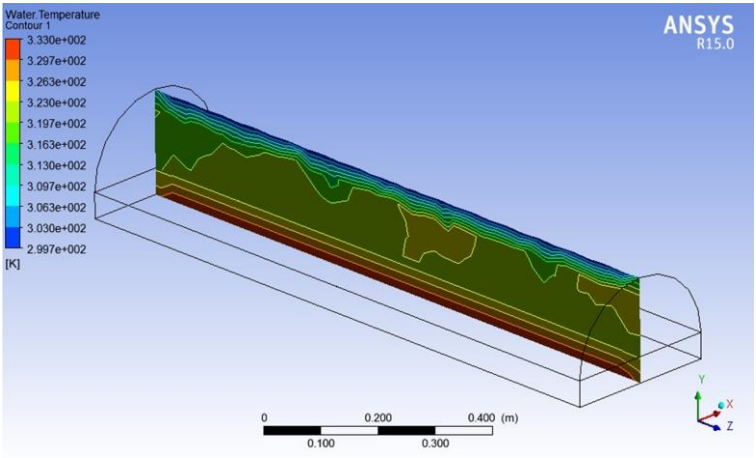

Fig 4.39 Water temperature plot at a bottom temperature of 60°C for a 150mm radius

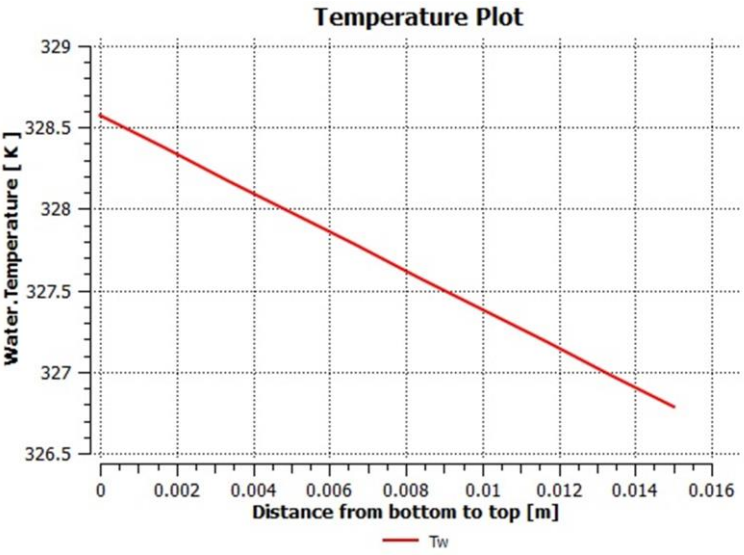

Fig 4.40 Water temperature plot at a bottom temperature of 60°C for a 150mm radius

4.1.3 Simulation for 100mm radius

4.1.3.1 Gas mixture at a bottom temperature of 40°C

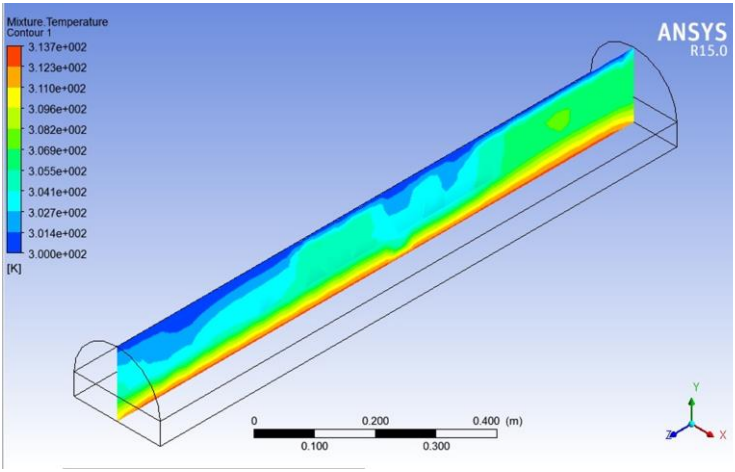

Fig 4.41 Gas mixture temperature contour at a bottom temperature of 40°C for a 100mm radius

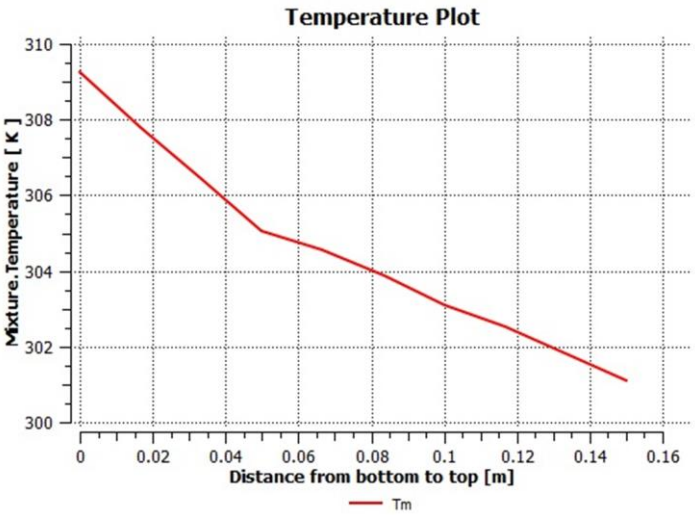

Fig 4.42 Gas mixture temperature plot at a bottom temperature of 40°C for a 100mm radius

4.1.3.2 Water at a bottom temperature of 40°C

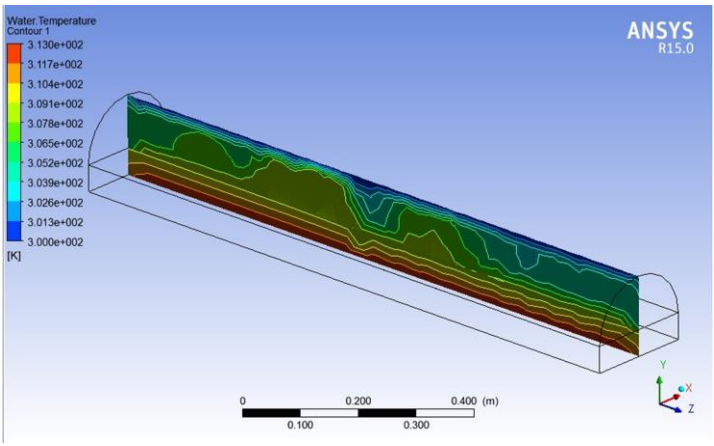

Fig 4.43 Water temperature contour at a bottom temperature of 40°C for a 100mm radius

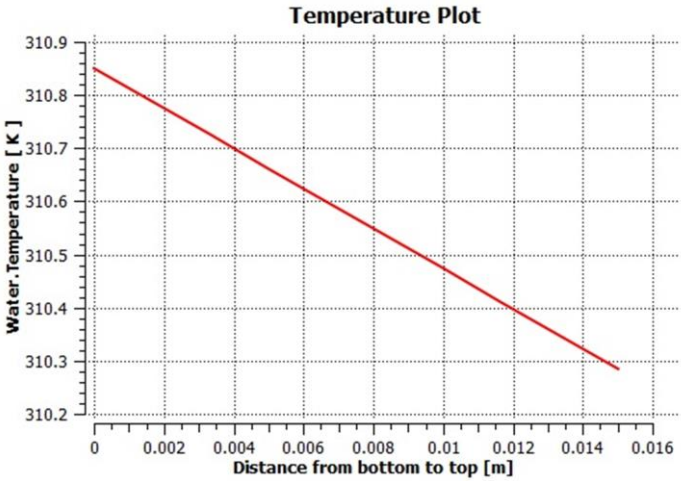

Fig 4.44 Water temperature plot at a bottom temperature of 40°C for a 100mm radius

4.1.3.3 Gas mixture at a bottom temperature of 45°C

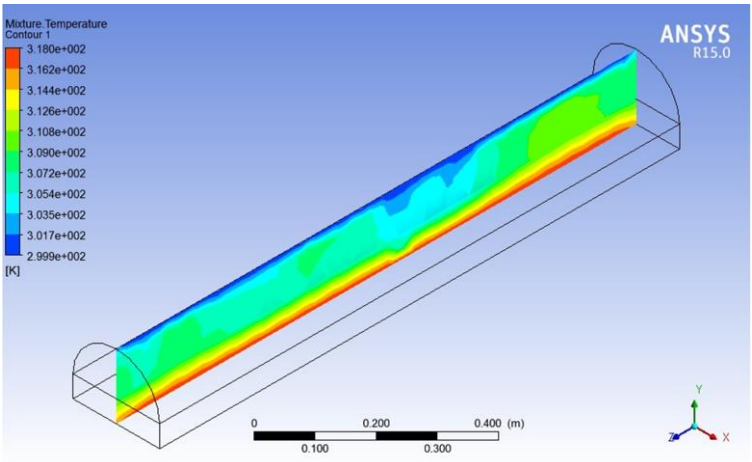

Fig 4.45 Gas mixture temperature contour at a bottom temperature of 45°C for a 100mm radius

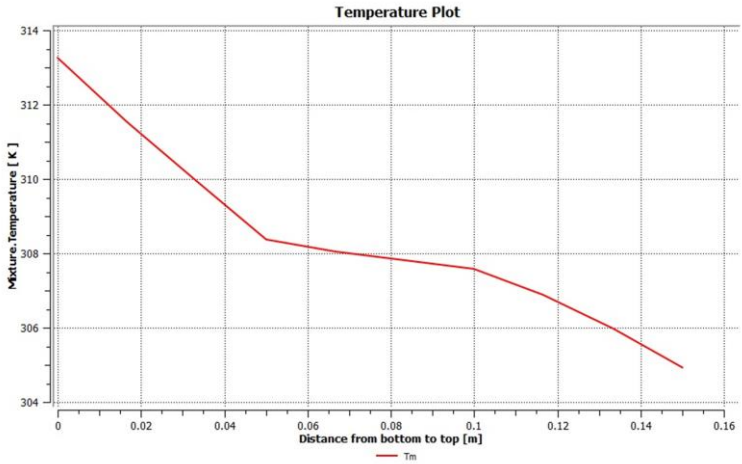

Fig 4.46 Gas mixture temperature plot at a bottom temperature of 45°C for a 100mm radius

4.1.3.4 Water at a bottom temperature of 45°C

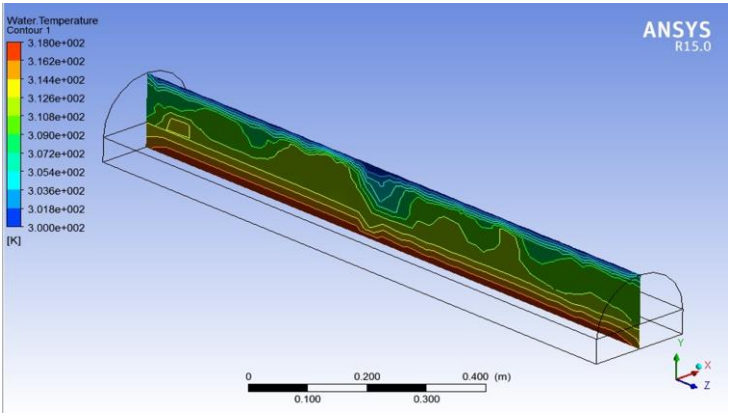

Fig 4.47 Water temperature contour at a bottom temperature of 45°C for a 100mm radius

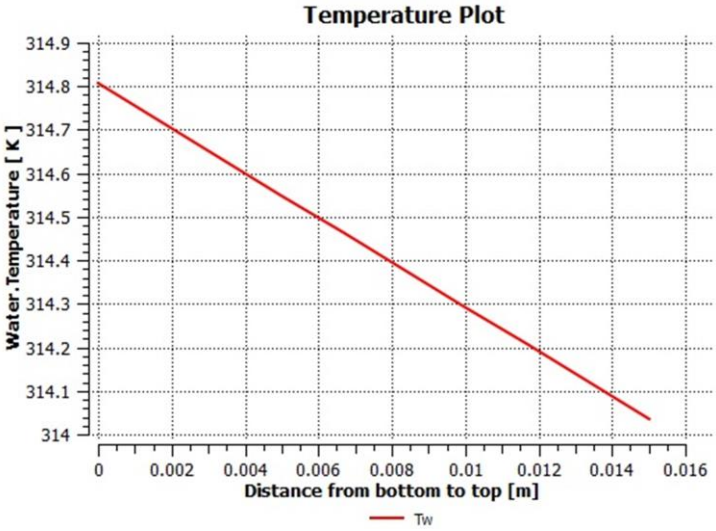

Fig 4.48 Water temperature plot at a bottom temperature of 45°C for a 100mm radius

4.1.3.5 Gas mixture at a bottom temperature of 50°C

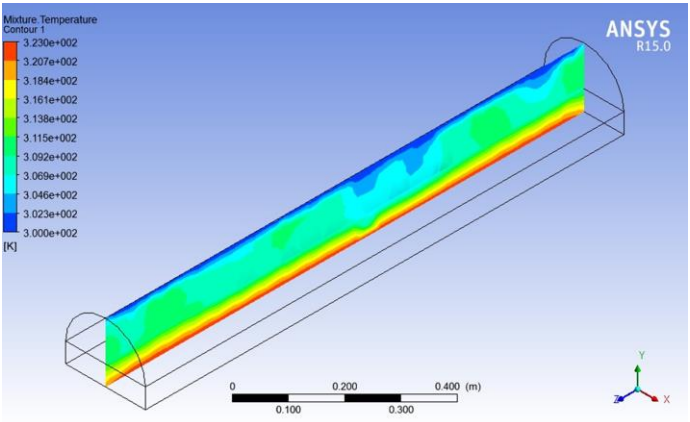

Fig 4.49 Gas mixture temperature contour at a bottom temperature of 50°C for a 100mm radius

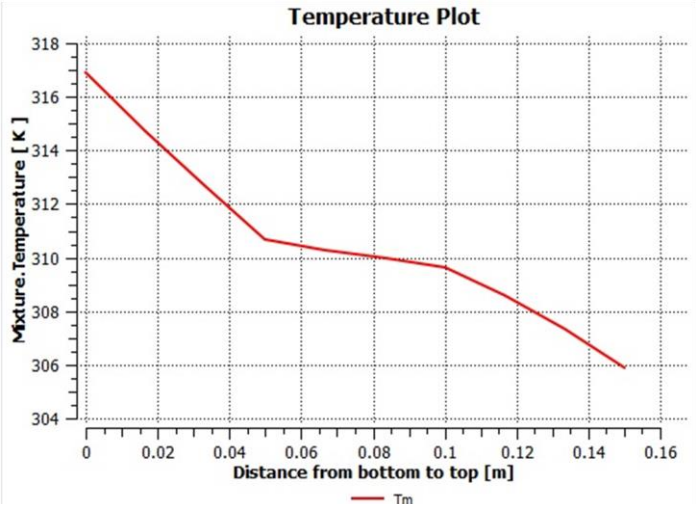

Fig 4.50 Gas mixture temperature plot at a bottom temperature of 50°C

4.1.3.6 Water at a bottom temperature of 50°C

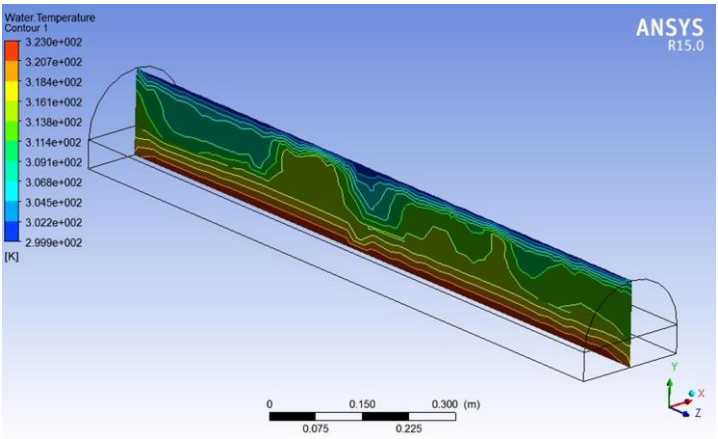

Fig 4.51 Water temperature contour at a bottom temperature of 50°C for a 100mm radius

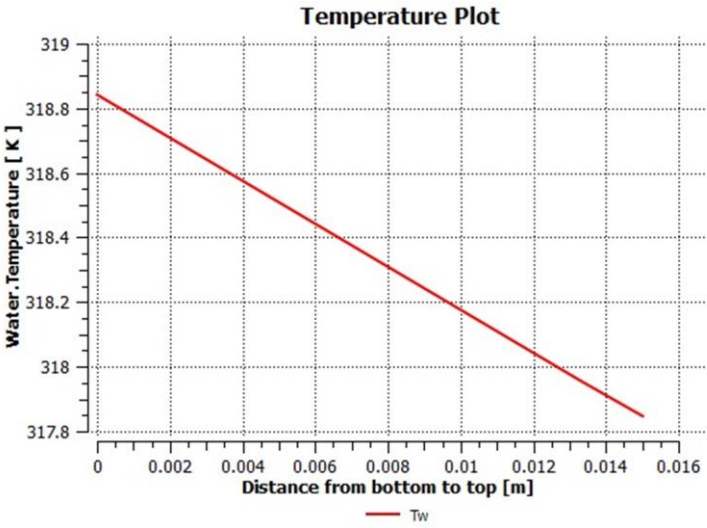

Fig 4.52 Water temperature plot at a bottom temperature of 50°C for a 100mm radius

4.1.3.7 Gas Mixture at a bottom temperature of 55°C

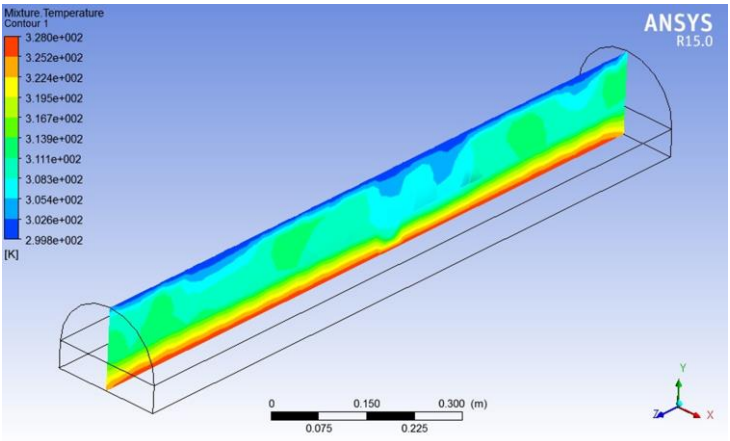

Fig 4.53 Gas mixture temperature contour at a bottom temperature of 55°C for a 100mm radius

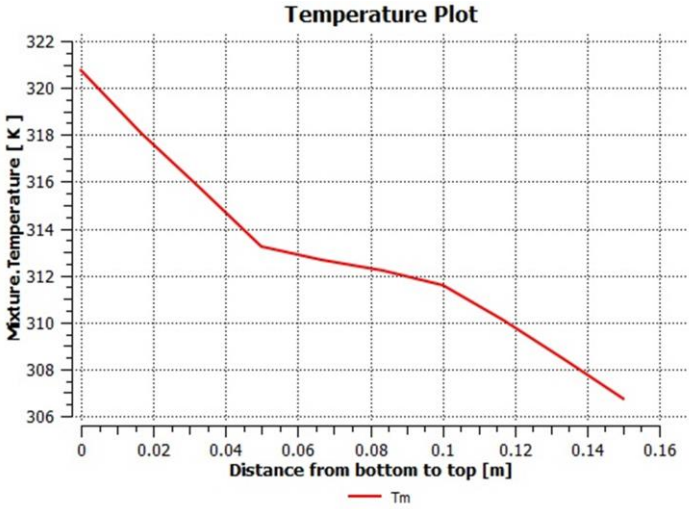

Fig 4.54 Gas mixture temperature plot at a bottom temperature of 55°C for a 100mm radius

4.1.3.8 Water at a bottom temperature of 55°C

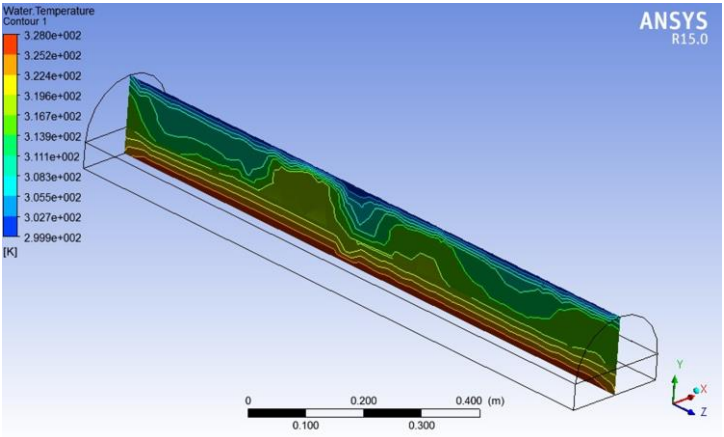

Fig 4.55 Water temperature contour at a bottom temperature of 55°C for a 100mm radius

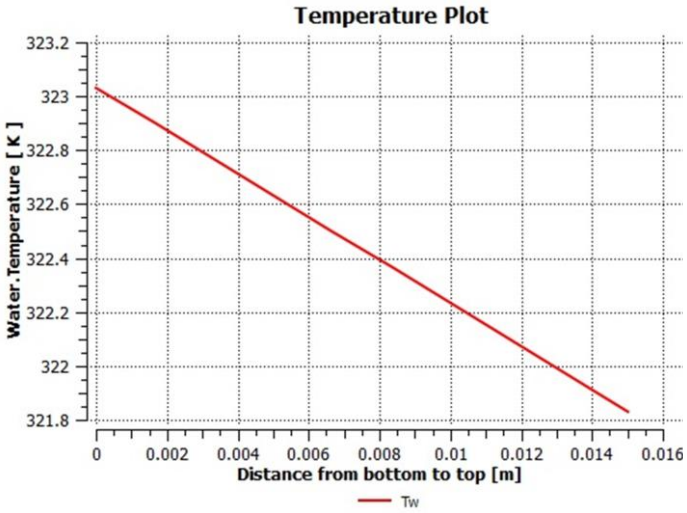

Fig 4.56 Water temperature plot at a bottom temperature of 55°C for a 100mm radius

4.1.3.9 Gas Mixture at a bottom temperature of 60°C

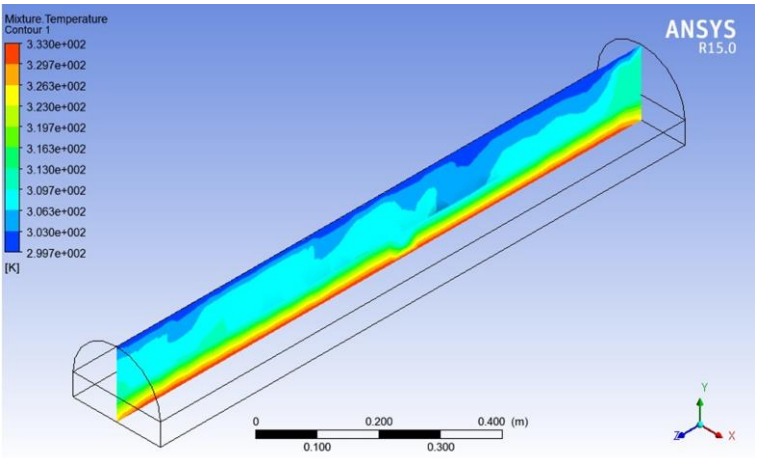

Fig 4.57 Gas mixture temperature contour at a bottom temperature of 60°C for a 100mm radius

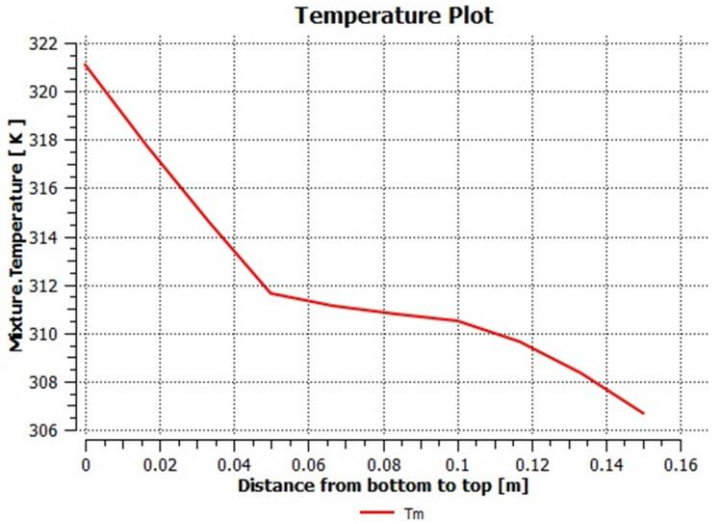

Fig 4.58 Gas mixture temperature plot at a bottom temperature of 60°C for a 100mm radius

4.1.3.10 Water at a bottom temperature of 60°C

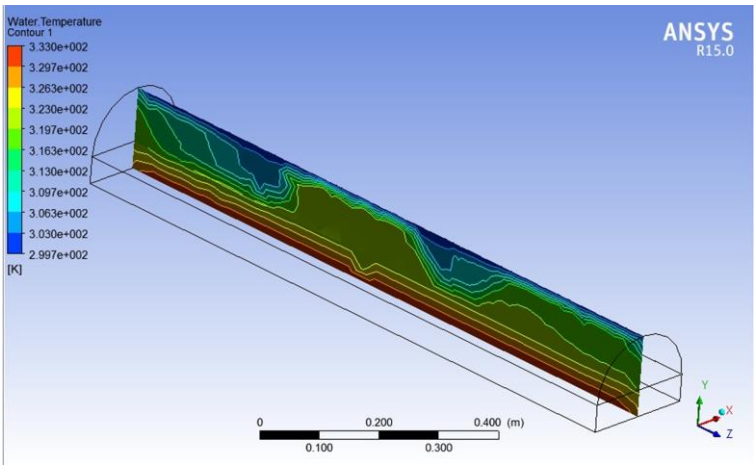

Fig 4.59 Water temperature contour at a bottom temperature of 60°C for a 100mm radius

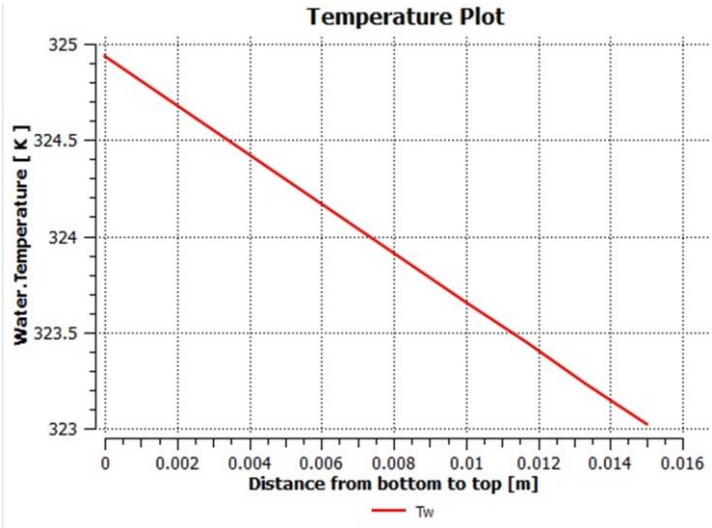

Fig 4.60 Water temperature plot at a bottom temperature of 60°C for a 100mm radius

4.2 EXPERIMENTAL VALIDATION

4.2.1 Water production rate by CFD and Experimental data

When the saline water is heated, water gets evaporated and converted into water vapor which is condensed to obtain potable water in liquid state. ANSYS CFX gives the mass flow of gas and water in Kg/sec which is divided by evaporation area to obtain the amount of fresh water produced. It was assumed that the amount of water evaporated is equal to the rate of water production Kg/m^2 sec. In other words, the amount of water evaporated is equal to the amount of water condensed. The same amount of water is collected in distillate channel. To represent the mass flow, three images of contours are taken as shown in figures (4.61), (4.62) and (4.63) for 100mm, 150mm and 200mm radii respectively.

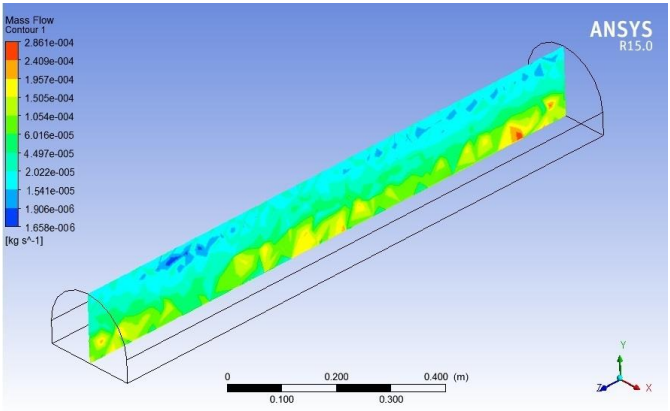

Fig. 4.61 Water mass flow predicted by CFD simulation for 100mm radius model

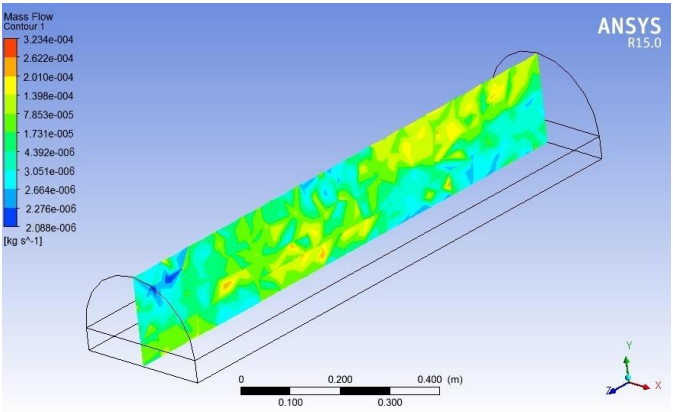

Fig. 4.62 Water mass flow predicted by CFD simulation for 150mm radius model

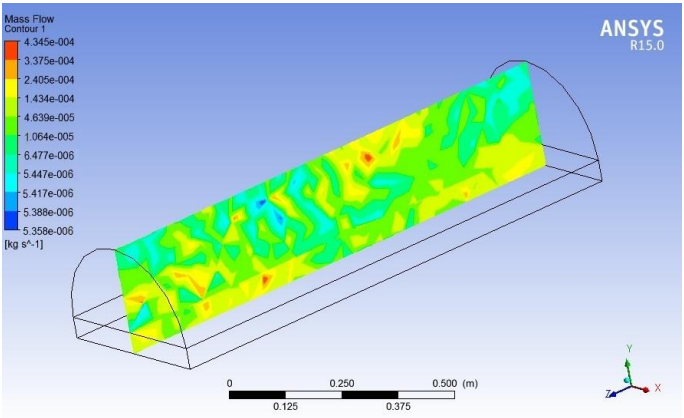

Fig. 4.63 Water mass flow predicted by CFD simulation for 200mm radius model

From the above contours the amount of fresh water produced is calculated. Figures (4.64), (4.65) and (4.66) show the results of

simulation run and experimental data from 40 °C to 60 °C with 5 degrees intervals for all 100mm, 150mm and 200mm radii. In the figures, it is noted that as the process begins when the water in the basin is heated by supplying heat from the bottom. Water starts warming up. Gradually the still space saturates with vapor and fresh water production rate is maximum when the bath temperature is at 60 °C. It has been found that water production rate increases with increasing the heat supplied. This is due to the fact that, at higher temperature evaporation rate is high. The amount of distillate output received will be higher for the higher temperature of evaporative surface, also for lower temperature of condensing surface. In other words, the higher value of evaporative surface temperature and lower value of condensing surface temperature, both leads to the rise in distillate output. A little consideration reveals that both of this increase the temperature difference ΔT between evaporative and condensing surfaces . It plays an important role in optimizing the yield and so ultimately convective mass transfer coefficient as well. In the beginning, water production rate is low as the bath temperature is low. The average error for production rate is 8.6% for 200mm radius, 7.5% for the 150mm model and 5.5% for the 100mm radius model.

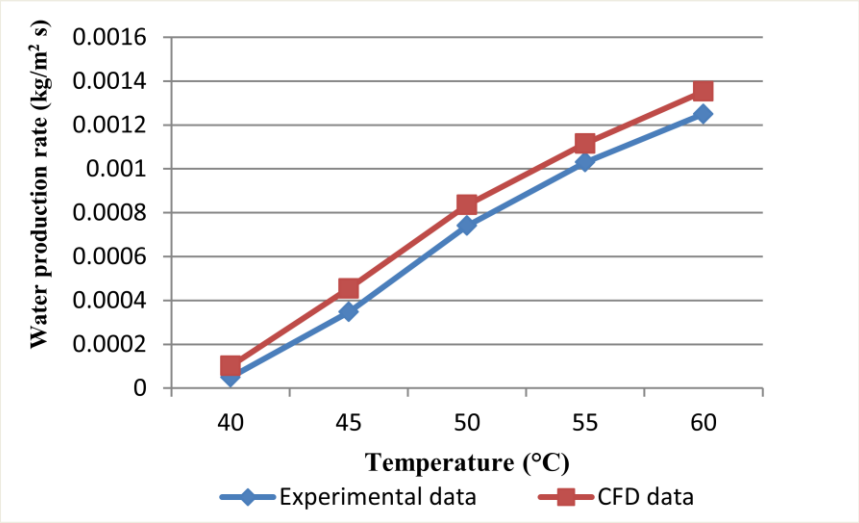

Fig. 4.64 Rate of fresh water production from experimental data and simulation result for 200mm radius

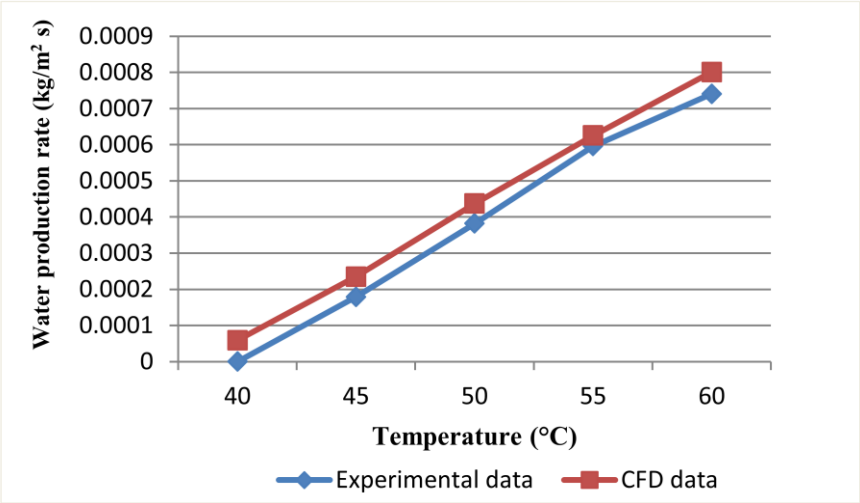

Fig 4.65 Rate of fresh water production from experimental data and simulation result for 150mm radius

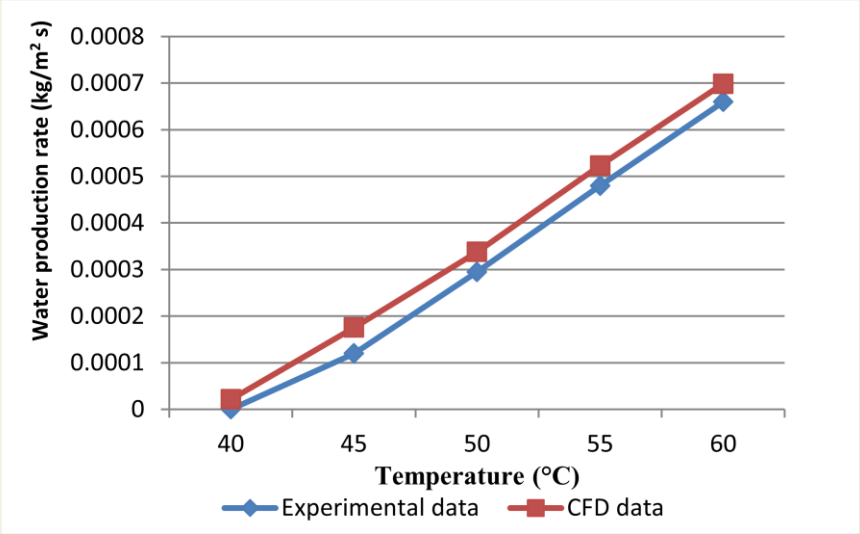

Fig 4.66 Rate of fresh water production from experimental data and simulation result for 100mm radius

Heat transfer is due to the buoyancy force. The gas phase moves on circular path lines between bottom and the glass. Warm water moves upward as its density decreases and the portion of vapor gets condensed on the top where it cools down and gets heavier. And then forces the lighter warm vapor towards the glass. Therefore, a free convection heat transfer mechanism takes place as shown in figures (4.67), (4.68) and (4.69).

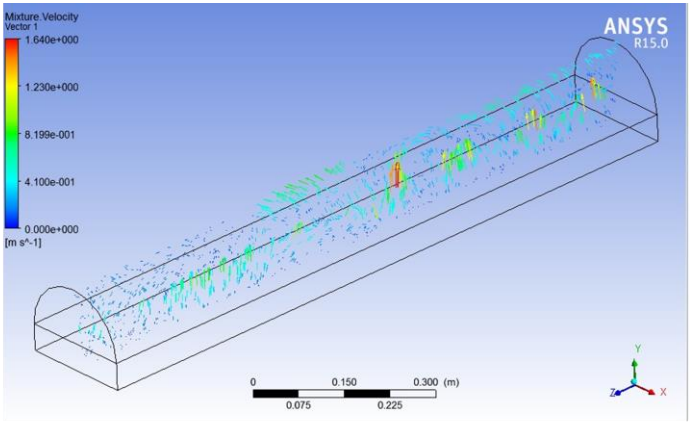

Fig 4.67 Gas mixture velocity on a plane inside the solar still for a 100mm radius

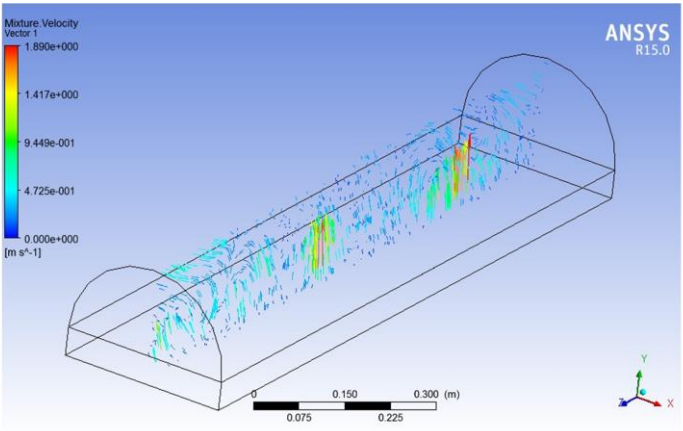

Fig 4.68 Gas mixture velocity on a plane inside the solar still for a 150mm radius

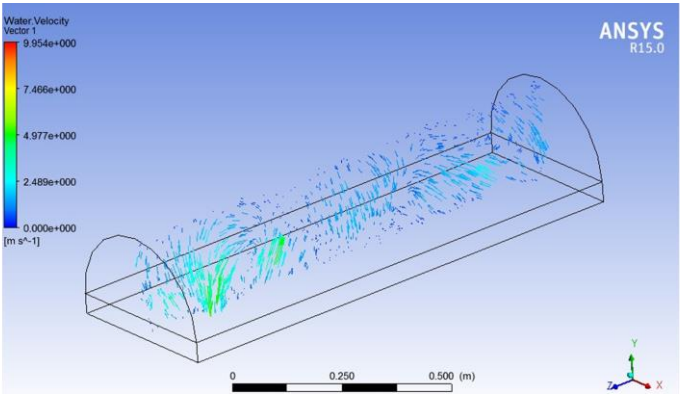

Fig 4.69 Gas mixture velocity on a plane inside the solar still for a 200mm radius

4.2.2 Water production rate by full-TSS and half-TSS models

4.2.2.1 Full-TSS models with constant tray dimensions

The accumulative production rates of distilled water are obtained during the day for each model and presented per unit area. Figure (4.70) shows that the maximum amount of production rate occurred between the three experimental models of the full-TSS. The accumulative productivity per day was highest when the full-TSS with constant tray dimensions was used with 3.9125 kg/m^2 for the diameter of 400mm, followed by 3.7833 kg/m^2 for the middle-sized model with diameter of 300mm, and the lowest accumulative productivity was 2.97 kg/m^2 for the lowest TSS diameter of 200mm. Figure (4.71) shows the accumulative

productivity of full TSS models with constant tray dimensions with respect to volume of humid air. The experimental data shows the productivity as a function of the volume of humid air.

$$y = -0.225x^2 + 1.4874x + 1.7084,\ R^2 = 1 \qquad (4.1)$$

where (y) is the productivity (kg/m^2 day) and (x) is the humid air volume(m^3), (Root means square value of R^2)

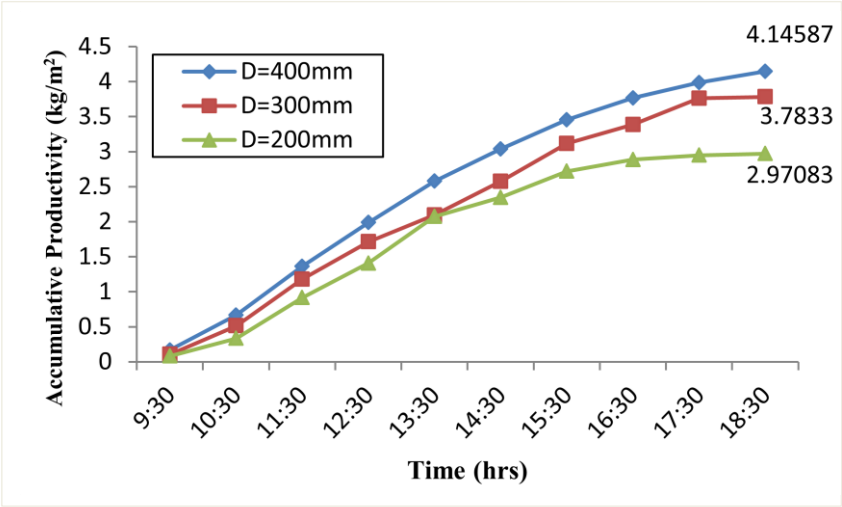

Fig 4.70 Accumulative productivity of full-TSS models with constant tray dimensions

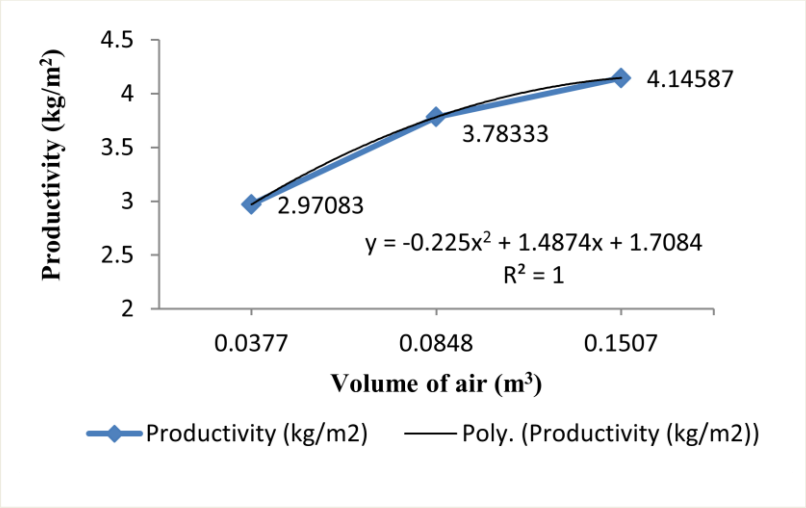

Fig 4.71 Accumulative productivity of full-TSS models with constant tray dimensions with respect to volume of humid air

4.2.2.2 Half-TSS models with constant tray dimensions

The production rate of half-TSS with constant tray dimensions took the second rank of the daily accumulative production of distilled water with respect to humid air volume, with 3.979 kg/m^2 for a 200mm radius, 2.687 kg/m^2 for a 150mm radius and 2.416 kg/m^2 for a 100mm radius per day as shown in figure (4.72). Figure (4.73) shows the productivity as a function of the volume of humid air.

$$y = 0.5104x^2 - 1.2604x + 3.1667, \quad R^2 = 1 \qquad (4.2)$$

where (y) is the productivity (kg/m^{2}day) and (x) is the volume of humid air (m^3), (Root means square value of R^2)

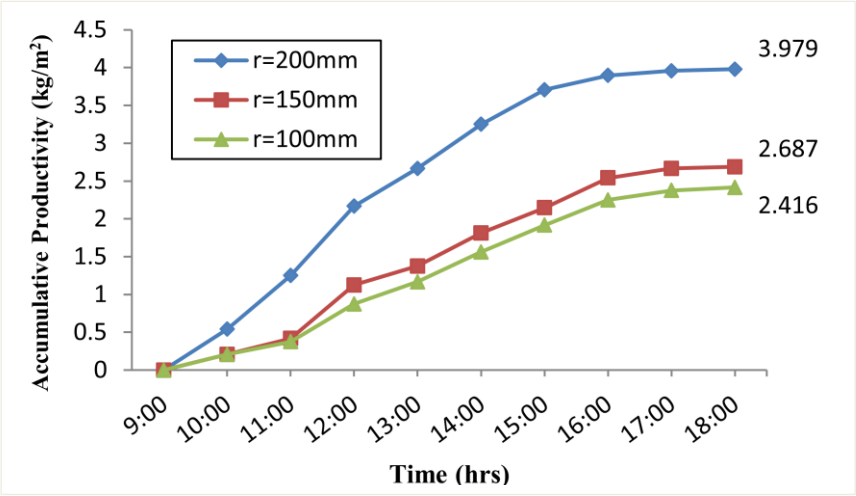

Fig 4.72 Accumulative productivity of half-TSS models with constant tray dimensions

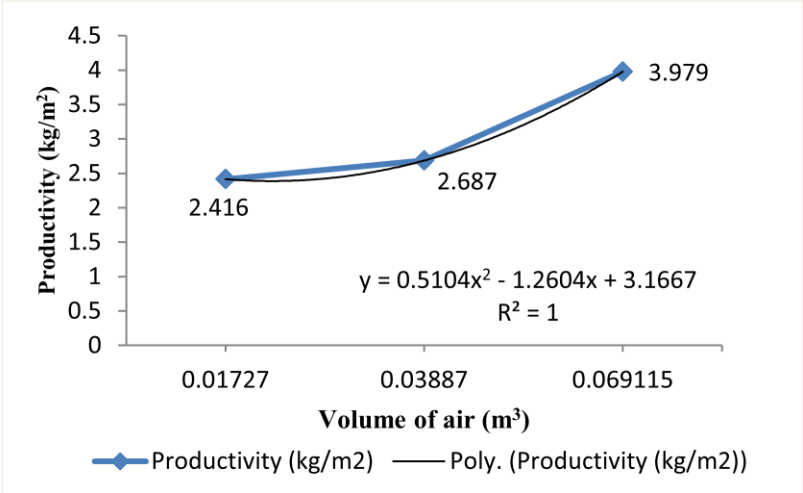

Fig 4.73 Accumulative productivity of half-TSS models with constant tray dimensions with respect to volume of humid air

4.2.2.3 Half-TSS models with variable tray dimensions

The lowest production rate per unit area were taken from the half-TSS models with variable tray dimensions. It was noticed that at the end of the day the accumulative production of distilled water was equal for all three models with 2.375 kg/m³ for the 200, 150 and 100mm radii with respect to humid air volume as shown in figure (4.75). A constant productivity shown in figure (4.76) as a function of the volume of humid air.

$$y = 2.375, \qquad R^2 = \#N/A \tag{4.3}$$

where (y) is the productivity (kg/m^2 day), (Root Mean square value R^2)

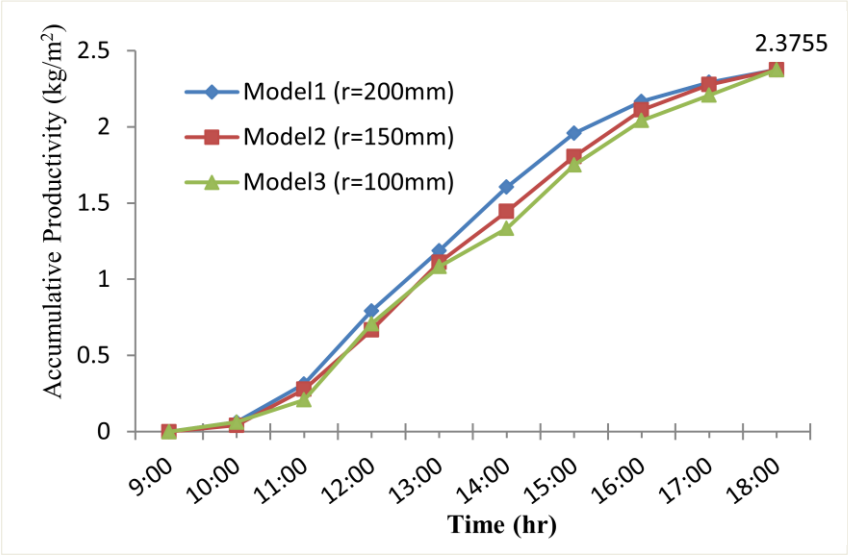

Fig. 4.74 Accumulative productivity of half-TSS models with variable tray dimensions

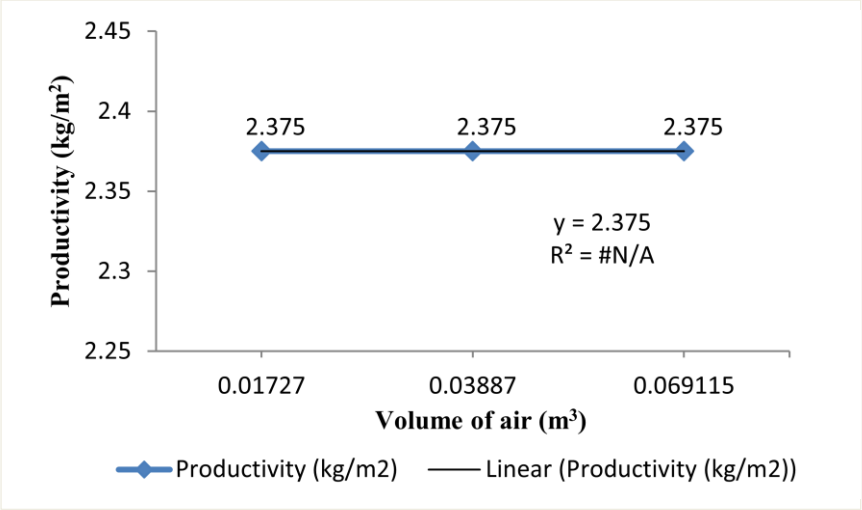

Fig. 4.75 Accumulative productivity of half-TSS models with variable tray dimensions with respect to volume of humid air

4.2.3 Water temperature by CFD and Experimental data

When the results extracted from the water temperature as predicted by the CFD simulation were compared with available experimental data of half-TSS models of 100, 150, 200mm radii with constant tray dimensions as figured in figures (4.76), (4.77) and (4.78), the water temperature was in good agreement between the CFD simulation and experimental data. These figures were drawn with water temperature as ordinate and bath temperature as abscissa. The average error of water temperature between the CFD simulation and experimental data is 5.2% with a 100mm radius, 4.6% with a 150mm radius and 5.3% with a 200mm radius with rise in bath temperature.

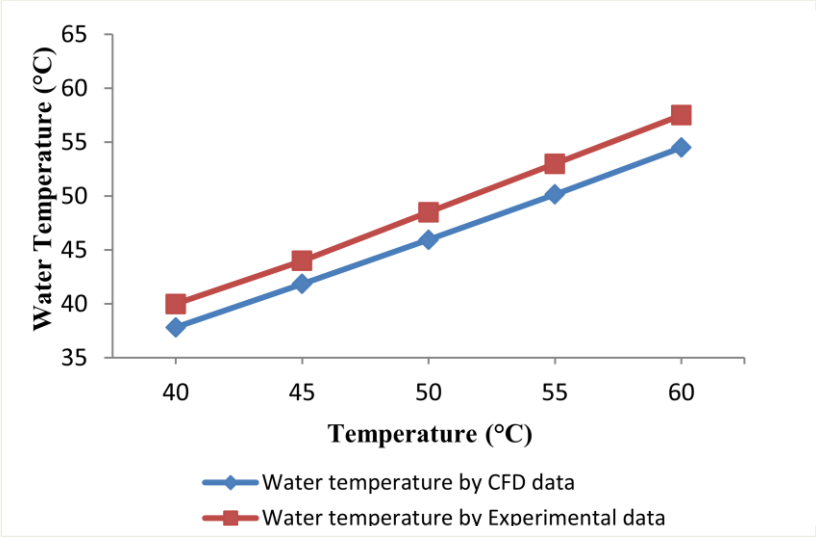

Fig. 4.76 Water temperature predicted by the CFD simulation and experimental data for 100mm radius

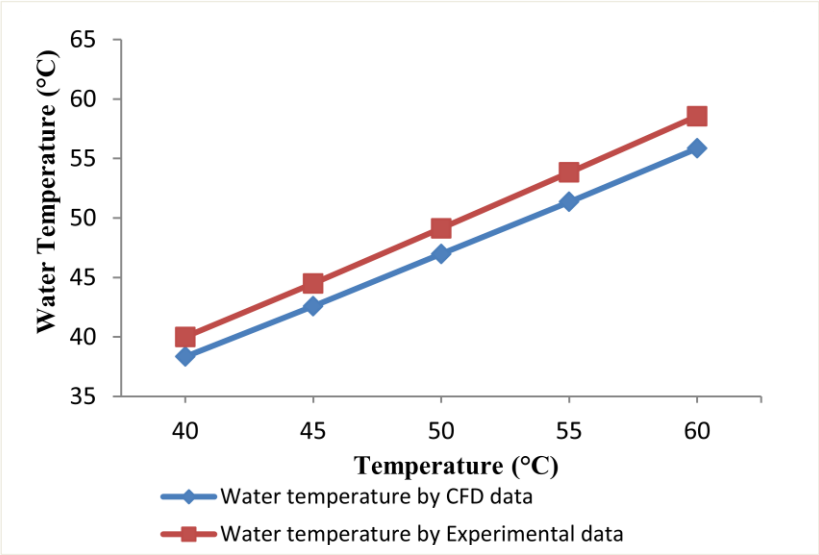

Fig. 4.77 Water temperature predicted by the CFD simulation and experimental data for 150mm radius

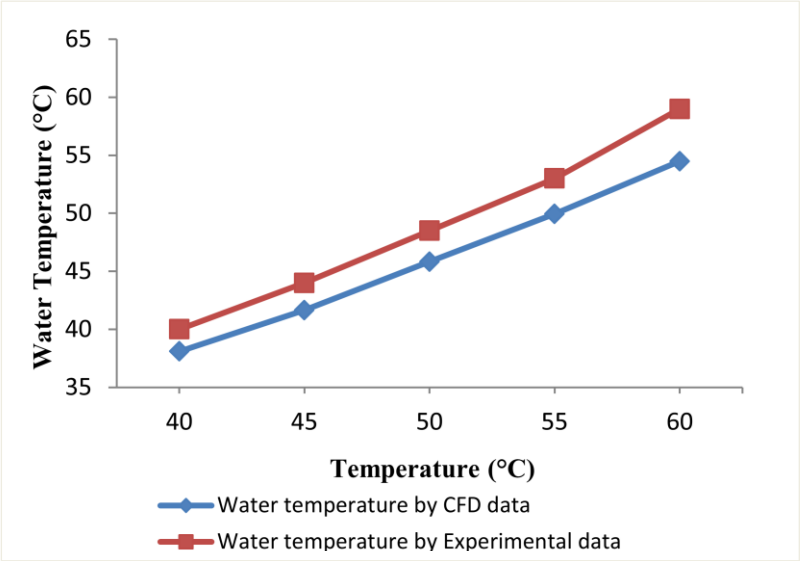

Fig. 4.78 Water temperature predicted by the CFD simulation and experimental data for 200mm radius

`

CHAPTER 5

CONCLUSION AND FUTURE SCOPE

5.1 FLOW OF WORK DONE

In the present thesis, work modeling of evaporation and condensation process is done for different diameters of condensing covers and different tray dimensions to optimize the mass yield to improve the performance of distillation unit under normal weather conditions. The performance of solar stills is evaluated by varying the temperature at the bottom of the solar still from 40 ℃ – 60 ℃ at radii of 100, 150 and 200 mm. Initially, all simulation work is done on ANSYS CFX. The simulation of an evaporation process is conducted on a tubular solar still. Different sets of simulation are phased by varying the temperature of the top and the bottom of the solar still according to experimental data. The behavior of phase change and temperature distribution is observed due to evaporation. The temperature of water obtained by CFX and mass yield is compared with the available experimental data. Three radii of condensing cover at 100, 150 and 200mm are taken for simulation. By plotting the curves of mass of water produced, convective and evaporative heat transfer coefficients are optimized with regard to which condensing cover attained the best performance. Based on the results of the present work, following conclusions are drawn:

1. Selecting best radius with best tray dimensions: A comparison between the three TSS models for the three experiments on the same 200mm radius were done as shown in figure (5.1), to reveal the variation of distilled water productivity throughout the day with respect to the volume of humid air. As a result of the comparison, the maximum productivity was achieved from the full-TSS model with constant tray dimensions with the value of 4.145 kg/m^2 day, followed by the half TSS model with constant tray dimensions by 3.979 kg/m^2 day with a slight productivity difference of 4% between the two models. The least productivity value per day was extracted from the half TSS model with variable tray dimensions with a productivity difference of 40% less than the same model with constant tray dimensions , and with a difference of 42.7% in lower productivity than the full TSS with constant try dimensions. The difference in distilled water production between the full- and half-TSS models with constant tray dimensions amounted to 0.166 kg/m^2. It is obvious from the economical point of view, that the half-TSS with constant tray dimensions is the best selection for the maximum pure water productivity as it is exactly 50% off glass/plastic cover price than the full glass/plastic model with only a 4% difference in productivity.

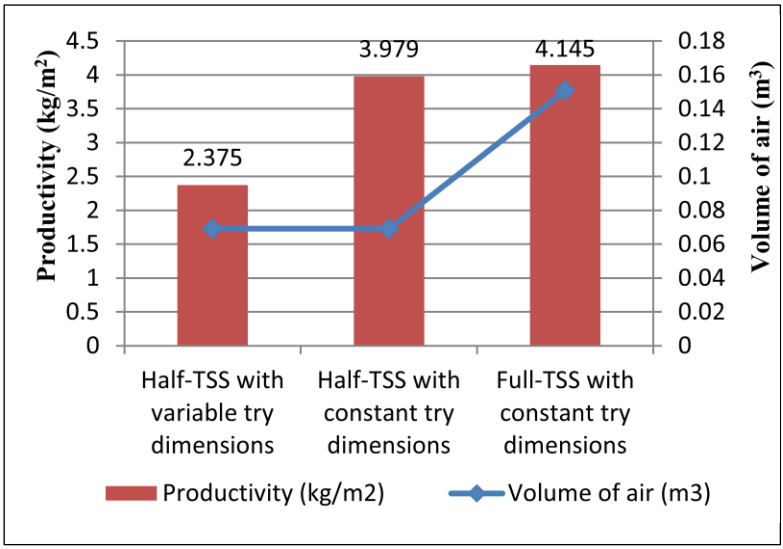

Fig 5.1 Comparison between three TSS models for the three experiments with the same 200mm radius Vs the volume of humid air

2. Effect of input parameter on yield: In the previous chapter it is shown that if the temperature at the bottom is increasing, the production yield is also increasing. So temperature applied at the bottom is the most significant factor.

3. Effect of the span of temperature range: It is concluded that if the temperature is reduced, rise in the value of convective and evaporative heat transfer is also reduced.

4. Experimental validation: Evaluating the simulation results with experimental data, concerning heat distribution from 40-60 °C, water temperature and mass of fresh water produced, it was observed that the

results produced by the CFD simulation are in good agreement within an error margin.

5.2 FUTURE SCOPE

There were several improvements that could be implemented to enhance the design and performance but due to time restrictions of this project it was not possible to execute these improvements. These suggestions are recommended for any future work to be conducted on the solar still for desalination purposes:

1. The CFD analysis of the multiphase water evaporation process could be improved by simulating a buoyant flow as solar radiation falls on the condensing cover instead of supplying heat to the bottom of the basin. This could be done by applying radiation on the condensing cover.
2. Computer simulation can be used for simulating the evaporation process through new solar still designs. Designs of solar stills can be improved further by changing different cross-sections by changing the shapes of the condensing cover.
3. A CFD analysis should be conducted on the condensation process by considering a separate condenser.

`

References

[1] Human Development Report 2006. UNDP, 2006 Coping with water scarcity. Challenge of the twenty-first century. UN-Water, FAO, 2007.

[2] B.A. Jubran1, M.I. Ahmed, A.F. Ismail, Y.A. Abakar. Numerical modelling of a multi-stage solar Still, Energy Conversion & Management 41 (2000) 1107-1121.

[3] K.Sampathkumar,T.V.Arjunan,P.Pitchandi,P.Senthilkumar,Activesolardistillation-A detailed review, Renew. Sustainable Energy Rev. 14 (2010) 1503–1526.

[4] G.N. Tiwari and A. Tiwari, Solar Distillation Practice for Water Desalination Systems, Anamaya, New Delhi, 2007.

[5] H.P. Garg and H.S. Mann, Effect of climatic, operational and design parameters on the year round of single-sloped and double-sloped solar still under Indian arid zone conditions, Solar Energy, 18 (1976) 159–163.

[6] J.A. Eibling, S.G. Talbert and G.O.G. Lof, Solar stills for community use-digest of technology, Solar Energy, 13 (1971) 263–276.

[7] http://www.crses.sun.ac.za/technologies-solar.php

[8] Hazim Mohameed Qiblawey, Fawzi Banat. Solar thermal desalination technologies. Desalination. 220 (2008) 633–644.

[9] Mohamed A. Eltawil, Zhao Zhengming, Liqiang Yuan. A review of renewable energy technologies integrated with desalination systems. Renewable and Sustainable Energy Reviews 13 (2009) 2245–2262.

[10] Mohammed Abdel wahab Sharf Eldin (Design and Simulation of Solar Desalination Systems) PhD thesis 2011.

[11] Mohamed A. Eltawil, Zhao Zhengming, Liqiang Yuan. A review of renewable energy technologies integrated with desalination systems. Renewable and Sustainable Energy Reviews 13 (2009) 2245–2262.

[12] Hanafi A. Design and performance of solar MSF desalination system. Desalination 1991; 82 (1–3): 165–74.

[13] Banat F, Jwaied N. Economic evaluation of desalination by small-scale autonomous solar-powered membrane distillation units. Desalination 2008; 220:566–73.

[14] Delyannis EE. Status of solar assisted desalination: a review, Desalination 1987; 67:3–19.

[15] Manjares R, Galvan M. Solar multistage flash evaporation (SMSF) as a solar energy application on desalination processes. Description of one demonstration project. Desalination 1979;31(13):545–54.
[16] Palma F. Seminar on new technologies for the use of renewable energies in water desalination, Athens, 1991. Commission of the European Communities, DG XVII for Energy, CRES (Centre for Renewable Energy Sources) 1991.
[17] Valverde Muela V. Planta Desaladora con Energia Solar de Arinaga (Las Palmas de Gran Canaria). Departamento de Investigacion Nuevas Fuentes. Centro de Estudios de la Energia; April, 1982.
[18] Moh'd S. Abu-Jabal, I. Kamiya, Y. Narasaki, Proving test for a solar-powered desalination system in Gaza–Palestine, Desalination 137 (2001) 1–6.
[19] Kyritsis S. Proceedings of the Mediterranean Conference on Renewable Energy Sources for Water Production. European Commission, EURORED Network, CRES, EDS, Santorini, Greece; 10–12 June, 1996. p. 265–70.
[20] Kyritsis S. Proceedings of the Mediterranean Conference on Renewable Energy Sources for Water Production. European Commission, EURORED Network, CRES, EDS, Santorini, Greece; 10–12 June, 1996. p. 265–70.
[21] Mark Wilf, Craig Bartels, Optimization of seawater RO systems design, Desalination 173 (2005) 1-12.
[22] http://puretecwater.com/what-is-reverse-osmosis.html
[23] T. Mezhar, H. Fath, Z. Abbas, & A. Khaled (2011) Techno-economis assessment and environmental impacts of desalination technologies. Desalination, vol. 266, p.263-276.
[24] master engineering thesis.
[25] A Mills (1999) Heat Transfer, Prentice Hall, New Jersey.
[26] Kalogirou, S. (2009). Solar energy engineering: Processes and systems. Burlington, MA: Elsevier/Academic Press.
[27] Kalogirou, S. (2009). Solar energy engineering: Processes and systems. Burlington, MA: Elsevier/Academic Press.
[28] Wheeler, N., Evans, W., (1870) Improvements in Evaporating and Distilling by Solar Heat. http://www.google.com/patents/US102633
[29] Delyannis, E. (2003). Historic background of desalination and renewable energies, Solar Energy, 75(5), 357-366.
[30] NationalArchives, http://www.archives.gov/research/guide-fed-records/groups/380.html
[31] Attia, A. (2012). Thermal analysis for systems uses solar energy as a pressure source for reverse osmosis (RO) water desalination, Solar Energy,

86(9), 2486-2493.

[32] HS Aybar (2007) A review of desalination by solar still. Solar Desalination, pp. 207214.

[33] A.A. Kabeel, Performance of solar still with a concave wick evaporation surface, Energy 34 (2009) 1504–1509.

[34] Hilal Al-Hinai, MS. Al-Nassri, B.A. Jubran. Parametric investigation of a double-effect solar still in comparison with a single-effect solar still, Desalination 150 (2002) 75-83.

[35] T. Arunkumar, R. Jayaprakash, D. Denkenberger et al., "An experimental study on a hemispherical solar still," Desalination, vol. 286, pp. 342–348, 2012.

[36] http://www.redsunin.com/products/evacuated-tube-collector-solar-water-heaters/

[37] Delyannis E. Historic Background of Desalination and Renewable Energies. J Solar Energy Elsevier. 2003; 75: 357–366.

[38] Abdul Jabbar N. Khalifa, Ahmad M. Hamood. Effect of insulation thickness on the productivity of basin type solar stills: An experimental verification under local climate. Energy Conversion and Management 50 (2009) 2457–2461.

[39] A. Safwat Nafey, M. Abdelkader, A. Abdelmotalip, A.A. Mabrouk. Enhancement of solar still productivity using floating perforated black plate. Energy Conversion and Management 43 (2002) 937–946

[40] A. Safwat Nafey, M. Abdelkader, A. Abdelmotalip, A.A. Mabrouk. Enhancement of solar still productivity using floating perforated black plate. Energy Conversion and Management 43 (2002) 937–946.

[41] Prem Shankar and Shiv Kumar, (2011), 'Instantaneous Exergy Efficiency of a Passive Solar Still', International conference on innovative science & engineering technology, 122-126.

[42] Mario Reali and Giovanni Modica, (2008), "Solar stills made with tubes for sea water desalting," Desalination, 220, pp. 626–632.

[43] T.V. Arjunan, H. S. Aybar, N. Nedunchezhian and M. Sakthivel, (2009), 'Effect of Blue Metal Stones on the Performance of a Conventional Solar Still', Journal of Convergence in Engineering, Technology and Science, 1, pp 17-22.

[44] Tiwari GN, Kumar Ashok. Nocturnal water production by tubular solar stills using waste heat to preheat brine. Desalination 1988;69:309–18.

[45] A.K. Tiwari, G.N. Tiwari (2006) Effect of water depths on heat and mass transfer in a passive solar still: in summer climatic condition. Desalination 195, 78-94.

[46] Mahmoud. I.M. Shatat, K. Mahkamov. Determination of rational design parameters of a multi-stage solar water desalination still using transient mathematical modelling. Renewable Energy 35 (2010) 52–61.
[47] Sodha MS, Kumar Asvini, Tiwari GN. Utilization of waste hot water for distillation. Desalination 1981;37:325–42.
[48] V. Gnaneshwar and N. Nimlakhandan (2010), 'Sustainable desalination using solar energy', Energy conversion & management, 51, pp. 2245-2251.
[49] Al-Kharabsheh S, Goswami D Y. Experimental study of an innovative solar water desalination system utilizing a passive vacuum technique. Solar Energy 2003; 75(5): 395-401.
[50] Tiwari GN, Dimri Vimal, Singh Usha, Chel Aravind, Sarkar Bikash. Comparative thermal performance evaluation of an active solar distillation system. International Journal of Energy Research 2007;31:1465–82.
[51] R.V. Dunkle, Solar water distillation; the roof type solar still and a multi effect diffusion still. International developments in heat transfer. A.S.M.E., Proceedings of
[52] Amimul Ahsan, Teruyuki Fukuhara. Mass and heat transfer model of Tubular Solar Still. Solar Energy 84 (2010) 1147–1156.
[53] Amimul Ahsan, Teruyuki Fukuhara. Mass and heat transfer model of Tubular Solar Still. Solar Energy 84 (2010) 1147–1156.
[54] https://www.google.com.eg/maps/place/Suez,+Suez+Governorate

ملخص

إعتمدت تحلية المياه بشكل متزايد على مدى العقود الماضية كخيار، وأحيانا باعتبارها ضرورة للتغلب على نقص المياه في العديد من المناطق حول العالم. وقد استخدمت أشعة الشمس المباشرة لفترة طويلة في السابق لتحلية المياه. وتستخدم وحدات التقطير الشمسية لتوفير المياه المحلاة للمجتمعات الصغيرة القريبة و المناطق النائية و الساحلية. المقطرات الشمسية هي سهلة البناء، ويمكن أن تنفذ من قبل السكان المحليين من المواد المتوفرة محليا، وهي بسيطة البناء ولا تتطلب في عملية بنائها الي أفراد مهرة، ولا تحتاج الى صيانه معقدة. وبالتالي لزيادة أداء الطاقة الشمسية لا يزال من الضروري عمل نموذج ودراسة تأثير العوامل المختلفة على نحو التبخير و التكثيف على الغطاء الزجاجي. الدراسة الحالية تهدف إلى نمذجة الطاقة الشمسية بإستخدام برنامج النمذجة و المحاكاه أنسيس سي إف إكس ١٥،٠ (ANSYS CFX 15.0) للتحقيق في تأثير أنصاف الأقطار المختلفة على إنتاجية المياه المحلاه. تم تطوير نموذج ثلاثي الأبعاد لمحاكاة عملية التبخير والتكثيف لمحاكاة توزيع درجات حرارة المياه والبخار داخل النموذج و مقارنتها بالنتائج المعملية وأيضا على كمية إنتاجية المياه العذبة. تمت دراسة ثلاثة أنصاف أقطار مختلفة لتحليل تأثير على معدل التبخر. ويتم محاكاة من ٤٠-٦٠ درجة مئوية مع فارق ٥ درجات مؤية على ثلاث نماذج بأنصاف أقطار ١٠٠ و ١٥٠ و ٢٠٠ ملم نصف قطر. تم إجراء التجربة العملية في محافظة السويس (خط عرض ُ ٢٩ °٩٦٦ و الطول ُ٣٢ ° ٥٤٩)

.

الناشر	**عبدالهادي محمد ماهر محمد الهادي زغلول**
عنوان الرسالة	**دراسة عددية وتجريبية للمقطر الشمسي الانبوبي**
الكلية	**هندسة البترول و التعدين**
القسم	**قسم العلوم الهندسية**
الدرجة	**الماجستير في هندسة الطاقة**
العنوان	**السويس- مصر**
التاريخ	**2015/7/27**
اللغة	**الإنجليزية**
لجنة الإشراف	**د/سيد عثمان الحليبي** **د/ أحمد محمد سليمان** **د/محمد عبدالوهاب شرف الدين**

ملخص البحث

إعتمدت تحلية المياه بشكل متزايد على مدى العقود الماضية كخيار، وأحيانا باعتبارها ضرورة للتغلب على نقص المياه في العديد من المناطق حول العالم. وقد استخدمت أشعة الشمس المباشرة لفترة طويلة في السابق لتحلية المياه. وتستخدم وحدات التقطير الشمسية لتوفير المياه المحلاة للمجتمعات الصغيرة القريبة و المناطق النائية و الساحلية. المقطرات الشمسية هي سهلة البناء، ويمكن أن تنفذ من قبل السكان المحليين من المواد المتوفرة محليا، وهي بسيطة البناء ولا تتطلب في عملية بنائها الي أفراد مهرة، ولا تحتاج الى صيانه معقدة. وبالتالي لزيادة أداء الطاقة الشمسية لا يزال من الضروري عمل نموذج ودراسة تأثير العوامل المختلفة على نحو التبخير و التكثيف على الغطاء الزجاجي. الدراسة الحالية تهدف إلى نمذجة الطاقة الشمسية بإستخدام برنامج النمذجة و المحاكاه أنسيس سي إف إكس ١٥،٠ (ANSYS CFX 15.0) للتحقيق في تأثير أنصاف الأقطار المختلفة على إنتاجية المياه المحلاه. تم تطوير نموذج ثلاثي الأبعاد لمحاكاة عملية التبخير والتكثيف لمحاكاة توزيع درجات حرارة المياه والبخار داخل النموذج و مقارنتها بالنتائج المعملية وأيضا على كمية إنتاجية المياه العذبة. تمت دراسة ثلاثة أنصاف أقطار مختلفة لتحليل تأثير على معدل التبخر. ويتم محاكاة من ٤٠-٦٠ درجة مئوية مع فارق ٥ درجات مؤية على ثلاث نماذج بأنصاف أقطار ١٠٠ و ١٥٠ و ٢٠٠ ملم نصف قطر. تم إجراء التجربة العملية في محافظة السويس (خط عرض ٢٩° ٩٦٦° و الطول ٣٢′ ٥٤٩ °)

.

الكلمات الدالة: المقطر الأنبوبي, أنسيس سي إف إكس 15.0, سي إف دي

جامعة السويس
كلية هندسة البترول و التعدين
قسم العلوم الهندسية

الموافقة

دراسة عددية وتجريبية للمقطر الشمسي الانبوبي

رسالة مقدمة من
المهندس/عبدالهادي محمد ماهر محمد الهادي زغلول
بكالوريوس الهندسة الميكانيكية
2006
للحصول علي درجة الماجستير في
هندسة الطاقة

لجنة فحص و مناقشة الرسالة

أ.د.الدسوقي إبراهيم عيد
أستاذ هندسة القوي الميكانيكية
عميد كلية التعليم الصناعي
جامعة السويس

د.أحمد صفوت محمد
أستاذ مساعد الهندسة الميكانيكية -قسم العلوم الهندسيه
كلية هندسة البترول و التعدين
جامعة السويس

د.سيد عثمان الحليبي
أستاذ مساعد بقسم الهندسة الميكانيكية -قسم العلوم الهندسيه
كلية هندسة البترول و التعدين
الجامعة السويس

يعتمد

تاريخ المناقشة 2015/7/27

عميد الكلية

السويس
2015

جامعة السويس
كلية هندسة البترول و التعدين
قسم العلوم الهندسية

دراسة عددية وتجريبية للمقطر الشمسي الانبوبي

رسالة مقدمة من
المهندس/عبدالهادي محمد ماهر محمد الهادي زغلول
بكالوريوس الهندسة الميكانيكية
2006
للحصول علي درجة الماجستير في
هندسة الطاقة

لجنة أشراف

د.سيد عثمان الحليبي
أستاذ مساعد بقسم الهندسة الميكانيكة-قسم العلوم الهندسية
كلية هندسه البترول و التعدين
جامعة السويس

د.أحمد محمد سليمان
مدرس الهندسة الميكانيكية-قسم العلوم الهندسيه
كلية هندسة البترول و التعدين
جامعة السويس

د.محمد عبدالوهاب شرف الدين
مدرس الهندسة الميكانيكية -قسم العلوم الهندسيه
كلية هندسة البترول و التعدين
جامعة السويس

السويس
2015